FIRST-PRINCIPLES THEORY OF LOW-DIMENSIONAL SYSTEMS, THEIR ASSEMBLY, AND THE INFLUENCE OF THEIR ENVIRONMENT

By

Liangbo Liang

A Dissertation Submitted to the Graduate

Faculty of Rensselaer Polytechnic Institute

in Partial Fulfillment of the

Requirements for the Degree of

DOCTOR OF PHILOSOPHY

Major Subject: PHYSICS

Examining Committee:

_____
Vincent Meunier, Dissertation Advisor

_____
Shengbai Zhang, Member

_____
Kim Lewis, Member

_____
Liping Huang, Member

Rensselaer Polytechnic Institute
Troy, New York

April 2014
(For Graduation May 2014)

© Copyright 2014
by
Liangbo Liang
All Rights Reserved

CONTENTS

LIST OF TABLES vii

LIST OF FIGURES viii

ACKNOWLEDGMENT xviii

ABSTRACT xix

1. List of computational methods 1
   - 1.1 Density functional theory 1
   - 1.2 Many-body *GW* approximation 1
   - 1.3 Tight-binding and Hubbard model 1
   - 1.4 The computation of the thermoelectric figure of merit 2
   - 1.5 Image charge model for band gap reduction 2
   - 1.6 Non-equilibrium Green's function formalism 2
   - 1.7 The computation of power conversion efficiency of a solar cell 2
   - 1.8 Non-resonant first-order Raman scattering 2

I Graphene-based materials: graphene nanowiggles **3**

2. Background on graphene and graphene-based materials 4
   - 2.1 Graphene sheets 4
   - 2.2 Graphene nanoribbons 5
   - 2.3 Graphene nanowiggles 7
   - 2.4 Overview for the rest of Part I 10

3. Electronic and magnetic properties of GNWs 11
   - 3.1 Introduction 11
   - 3.2 Geometry and nomenclature 11
   - 3.3 Theoretical methods 13
     - 3.3.1 Density functional theory 13
     - 3.3.2 Tight-binding+Hubbard model 17
   - 3.4 Electronic and magnetic properties 18

3.4.1 AA-GNWs . . . 18
3.4.2 AZ-GNWs . . . 20
3.4.3 ZA-GNWs . . . 21
3.4.4 ZZ-GNWs . . . 22
3.5 Quasiparticle corrections . . . 22
3.6 Summary . . . 26
4. Thermal and thermoelectric properties of GNWs . . . 27
4.1 Introduction . . . 27
4.2 Theoretical methods . . . 28
4.3 Thermal and thermoelectric properties . . . 30
4.3.1 AA-GNWs . . . 30
4.3.2 ZZ-GNWs . . . 31
4.3.3 Electronic resonant tunneling . . . 33
4.4 Systematic study: establishing a roadmap to optimal *ZT* in GNWs . . . 33
4.5 Structural modifications to further enhance *ZT* . . . 35
4.6 Summary . . . 36
5. Substrate effects on electronic and magnetic properties of GNRs and GNWs . . . 38
5.1 Introduction . . . 38
5.2 Theoretical methods . . . 39
5.3 Substrate effects on electronic properties . . . 40
5.3.1 Geometry on the substrate . . . 40
5.3.2 Band structures on the substrate . . . 41
5.3.3 Charge transfer and substrate polarization . . . 42
5.3.4 Band gap reduction by substrate polarization: an image charge approach . . . 43
5.4 Substrate effects on magnetic properties . . . 46
5.5 Summary . . . 48
6. Heterojunctions of pure and nitrogen-doped GNWs . . . 49
6.1 Introduction . . . 49
6.2 Theoretical methods . . . 50
6.2.1 Non-equilibrium Green's function (NEGF) formalism . . . 50
6.3 Electronic and transport properties of p-N-GNW heterojunctions . . . 53

6.4 Type-II band alignment for solar cell applications 57
6.5 Summary 59

II Graphene-like materials: transition metal dichalcogenides 61

7. Background on transition metal dichalcogenides 62
7.1 Structural, electronic and photoluminescence properties of TMDs 62
7.2 Raman spectra of TMDs 65
7.3 Overview for the rest of Part II 67
8. First-principles Raman spectra of MoS_2, WS_2 and their heterostructures 68
8.1 Introduction 68
8.2 Theoretical methods 69
8.3 Electronic and dielectric properties of MoS_2 and WS_2 72
8.4 Raman spectra of MoS_2 and WS_2 73
8.5 Laser polarization effect on Raman spectra 76
8.6 Raman scattering of MoS_2/WS_2 heterostructures 80
8.7 Summary 84

III Fe-based superconductors: spin-dependent surface reconstruction 86

9. Spin ordering in the (1×2) surface reconstruction of $Ca(Fe_{1-x}Co_x)_2As_2$ 87
9.1 Introduction 87
9.2 Experimental and theoretical methods 89
9.3 Results and discussions 90
9.4 Summary 96
10. Conclusions and perspectives 97
10.1 Conclusions 97
10.2 Perspectives 101
REFERENCE 103
APPENDICES 110

A. Publications Related to the Thesis 111
INDEX 113

LIST OF TABLES

3.1 The summary of *GW* and DFT band gaps of different magnetic states for the four GNWs. 26

5.1 DFT and *GW* band gaps of free-standing and substrate-supported AGNR-7 and GNW (9_A,6_A). For the substrate-supported case, the *GW* band gaps are estimated in combination of *GW* and the image charge model. The experimental band gaps [66] of substrate-supported AGNR-7 and (9_A,6_A) are also shown for comparison. 45

8.1 Frequency differences and intensity ratios for MoS_2, WS_2 and their heterostructures. 80

9.1 Details of stripe (1×2) surface structures of Ca122 and 7.5% Co-doped Ca122. 93

9.2 Bader charges for orthorhombic Ca122 surface and bulk with or without including the AFM spin ordering. See Ref. [147] for details regarding Bader charges. 94

LIST OF FIGURES

2.1 (a) Graphene and its 2D Brillouin zone. (b) Band structure of graphene along high symmetry directions. (c) 3D representation of the π bands with the Dirac points at the K point. Graphene is hence a zero-gap semiconductor or semi-metal. From Ref. [2]. 4

2.2 Geometry of (a) AGNRs and (b) ZGNRs with edges hydrogenated. The red boxes indicate the GNRs unit cells. They are periodic along the vertical direction. From Ref. [1]. 6

2.3 Paramagnetic (PM), anti-ferromagnetic (AFM) and ferromagnetic (FM) states in a ZGNR and their corresponding band structures. The green line is the Fermi energy, and the black and red lines stand for spin up and down levels. All the bands are degenerate in PM and AFM states. From Ref. [1]. 7

2.4 (a) Bottom-up fabrication of atomically precise GNRs. Basic steps for surface-supported GNR synthesis, illustrated with a ball-and-stick model of the example of 10,10′-dibromo-9,9′-bianthryl monomers. (b) Straight GNRs from bianthryl monomers and the high-resolution STM image. (c) Chevron-type GNRs from tetraphenyl-triphenylene monomers and the high-resolution STM image. (d) Threefold GNR junction obtained from a 1,3,5-tris(4″-iodo-2′-biphenyl) benzene monomer 3 at the nodal point and monomer 2 for the ribbon arms, and its STM image. From Ref. [21]. 8

2.5 Monomers for the generation of graphene nanowiggles with defined edge-doping via on-surface polymerization followed by cyclo-dehydrogenation. Shown are monomers 1-3 with either none, one or two doping N-atoms, while the synthesis is exemplarily shown for the case of the doubly nitrogen-doped GNW. From Ref. [22]. 9

3.1 (a) Geometry and nomenclature of a hydrogenated GNW made up of successive parallel (P) and oblique (O) sectors with armchair- (A) or zigzag- (Z) edged geometries. (b)-(e) Examples of an AA, AZ, ZA and ZZ GNW, respectively. They are periodic in the horizontal direction. 12

3.2 Schematic of the first-, second-, and third-nearest neighbor hopping integrals (γ_1, γ_2 and γ_3) on an armchair-edged graphitic structure. The different chemical environment at the edges is accounted for by a modified first neighbor interaction for these frontier atoms. From Ref. [26]. 17

3.3 TBU (solid lines) and DFT (dashed lines) electronic band structures of different magnetic states for AA (9_A,6_A), AZ (6_A,7_Z), ZA (4_Z,9_A) and ZZ (7_Z,7_Z) GNWs. The schematic spin distributions (black: up, red: down) are shown on top of each panel. The Fermi level is set at 0 eV for each graph. . 19

3.4 TBU energy band gap as a function of the widths of parallel (P) and oblique sectors (O) for (a) AA GNWs in the PM state, and for (b) AZ, (c) ZA and (d) ZZ GNWs in the AFM state. The points absent mainly on the upper-left corner of each graph correspond to geometries not allowed by the particular choice for P and O. For (b)-(d), the systems that do not possess a stable AFM state are marked by a cross. In these charts, the band gap minima and maxima (in unit of eV) are (a) Δ^{AA}_{min}=0.00, Δ^{AA}_{max}=1.70; (b) Δ^{AZ}_{min}=0.18, Δ^{AZ}_{max}=0.45; (c) Δ^{ZA}_{min}=0.11, Δ^{ZA}_{max}=0.48; (d) Δ^{ZZ}_{min}=0.21, Δ^{ZZ}_{max}=0.49. 20

3.5 The repulsive Coulomb interaction creates a Coulomb hole (or cloud) around an electron to form a quasiparticle. 23

3.6 *GW* (solid lines) and DFT (dashed lines) electronic band structures of different magnetic states for the GNWs shown in Fig. 3.1. The schematic spin distributions (black: up, red: down) are shown on top of each panel. The Fermi level is set at 0 eV for each graph. 25

4.1 ZT versus chemical potential μ at T=300 K obtained both by DFT (black) and TB (red) for AA (9_A,6_A), AZ (7_A,4_Z), ZA (4_Z,9_A) and ZZ (6_Z,4_Z) GNWs. Except the AA GNW in the PM state, others are all in the AFM state. 29

4.2 DFT Phonon dispersions and transmission functions of AGNR-9 and AA (9_A,6_A) with their structures on the top. AGNR-9 is the straight counterpart to (9_A,6_A) sharing the same width. (b) Thermal conductance k_{ph} versus temperature of (9_A,6_A) (solid line) and AGNR-9 (dashed line). (c) Electrical conductance G_e; (d) thermal power S; and (e) thermoelectric figure of merit ZT versus chemical potential μ at room temperature (T=300 K) of (9_A,6_A) (solid line) and AGNR-9 (dashed line). The zero in the chemical potential is chosen at the Fermi level. Both structures are in the PM state. 31

4.3 DFT Phonon dispersions and transmission functions of ZGNR-6 and ZZ (6_Z,4_Z) with their structures on the top. ZGNR-6 is the straight counterpart to (6_Z,4_Z) sharing the same width. (b) k_{ph} versus temperature of (6_Z,4_Z) (solid line) and ZGNR-6 (dashed line). (c) G_e; (d) S; and (e) ZT versus μ at room temperature of (6_Z,4_Z) (solid line) and ZGNR-6 (dashed line). The zero in the chemical potential is chosen at the Fermi level. Both structures are in their AFM state. 32

4.4 Peak ZT (room temperature) versus the widths of parallel (P) and oblique (O) sectors for (a) AA GNWs in the PM state, and for (b) AZ, (c) ZA and (d) ZZ GNWs in the AFM state. The points absent mainly on the upper-left corner of each graph correspond to geometries not allowed by the particular choice for P and O. In (a), the column on the right side of the frame represents peak ZT values of AA GNWs' straight counterparts in the PM state. Similarly in (d), the column next to the frame shows peak ZT of ZZ GNWs' straight counterparts in the AFM state. In these charts, minima and maxima of peak ZT values are (a) ZT_{min}=0.04, ZT_{max}=0.79; (b) ZT_{min}=0.12, ZT_{max}=0.65; (c) ZT_{min}=0.07, ZT_{max}=0.56; (d) ZT_{min}=0.04, ZT_{max}=0.57. . . . 34

4.5 (a) Atomic structures of the defect-free GNW (9_A,6_A) (on the top) and its dislocated counterpart (on the bottom). They are periodic in the horizontal direction. (b) thermal conductance k_{ph} versus temperature of the GNW (black line) and dislocated counterpart (red line). (c) Electrical conductance G_e, (d) thermal power S, and (e) thermoelectric figure of merit ZT versus chemical potential μ at room temperature (T=300 K) of the GNW (black line) and dislocated counterpart (red line). The zero in the chemical potential is chosen at the Fermi level. 36

5.1 The adsorption geometry of a hydrogenated (a) AGNR-7 and (b) AA (9_A,6_A) on the Au(111) surface. One unit cell is shown for both cases. Numbers indicate separation distances in Å between circled C atoms and Au atoms right below them. To visualize the bulking of the GNW upon adsorption on the substrate, a height variation (blue curve) of the GNW along the blue line is shown on the right side. 40

5.2 Simulated constant current STM images of AGNR-7 on the gold surface at -1 eV bias voltage with tip height range given by (a) H_{min} = 2.18 Å, H_{max} = 5.18 Å and (b) H_{min} = 4.42 Å, H_{max} = 6.40 Å. H_{min} and H_{max} represent the minimum and maximum tip-substrate distance, respectively. Simulated constant current STM images of (9_A,6_A) on the Au(111) surface at -1 eV bias voltage with (c) H_{min} = 2.20 Å, H_{max} = 5.23 Å and (d) H_{min} = 4.38 Å, H_{max} = 6.43 Å. 41

5.3 (a) Electronic band structures of AGNR-7 deposited on a Au(111) substrate. The dots superimposed on the bands correspond to projected bands due to AGNR-7. Panel (b) only shows the dots, for clarity. (d) Electronic band structures of (9_A,6_A) deposited on a Au(111) substrate. The dots show the projected bands of (9_A,6_A). Panel (e) only shows the projected bands of (9_A,6_A) for clarity. The size of the dot is proportional to the amplitude of the projection. (c) and (f) show electronic band structures of free-standing AGNR-7 and (9_A,6_A), respectively. Solid (dashed) lines represent bands at the *GW* (DFT) level. The Fermi level is set at 0 eV in each graph. 42

5.4 (a) Plane-averaged difference electronic charge densities $\Delta\rho(z) = \rho_{M|G}(z) - \rho_M(z) - \rho_G(z)$ upon formation of the interface for AGNR-7 and AA (9_A,6_A), respectively. (b) Plane-averaged exchange-correlation potential of a clean gold surface and image potential. The origin is set at the first gold layer, and z_0 and z_1 are fitted by setting the intersection of the two curves at z_1. (c) Plane-averaged charge densities for the conduction band minimum (CB_{min}) and the valence band maximum (VB_{max}) of the free-standing (9_A,6_A). . . . 43

5.5 Top view of two most stable adsorption geometries of the GNW (7_A,4_Z) in the AFM state on the Au(111) surface. The system is periodic in both horizontal and vertical directions and one unit cell is shown. To ensure the strongest binding with the substrate, a carbon atom should be either on top of a gold atom or on top of the center of the bridge between two gold atoms. Numbers in red indicate separation distances in Å between circled C atoms and Au atoms right below them. To visualize the bulking of the GNW upon adsorption on the substrate, a height variation (blue curve) of the GNW along the blue line is shown on the left side. 46

6.1 For a GNW heterojunction, the pure GNW (p-GNW) is on the left side of the interface and the nitrogen-doped GNW (N-GNW) is on the right side. There are two types of experimentally realized nitrogen doping in the GNW (9_A,6_A): (a) two nitrogen atoms per monomer unit and (b) four nitrogen atoms per monomer unit. They are denoted as N2 and N4, respectively. Then the corresponding nitrogen-doped GNWs are labeled as N2-GNW and N4-GNW, respectively. Hence, the two types of GNW heterojunctions are denoted as (a) p-N2-GNW heterojunction (b) p-N4-GNW heterojunction. . . 49

6.2 Schematic of a transport system consisting of a conductor and two semi-infinite leads: left and right leads. 50

6.3 (a) Transport device built from a p-N2-GNW heterojunction. The left (right) electrode is semi-infinite in the left (right) direction. (b) Densities of states of the heterojunction (black solid line), p-GNW (red dashed line) and N2-GNW (blue dashed line). (c) Electrical conductance of the heterojunction (black solid line), p-GNW (red dashed line) and N2-GNW (blue dashed line). Fermi level of the heterojunction is at 0 eV. 54

6.4 (a) Transport device built from p-N4-GNW heterojunction. The left (right) electrode is semi-infinite in the left (right) direction. (b) Densities of states of the heterojunction (black solid line), p-GNW (red dashed line) and N4-GNW (blue dashed line). (c) Electrical conductance of the heterojunction (black solid line), p-GNW (red dashed line) and N4-GNW (blue dashed line). Fermi level of the heterojunction is at 0 eV. 55

6.5 DFT calculated type-II band alignments for the pure, N2-doped and N4-doped GNWs (9_A,6_A). VBM and CBM stand for valence band maximum and conduction band minimum, respectively. 56

6.6 Three types of band alignments at the interface of semiconductor heterojunctions: straddling gap (type-I), staggered gap (type-II) or broken gap (type-III). 56

6.7 (a) Schematic diagram of the type-II band alignment with donor band gap (E_g) and conduction band offset (ΔE_c). VBM and CBM stand for valence band maximum and conduction band minimum, respectively. (b) Power conversion efficiency contour plot as a function of the donor band gap (E_g) and conduction band offset (ΔE_c). 57

6.8 The standard AM1.5G solar spectrum with respect to (a) the wavelength (nm) and (b) the photon energy (eV). From Ref. [91]. 58

7.1 (a) Side view of MoS_2 bulk and single layer (analogous for WS_2). (b) Top view of MoS_2 (analogous for WS_2) with the unit cell delineated. The interaction between layers is dominated by vdW forces. The hexagonal lattice similar to graphene is clearly seen in (b). The primitive vectors are $\vec{a} = (a,0,0)$, $\vec{b} = (-a/2, \sqrt{3}a/2, 0)$, and $\vec{c} = (0,0,c)$. According to experimental data [94], $a = 3.15$ and $c = 12.3$ Å for MoS_2; $a = 3.153$ and $c = 12.323$ Å for WS_2. 62

7.2 (a) A monolayer MoS_2 field-effect transistor (FET) connected to external electrodes. MoS_2 is deposited on a degenerately doped silicon substrate with 270-nm-thick SiO_2. The substrate acts as a back gate. One of the gold electrodes acts as drain and the other source electrode is grounded. The monolayer is separated from the top gate by 30 nm of ALD-grown HfO_2. The top gate width for the device is 4 mm and the top gate length, source-gate and gate-drain spacings are 500 nm. (b) Room temperature transfer characteristic for the FET with 10 mV applied bias voltage V_{ds}. Back-gate voltage V_{bg} is applied to the substrate and the top gate is disconnected. Inset: I_{ds}-V_{ds} curve acquired for V_{bg} values of 0, 1 and 5 V. From Ref. [95]. 63

7.3 (a) The hexagonal lattice and corresponding 2D Brillouin zone for MoS_2 or WS_2. (b) Along the high symmetry lines in the Brillouin zone, DFT calculated electronic band structures of (b) MoS_2 and (c) WS_2 from the bulk (bottom panels) to double-layer (2L, middle panels) to single-layer (1L, top panels). The solid blue arrows indicate the lowest energy transitions. The Fermi level is set at 0 eV. 64

7.4 (a) Photoluminescence (PL) spectra normalized by Raman intensity for MoS_2 layers with different thickness, showing a dramatic increase of luminescence efficiency in MoS_2 monolayer. From Ref. [102]. (b) Photoluminescence map of a WS_2 triangular island. The edges of WS_2 monolayers exhibit PL signals with extraordinary intensity, around 25 times stronger than that at the platelets center. From Ref. [103]. 65

7.5 (a) Schematic of Raman-active modes E^1_{2g} and A_{1g} of bulk MoS_2. (b) Raman spectra of thin (nL) and bulk MoS_2 films. (c) Frequencies of E^1_{2g} and A_{1g} (left vertical axis) and their difference (right vertical axis) as a function of layer thickness. From Ref. [105]. 65

7.6 Raman spectra of MoS_2 films from (a) Ref. [105], (b) Ref. [106] and (c) Ref. [98]. 66

8.1 (a) Side view of MoS_2 bulk and single layer (1L in short). (b) Top view of MoS_2 with the unit cell delineated (analogous for WS_2). (c) Heterostructure consisting of 1L MoS_2 and 1L WS_2. Electronic band structures of (d) 1L MoS_2, (e) 1L WS_2 and (f) the heterostructure shown in (c). The solid blue arrows indicate the lowest energy transitions. In (f), red circles (green squares) correspond to projected bands of the MoS_2 (WS_2) layer with the red (green) dashed arrow showing the layer's lowest energy transition. The Fermi level is set at 0 eV. 69

8.2 DFT calculated thickness dependence of (a) electronic band gaps and (b) dielectric constants of MoS_2 and WS_2. For dielectric tensor ε, non-diagonal elements are zero and $\varepsilon_{xx} = \varepsilon_{yy}$. 73

8.3 (a) *Ab initio* Raman spectra of free-standing n-layer (nL) and bulk MoS_2, with laser polarization $\mathbf{g}_i$=$\mathbf{g}_s$=(1,0,0) and wavelength 488 nm. (b) Schematic of Raman-active modes E^1_{2g} and A_{1g} of bulk MoS_2. (c) Frequencies of E^1_{2g} and A_{1g} (left vertical axis) and their difference (right vertical axis) as a function of layer number. (d) Peak intensities of E^1_{2g} and A_{1g} (left vertical axis) and their intensity ratio (right vertical axis) as a function of thickness. 74

8.4 (a) *Ab initio* Raman spectra of free-standing n-layer (nL) and bulk WS_2, with laser polarization $\mathbf{g}_i$=$\mathbf{g}_s$=(1,0,0) and wavelength 488 nm. (b) Schematic of Raman-active modes E^1_{2g} and A_{1g} of bulk WS_2. (c) Frequencies of E^1_{2g} and A_{1g} (left vertical axis) and their difference (right vertical axis) as a function of layer number. (d) Peak intensities of E^1_{2g} and A_{1g} (left vertical axis) and their intensity ratio (right vertical axis) as a function of layer number. 75

8.5 Raman spectra of (a) single-layer and (c) bulk MoS_2 with laser polarization $\mathbf{g}_i$=$\mathbf{g}_s$=(cos θ,0,sin θ). Raman spectra of (b) single-layer and (d) bulk MoS_2 with laser polarization $\mathbf{g}_i$=(1,0,0) and $\mathbf{g}_s$=(cos θ,sin θ,0). In (a) and (c), some of Raman spectra are scaled for comparison purpose. The inset figures show the intensity ratio between E^1_{2g} and A_{1g} as a function of θ. 77

8.6 Raman spectra of (a) single-layer and (c) bulk WS_2 with laser polarization $\mathbf{g}_i$=$\mathbf{g}_s$=(cos θ,0,sin θ). Raman spectra of (b) single-layer and (d) bulk WS_2 with laser polarization $\mathbf{g}_i$=(1,0,0) and $\mathbf{g}_s$=(cos θ,sin θ,0). In (a) and (c), some of Raman spectra are scaled for comparison purpose. The inset figures show the intensity ratio between E^1_{2g} and A_{1g} as a function of θ. 79

8.7 (a) A MoS_2/WS_2 heterostructure. For simplicity, a MoS_2 (WS_2) layer is denoted as Mo (W). So the heterostructure is named as MoWMoW for its stacking pattern. (b) *Ab initio* Raman spectra of various MoS_2/WS_2 heterostructures, with laser polarization $\mathbf{g}_i$=$\mathbf{g}_s$=(1,0,0) and wavelength 488 nm. The Raman spectra of single-layer MoS_2 (Mo) and WS_2 (W) are also shown for comparison. 81

9.1 (a) Phase diagram of $Ca(Fe_{1-x}Co_x)_2As_2$. Inset is the schematic view of the orthorhombic unit cell with spin structure; (b) STM topography of stripe-ordered surface on $CaFe_2As_2$ at (V_{bias} = 1.0 V, I_t = 200 pA). Inset is the zoom-in image, where the red rectangle shows the (1×2) unit cell. 88

9.2 (a) LEED pattern on the surface of $CaFe_2As_2$ (120 eV); (b-g): Six possible structural models for the stripe (1×2) phase for Ca- or As- termination. . . . 90

9.3 (a) Surface structure determined by LEED I-V analysis; (b) DFT calculated structure with AFM ordering identical to bulk; (c) Bader charge difference between surface and bulk atoms both with AFM ordering. The yellow arrows represent spins while the black arrows indicate the distortion with respect to the bulk; (d) Bader charge difference of surface atoms with (W) and without (W/O) AFM ordering. 92

9.4 (a) Averaged STS taken from the clean stripe (1×2) surface of $Ca(Fe_{0.925}Co_{0.075})_2As_2$ at the indicated temperatures; (b) & (c) STM topographic images taken at 20 K and 7.4 K, respectively (V_{bias} = 1.0 V, I_t = 200 pA). The profiles along indicated lines in (b) and (c) are shown in (d). 95

ACKNOWLEDGMENT

First of all, I would like to thank my family for being always supportive, especially willing to allow me to go abroad for my Ph.D. study. I am grateful that my parents taught me perseverance and diligence, helping me through challenges and eventually getting me there for my Ph.D. degree.

There goes an old Chinese saying: “Once a teacher, always a father”. If anybody has been more helpful and inspiring than my parents, that would be my advisor Prof. Vincent Meunier. I am very grateful that I can have him as my mentor for my Ph.D. stud. He has not only taught me how to do research, but also let me realize that doing research can be a lot of fun. His insights on science are very enlightening and his easy-going personality helps to alleviate the pressure from research. Above all, he always stands on my side and cares what is in the best interest of me. I feel truly lucky to have such wonderful advisor.

I also thank Dr. Eduardo Cruz-Silva and Dr. Eduardo Costa Girão a lot for always being available for technical assistance. They helped me through the learning curve when I just began research. As a Postdoc, Dr. Cruz-Silva is both knowledgeable and patient, teaching me many things such as Linux operating, scripting, paper writing and even driving, etc. Dr. Girão has been also extremely helpful for teaching me using Latex, fortran coding and so on. Especially, his Ph.D. thesis has been of great help for me to write up this dissertation. Without their help, life would be much more difficult for me. I would also like to thank other group members: Zac Bullard, Jonathan Owens, Pan Zhu and Adrien Nicolai. I feel very lucky to have them as both colleagues and friends.

I also thank all the members of the Physics department, whose teachings have made old subjects clear with new light. I am also grateful for RPI giving me the opportunity to pursue higher education with such excellent faculty and facilities. I also thank New York State NYSTAR for financial support.

ABSTRACT

Since its fabrication in 2004, graphene has attracted huge attention due to its exceptional electronic properties, and is now considered as one of the most promising candidates to replace the current semiconductor technology as silicon approaches its miniaturization limit. However, the absence of an electronic band gap in pristine graphene makes it ill-suited for many electronic applications. Semiconducting character can be imparted by a variety of methods, including chemical or structural modifications. For instance, a band gap can be opened by confining the electronic wave function in one dimension by cutting graphene to form graphene nanoribbons (GNRs). To possess a band gap comparable to conventional semiconductors like silicon, GNRs are required to have a width less than 3 nm and must also display sharp edges, which remains a great experimental challenge. Recently, a breakthrough advance has been achieved with the controlled synthesis of atomically precise nanoribbons using a bottom-up approach where small aromatic molecules chemically assemble into high-quality subnanometer ribbons. This method not only allows for the synthesis of high-quality straight GNRs, but also for more complex structures like wiggle-like GNRs, called graphene nanowiggles (GNWs).

In Part I of this thesis, first-principles density functional theory (DFT) calculations are carried out on a variety of GNWs to reveal their unusual electronic and magnetic properties that are absent in their individual GNRs components, such as tunable band gaps and versatile magnetic states. The relationship between the band gap and the geometry is dictated by the armchair or zigzag characters of the corresponding parallel and oblique sectors, enabling GNWs to offer a broader set of geometrical parameters to tune the electronic structures compared to GNRs. In addition, first-principles many-body Green's function calculations within the *GW* approximation are performed to yield a quantitative prediction of GNWs' electronic properties. The enhanced electron-electron interaction in the quasi-one-dimensional GNWs results in significant self-energy corrections to their DFT band gaps. Consequently, the quasiparticle band gaps are typically more than twice of the DFT band gaps and are within the most interesting range 0.0-3.7 eV.

In addition to unusual electro-magnetic properties, GNWs are also found to pos-

sess significantly enhanced thermoelectric performance compared to their straight GNR counterparts. The thermoelectric performance can be quantified by a dimensionless figure of merit ZT. Peak ZT values of armchair-armchair GNWs are more than triple those of straight armchair-edged GNRs of the same width. The highest ZT at room temperature for pristine GNWs is 0.79. A certain pattern of structural dislocation in the the experimentally available GNW is found to further enhance ZT beyond 1 at room temperature.

The electronic, magnetic and thermal properties discussed above are found for free-standing GNWs. In reality, however, they are synthesized on a gold substrate. For the experimentally fabricated GNW, a band gap reduction due to the substrate has been measured. DFT calculations reveal that a small net charge transfer from the GNW to the substrate results in an electric dipole at the interface and subsequently substrate polarization. A semi-empirical image charge model is then developed to estimate the observed band gap reduction by substrate polarization. Furthermore, a particular armchair-zigzag GNW is chosen as a case study to verify the magnetic robustness of GNWs on gold substrate. Spin-polarized DFT calculations show that the magnetic configurations are not affected by the substrate with magnetic strength only slightly weakened.

In addition to pristine GNWs, nitrogen-doped GNWs have been also synthesized, as reported recently in the literature. Subsequently, heterojunctions consisting of pure and nitrogen-doped GNWs have been realized. In the final chapter of Part I, the electronic and transport properties of these heterojunctions are studied. Nitrogen doping results in a type-II band alignment at the heterojunction interface, which subsequently reduces the electronic band gap of the heterojunction while increasing the transport gap. More interestingly, as the nitrogen doping concentration increases, both the conduction and valence band offsets at the interface increase almost linearly. Furthermore, the type-II band alignments can be used for solar cell applications. The recently synthesized GNW heterojunction is estimated to have a maximum power conversion efficiency of 11.3%, hence very promising for photovoltaics.

In Part II of this thesis, we venture beyond graphene-based systems and investigate graphene-like materials: transition metal dichalcogenides MX_2 (M = Mo, W; X = S). Similar to graphite, they are also layered structures stacked by weak van der Waals (vdW) forces. Single-layer MoS_2 and WS_2 have been synthesized and found to show enhanced

carrier charge mobilities and strong photoluminescence with direct band gaps, and thus they have been considered as replacements or complements to graphene for applications. Raman spectroscopy is often considered as one of the most popular tools to characterize them. Despite extensive experimental Raman studies on MoS_2 and WS_2, it remains unclear how Raman intensities and especially intensity ratio of Raman modes E^1_{2g} and A_{1g} depend on the materials thickness, due to the large spectrum of seemingly contradictory findings.

To clarify such issues, for both MoS_2 and WS_2, DFT calculations have been carried out to simulate their Raman spectra and reveal the intrinsic thickness dependence of Raman intensities and intensity ratio. We quantitatively analyze the laser polarization effect on the intensity ratio and reveal the high sensitivity of the intensity ratio to laser polarization. The intensity ratio can be tuned from 0 to infinity by adjusting laser polarization, which could be key to explaining the large apparent discrepancy between measured intensity ratios by different experimental groups where different laser polarization configurations might be used.

In addition to homogeneous systems, MoS_2/WS_2 heterostructures can show combined functionality of the individual layers, can lead to emergent properties and thus are very desirable. Hence, we also study *ab initio* Raman spectra of MoS_2/WS_2 heterostructures up to four layers in every possible combinations and stacking orders. Each heterostructure configuration is found to possess a unique Raman spectrum in both frequency and intensity that can be explained by changes in dielectric screening and interlayer coupling. The results establish a set of guidelines that can be used for the experimental identification of heterostructure configurations.

In the final part of the thesis (Part III), we highlight the experimental collaboration project with Prof. Plummer's group from Louisiana State University: spin-dependent surface reconstruction of layered Fe-based superconductors $CaFe_2As_2$. Low energy electron diffraction, scanning tunneling microscopy and spectroscopy, and first-principles spin-polarized DFT are utilized to investigate the geometric, electronic, and magnetic structures of the stripe-ordered (1×2) surface of $Ca(Fe_{1-x}Co_x)_2As_2$ $(x = 0, 0.075)$. The surface is terminated with a 50% Ca layer. Compared to the bulk, the surface Ca layer has a large inward relaxation ($\sim$ 0.5 Å), and the underneath As-Fe_2-As layer displays a significant

buckling. First-principles calculations show that the (1×2) phase is stabilized by the bulk anti-ferromagnetic spin ordering through the spin-charge-lattice coupling. Strikingly, a superconducting gap ($\sim$7 meV at 7.4 K) is observed on such surface ($x = 0.075$ compound), suggesting the coexistence of both superconductivity and AFM ordering at the surface.

1. List of computational methods

This chapter lists the computational methods used and developed in this thesis. The details regarding each method are given in relevant chapters. The purpose of this chapter is to indicate the readers where to find the details on each method.

1.1 Density functional theory

First-principles density functional theory (DFT) is the main theoretical tool used in this thesis. The theoretical background of DFT is presented in Section 3.3. The details about how to perform plane-wave DFT calculations using "Vienna Ab initio simulation package" (VASP) are presented in Section 3.3, Section 4.2, Section 5.2, Section 8.2 and Section 9.2. We also carried out localized orbital DFT calculations using "Spanish Initiative for Electronic Simulations with Thousands of Atoms" (SIESTA), as shown in Section 6.2.

1.2 Many-body *GW* approximation

Since the Kohn-Sham scheme of DFT is a ground state theory using single-particle descriptions, it is well-known to usually underestimate band gaps of low-dimensional systems. Therefore, first-principles many-body Green's function calculations within the *GW* approximation have been also performed to provide more accurate description of band gaps in Section 3.5.

1.3 Tight-binding and Hubbard model

For systematic studies on hundreds of GNWs, DFT is too computationally demanding and thus a less expensive self-consistent tight-binding+Hubbard model has been developed in Subsection 3.3.2.

1.4 The computation of the thermoelectric figure of merit

The formalism to compute the thermoelectric figure of merit ZT based on the full electron and phonon band structures is presented in Section 4.2.

1.5 Image charge model for band gap reduction

To estimate the substrate polarization-induced band gap reduction, a semi-empirical image charge model is developed in Subsection 5.3.4.

1.6 Non-equilibrium Green's function formalism

The non-equilibrium Green's function (NEGF) formalism to calculate electronic transport properties is detailed in Subsection 6.2.1.

1.7 The computation of power conversion efficiency of a solar cell

For an excitonic solar cell with a type-II staggered band alignment, the theoretical model to estimate the maximum power conversion efficiency is developed in Section 6.4.

1.8 Non-resonant first-order Raman scattering

We present the details pertaining to the formalism of non-resonant first-order Raman scattering in Section 8.2.

PART I

Graphene-based materials: graphene nanowiggles

2. Background on graphene and graphene-based materials

This chapter provides a brief overview of graphene and graphene-derived materials. After a brief introduction of two-dimensional graphene sheets and one-dimensional graphene nanoribbons, we highlight the particular systems carefully studied in this thesis, namely graphene nanowiggles. Parts of this chapter are inspired by Dr. Girão's Ph.D. thesis [1].

2.1 Graphene sheets

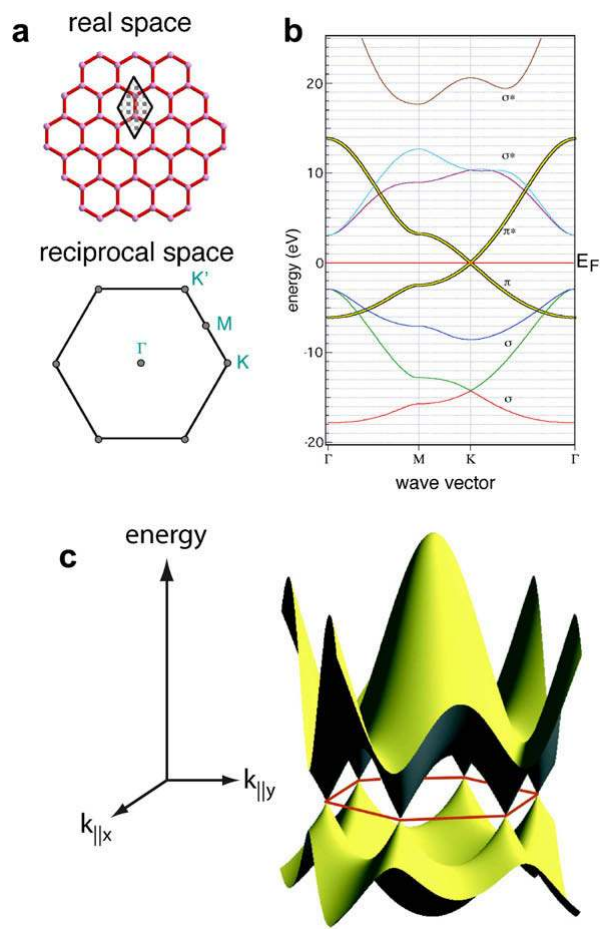

Figure 2.1: (a) Graphene and its 2D Brillouin zone. (b) Band structure of graphene along high symmetry directions. (c) 3D representation of the π bands with the Dirac points at the K point. Graphene is hence a zero-gap semiconductor or semi-metal. From Ref. [2].

Graphene is a two-dimensional (2D) single-layer sheet of carbon atoms packed into

a honeycomb lattice, as shown in Fig. 2.1(a). The first experimental isolation of graphene from graphite was accomplished in 2004 [3], marking the starting point of a boom in both experimental and theoretical investigations of this structure. In Fig. 2.1(b), its 2D band structure shows the π bands crossing the Fermi level at the K point. Near this point, the energy has a linear dependence on the wave vector k. The dependence on the 2D wave vector $k = (k_x, k_y)$ is conical as can be seen from the 3D rendition of the band structure in Fig. 2.1(c). Due to this local linear relation for low-energy levels, the electrons behave as massless Dirac fermions [4]. In addition to such extraordinary electronic feature, graphene also has exceptional electrical [3, 5, 6], optical [7, 8], thermal [9, 10] and mechanical [11] properties. For instance, it has been found that graphene exhibits high room temperature carrier mobility (15000-27000 $cm^2V^{-1}s^{-1}$) [12], quantized electrical conductance, high Seebeck coefficient [13], superior room temperature thermal conductivity as high as 5 kW/mK. All these striking properties are making graphene a rising star in material science.

2.2 Graphene nanoribbons

The rich properties of graphene, particularly its high electronic mobility and low contact resistance [12, 14], have made it one of the most promising candidates to replace silicon technology as silicon approaches its miniaturization limit [15]. However, the absence of an electronic band gap for pristine graphene [Fig. 2.1(b)] limits its applicability in the semiconductor industry. However, it can be chemically [16] or structurally [17] modified to acquire semiconducting properties. One widely studied approach is to induce quantum confinement along one in-plane direction, thus creating quasi-one-dimensional structures called graphene nanoribbons (GNRs). The two most symmetric cases of GNRs are armchair-edged GNRs (AGNRs) and zigzag-edged GNRs (ZGNRs), as presented in Fig. 2.2.

AGNRs present a semiconductor character with band gap Δ_n strongly dependent on the number of C-C lines along its width. The gap Δ_n of an AGNR approaches zero with its width $n \to \infty$, so it recovers as 2D graphene. More interestingly, the function of Δ_n versus n has three separate branches such that $\Delta_{3i+1} \geq \Delta_{3i} \geq \Delta_{3i+2}$ [18].

Unlike AGNRs where spin polarization is absent, ZGNRs possess ferromagneti-

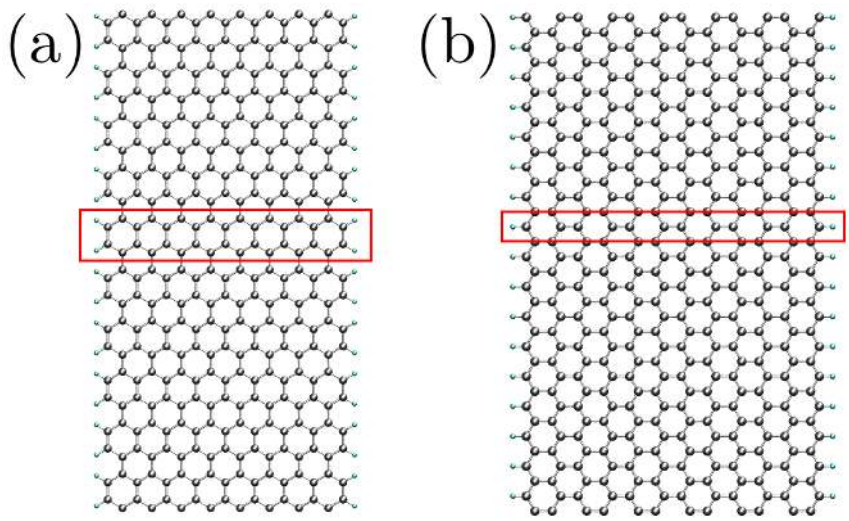

Figure 2.2: Geometry of (a) AGNRs and (b) ZGNRs with edges hydrogenated. The red boxes indicate the GNRs unit cells. They are periodic along the vertical direction. From Ref. [1].

cally polarized edges with two possibilities for the edge-to-edge polarization: parallel (FM) and anti-parallel (AFM) alignments. Hence, in addition to a non-polarized paramagnetic (PM) state, ZGNRs can have two other possible magnetic configurations, as illustrated in Fig. 2.3. The PM state is the most energetically unstable with a zero band gap, while spin polarization (both FM and AFM) lowers the energy of the structure. For the AFM, the spin up and down polarizations along the opposite edges are located on different graphene-sub-lattices, making it the most stable and opening a band gap around two thirds of the Brillouin zone, while the FM state has a slightly higher energy. It is important to note that both AFM and FM are considerably more stable than the PM state, while there is only small energy difference between AFM and FM. This difference tends to be zero as the ZGNRs' width increases, reflecting a decrease in the edge-to-edge interaction as they are farther away from each other. A possible switching property due to this small energy difference opens a window for the application of ZGNRs as magnetic sensors [19].

Indeed, these magnetic properties of ZGNRs open up a series of possibilities for the use of finite pieces of graphene in nanoelectronics and spintronics. For example, it has been shown that ZGNRs can present a half-metallicity behavior. The electronic structure has a metallic character for spin up levels and is semiconducting for spin down levels, or

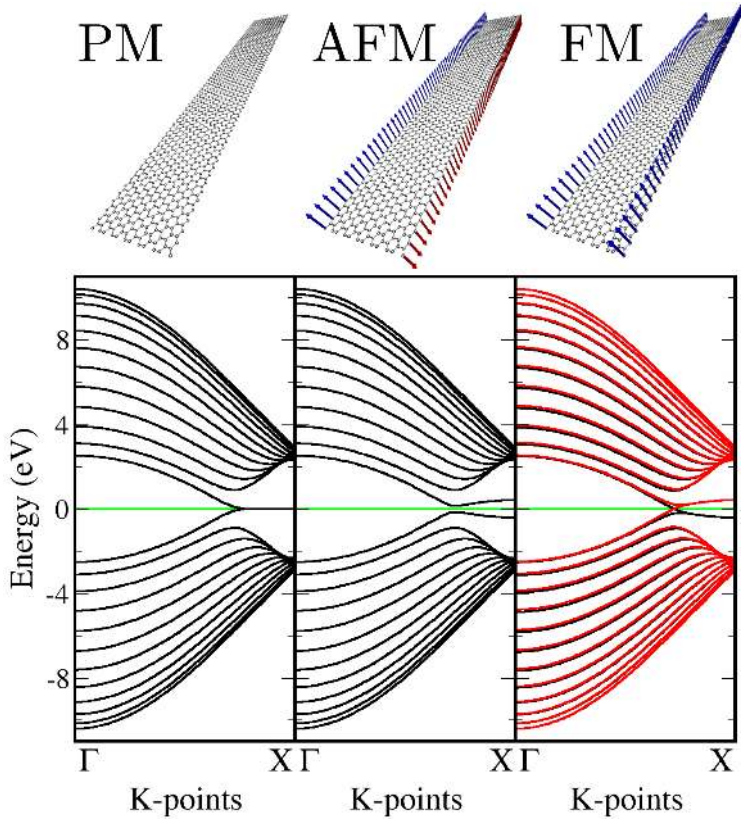

Figure 2.3: Paramagnetic (PM), anti-ferromagnetic (AFM) and ferromagnetic (FM) states in a ZGNR and their corresponding band structures. The green line is the Fermi energy, and the black and red lines stand for spin up and down levels. All the bands are degenerate in PM and AFM states. From Ref. [1].

vice-versa, which can be utilized for spin-filtering [20].

2.3 Graphene nanowiggles

To realize the aforementioned properties of GNRs for practical technological applications, GNRs must have a width less than 3 nm with clean edges. However, it remains a great experimental challenge to have reliable production of narrow GNRs with sharp edges. To that end, a set of synthesis techniques, including both top-down and bottom-up approaches, has been developed to enable the precise and controlled fabrication of narrow and defect-free systems [23]. Most notably, a block-to-block approach has been recently devised where small aromatic molecules are chemically assembled into highly crystalline narrow ribbons [21]. In this method, a cyclo-dehydrogenation reaction proceeds on a metallic substrate that facilitates both the coupling and the thermally-activated

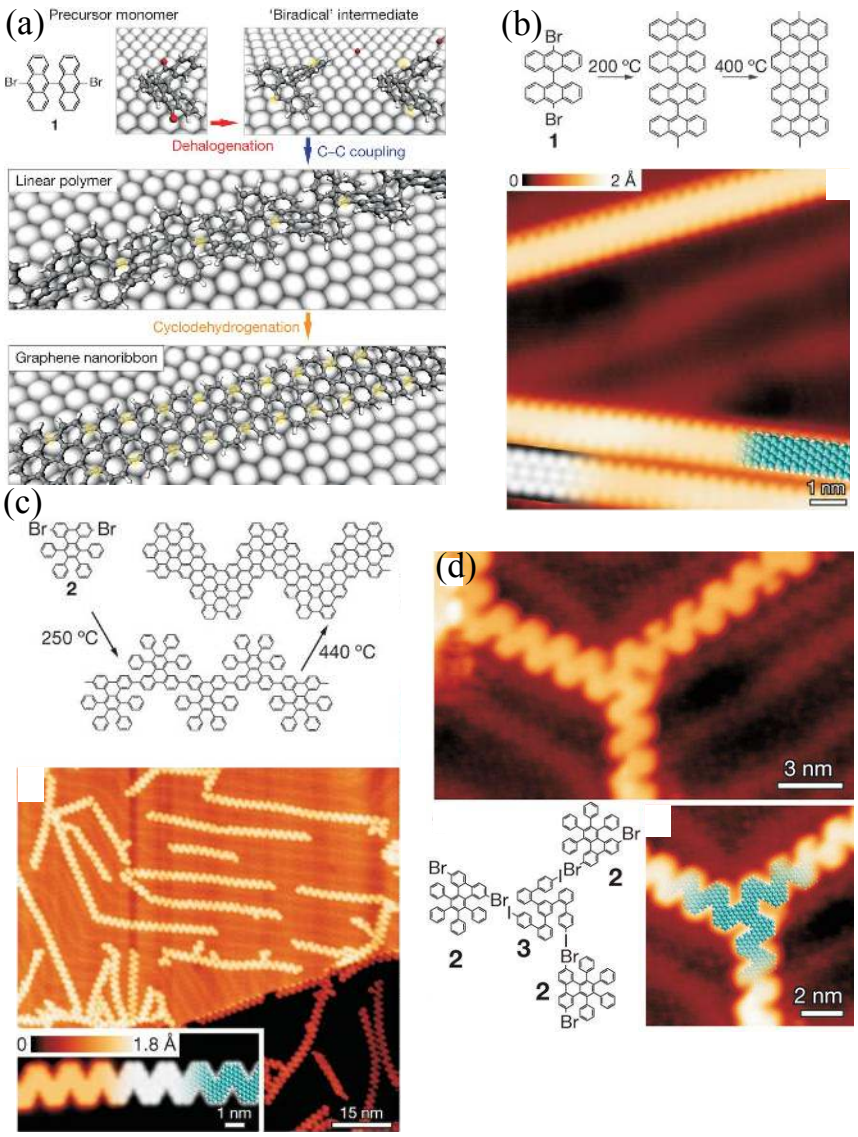

Figure 2.4: (a) Bottom-up fabrication of atomically precise GNRs. Basic steps for surface-supported GNR synthesis, illustrated with a ball-and-stick model of the example of 10,10′-dibromo-9,9′-bianthryl monomers. (b) Straight GNRs from bianthryl monomers and the high-resolution STM image. (c) Chevron-type GNRs from tetraphenyl-triphenylene monomers and the high-resolution STM image. (d) Three-fold GNR junction obtained from a 1,3,5-tris(4″-iodo-2′-biphenyl) benzene monomer 3 at the nodal point and monomer 2 for the ribbon arms, and its STM image. From Ref. [21].

fusion of individual aromatic molecules, as illustrated in Fig. 2.4(a). This method not only allows for the synthesis of high-quality straight GNRs shown in Fig. 2.4(b), but has also demonstrated the possibility of creating more complex structures, with a variety of shapes such as wiggle-like (or chevron-type) GNRs [Fig. 2.4(c)] and multiterminal

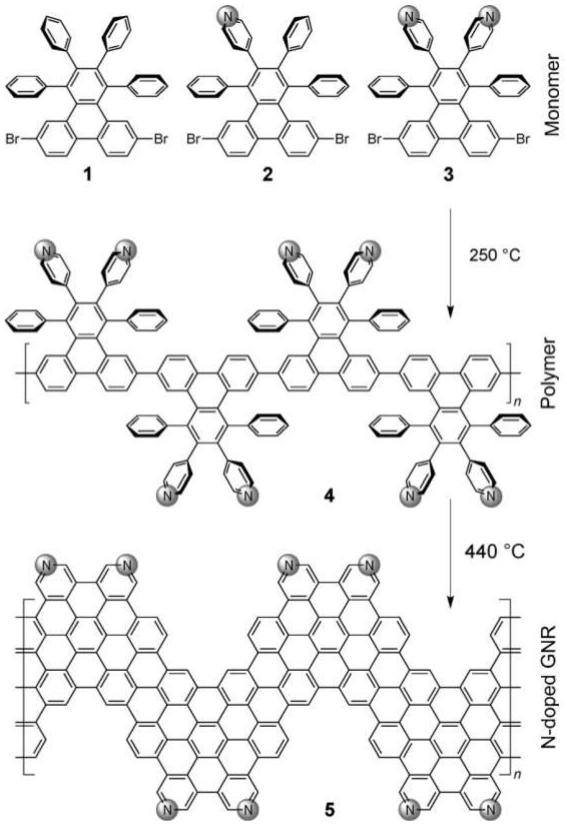

Figure 2.5: Monomers for the generation of graphene nanowiggles with defined edge-doping via on-surface polymerization followed by cyclo-dehydrogenation. Shown are monomers 1-3 with either none, one or two doping N-atoms, while the synthesis is exemplarily shown for the case of the doubly nitrogen-doped GNW. From Ref. [22].

GNRs [Fig. 2.4(d)]. The wiggle-like GNRs in Fig. 2.4(c), namely graphene nanowiggles (GNWs), can be characterized by a periodic repetition of GNRs junctions. The GNW experimentally fabricated shows electronic properties different from its individual GNRs components, owing to its unique wiggle-like edges [21].

As mentioned above, the building blocks of GNWs are individual aromatic molecules called monomers. By doping monomers with nitrogen atoms in the first place and using them as building blocks (Fig. 2.5), nitrogen-doped GNWs with an atomically precise edge structure and doping pattern have been synthesized recently [22]. Furthermore, by using both pure and nitrogen-doped monomers as building blocks, heterojunctions combining segments of pure GNWs (p-GNWs) and nitrogen-doped GNWs (N-GNWs) have been also synthesized (denoted as p-N-GNW heterojunctions) [24].

2.4 Overview for the rest of Part I

Inspired by the major experimental advance discussed above, in the rest of Part I of this thesis, we consider numerous GNWs beyond the one synthesized. In Chapter 3, we develop a general framework to classify nanowiggles according to their geometries and employ the first-principles density functional theory and tight-binding+Hubbard model to reveal their unusual electronic and magnetic properties which conventional GNRs do not possess. Also, in light of the fact that DFT Kohn-Sham band gap often fails to quantitatively match experimental data, a first-principles many-body Green's function approach within the *GW* approximation is utilized to provide more accurate description of GNWs' band gaps. In Chapter 4, we then demonstrate that GNWs also possess superior thermoelectric properties compared to their straight GNR counterparts. We also present a systematic study to establish how geometry and spin states influence ZT at room temperature. Chapter 5 is dedicated to an investigation of substrate effects on electronic and magnetic properties of GNWs. Finally, in Chapter 6, we investigate the electronic and transport properties of p-N-GNW heterojunctions, which show type-II band alignments for excitonic solar cell applications.

3. Electronic and magnetic properties of GNWs

In this chapter we present a detailed description about geometry and nomenclature of GNWs. Then we use first-principles density functional theory to highlight the microscopic origins of the emerging electronic and magnetic properties of GNWs [25]. A tight-binding+Hubbard model is also developed for a systematic study on how geometry and spin influence the electronic band gaps [26]. Finally, a first-principles many-body Green's function approach within the *GW* approximation is employed to yield more accurate quasiparticle band gaps of GNWs [27].

3.1 Introduction

As mentioned in Chapter 2, an atomically precise bottom-up approach has been developed by Cai *et al.* [21] to chemically assemble small aromatic molecules into high-quality subnanometer ribbons, including the novel GNWs. They can be characterized by a periodic repetition of GNR junctions. Motivated by the development of this practical synthesis technique, we here consider a variety of GNWs beyond the experimentally fabricated one to explore what these new structures can bring.

3.2 Geometry and nomenclature

GNWs consist in successive repetitions of parallel and oblique (relative to the GNWs periodic direction) GNR domains seamlessly stitched together without the need of structural defects [Fig. 3.1(a)]. Parallel (P) and oblique (O) sectors can be either armchair- (A) or zigzag- (Z) edged, leading to four types of GNWs: armchair-armchair (AA), armchair-zigzag (AZ), zigzag-armchair (ZA) and zigzag-zigzag (ZZ), as shown

---

Portions of this chapter previously appeared as: E. C. Girão, L. Liang, E. Cruz-Silva, A. Filho, and V. Meunier, Phys. Rev. Lett. **107**, 135501 (2011).
Portions of this chapter previously appeared as: E. C. Girão, E. Cruz-Silva, L. Liang, A. Souza Filho, and V. Meunier, Phys. Rev. B **85**, 235431 (2012).
Portions of this chapter previously appeared as: L. Liang, E. C. Girão, and V. Meunier, Phys. Rev. B **88**, 035420 (2013).

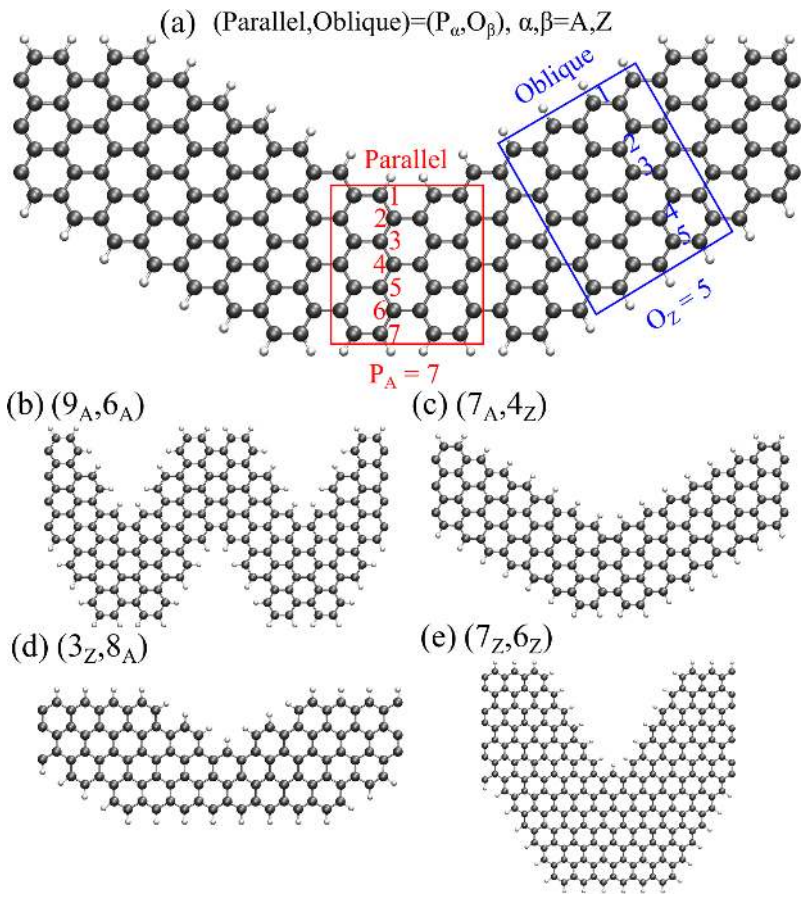

Figure 3.1: (a) Geometry and nomenclature of a hydrogenated GNW made up of successive parallel (P) and oblique (O) sectors with armchair- (A) or zigzag- (Z) edged geometries. (b)-(e) Examples of an AA, AZ, ZA and ZZ GNW, respectively. They are periodic in the horizontal direction.

in Figs. 3.1(b-e), respectively. Following the conventional notation used for straight nanoribbons, we define the width of the parallel (P_α) and oblique (O_α) sectors by the number of C-C dimer lines ($\alpha = A$) or zigzag strips ($\alpha = Z$) along their width, depending on whether these are armchair or zigzag sectors. Therefore, each structure can be uniquely identified by a (P_α,O_β) notation. For example, for the GNW in Fig. 3.1(a), the widths of armchair-edged P and zigzag-edged O sectors are $P_A = 7$ and $O_Z = 5$, respectively. So it is uniquely identified as (7_A,5_Z). The nanowiggle reported experimentally [21] is shown in Fig. 3.1(b) and is made of armchair parallel and armchair oblique sectors (type AA) with widths corresponding to (9_A,6_A).

3.3 Theoretical methods

Density functional theory (DFT) is the main theoretical tool used in this thesis. Therefore, before we discuss how to use DFT for a variety of calculations, the theoretical background of DFT is presented below, parts of which are inspired by Dr. Girão's Ph.D. thesis [1].

3.3.1 Density functional theory

In DFT, the electronic density $n(\mathbf{r})$ plays the central role. This is better understood with the two Hohenberg-Kohn theorems which constitute the basis of DFT [28].

1.If two systems of interacting electrons, one trapped in an external potential V_1 and the other in V_2, have the same ground state density $n(\mathbf{r})$, then necessarily $V_1 - V_2 =$ constant.

2. Let $E[n]$ be the functional for the energy relative to the electronic density n for a given external potential V_{ext}. Then this functional has its global minimum (ground state energy) for the exact density n_0 corresponding to the ground state.

Based on the first theorem, all the system properties are determined by the electronic density for the ground state since n_0 determines V_{ext}, which determines the Hamiltonian, which in turn defines the ground state and all the excited states. From the second theorem, we can use the energy functional $E[n]$ to determine the exact ground state energy and density. The energy functional is written as

$$E[n] = T[n] + U[n] + V[n] \tag{3.1}$$

where $T[n]$ is the kinetic energy functional, $U[n]$ accounts for all the electron-electron interactions and $V[n] = \int d\mathbf{r} V_{ext}(\mathbf{r}) n(\mathbf{r})$ is the potential energy functional from the external field. In principle, by the minimization of the functional $E[n]$ with respect to $n(\mathbf{r})$, we can obtain the ground state density n_0 and thus all other ground state observables. However, $U[n]$ is not explicitly known.

The necessary recipe to go around such issue is given by the Kohn-Sham ansatz [29]. The ground state of the system of interacting electrons can be written as the ground state of an auxiliary system of non-interacting electrons. The one-electron wavefunctions

for this auxiliary system are determined by Schrödinger-like equations in the form

$$\hat{H}^{\sigma}_{aux}\psi^{\sigma}_{i}(\mathbf{r}) = -\frac{\hbar^2}{2m_e}\nabla^2\psi^{\sigma}_{i}(\mathbf{r}) + V^{\sigma}\psi^{\sigma}_{i}(\mathbf{r}) = \varepsilon^{\sigma}_{i}\psi^{\sigma}_{i}(\mathbf{r}), \tag{3.2}$$

where σ labels the electron spin. The electronic density is written as

$$n(\mathbf{r}) = \sum_{\sigma}\sum_{i=1}^{N_\sigma}|\psi^{\sigma}_{i}(\mathbf{r})|^2 \tag{3.3}$$

and the corresponding kinetic energy is

$$T_{aux} = -\frac{\hbar^2}{2m_e}\sum_{\sigma}\sum_{i=1}^{N^\sigma}\langle\psi^{\sigma}_{i}|\nabla^2|\psi^{\sigma}_{i}\rangle = \frac{\hbar^2}{2m_e}\sum_{\sigma}\sum_{i=1}^{N^\sigma}\int d\mathbf{r}|\nabla\psi^{\sigma}_{i}(\mathbf{r})|^2. \tag{3.4}$$

The classical Coulomb interaction is

$$E_{Hartree}[n] = \frac{1}{8\pi\varepsilon_0}\int\int d\mathbf{r}d\mathbf{r}'\frac{n(\mathbf{r})n(\mathbf{r}')}{|\mathbf{r}-\mathbf{r}'|} \tag{3.5}$$

and hence the Kohn-Sham energy functional is given as

$$E_{KS}[n] = T_{aux}[n] + \int d\mathbf{r}V_{ext}(\mathbf{r})n(\mathbf{r}) + E_{Hartree}[n] + E_{xc}[n], \tag{3.6}$$

where E_{xc} is the functional which accounts for the exchange and all the correlation effects. If we consider $E = E_{KS}$, we have

$$E_{xc}[n] = T[n] - T_{aux}[n] + U[n] - E_{Hartree}[n], \tag{3.7}$$

which indicates that E_{xc} contains the exchange contribution and all the other correlation effects related to kinetic energy and electron-electron interactions. It can be written as

$$E_{xc}[n] = \int d\mathbf{r}n(\mathbf{r})\varepsilon_{xc}([n],\mathbf{r}), \tag{3.8}$$

where $\varepsilon_{xc}([n],\mathbf{r})$ is the exchange-correlation energy per electron at position $\mathbf{r}$ for the given density $n(\mathbf{r})$. One then proceeds with the minimization of the energy functional $E_{KS}[n]$

relative to the density n, and it ends up as

$$\begin{aligned}
&\frac{\delta T_{aux}[n]}{\delta \psi_i^{\sigma *}} + \frac{\delta E_{ext}[n]}{\delta \psi_i^{\sigma *}} + \frac{\delta E_{Hartree}[n]}{\delta \psi_i^{\sigma *}} + \frac{\delta E_{xc}[n]}{\delta \psi_i^{\sigma *}} - \varepsilon_i^{\sigma} \psi_i^{\sigma} \\
= \quad & -\frac{\hbar^2}{2m_e} \nabla^2 \psi_i^{\sigma}(\mathbf{r}) + \left(\frac{\delta E_{ext}[n]}{\delta n(\mathbf{r})} + \frac{\delta E_{Hartree}[n]}{\delta n(\mathbf{r})} + \frac{\delta E_{xc}[n]}{\delta n(\mathbf{r})} \right) \frac{\delta n(\mathbf{r})}{\delta \psi_i^{\sigma *}} - \varepsilon_i^{\sigma} \psi_i^{\sigma} = 0,
\end{aligned} \tag{3.9}$$

resulting in

$$\boxed{-\frac{\hbar^2}{2m_e} \nabla^2 \psi_i^{\sigma}(\mathbf{r}) + \left(V_{ext}(\mathbf{r}) + V_{Hartree}(\mathbf{r}) + \varepsilon_{xc}(\mathbf{r}) \right) \psi_i^{\sigma} = \varepsilon_i^{\sigma} \psi_i^{\sigma}}. \tag{3.10}$$

This is the well-known Kohn-Sham equation for the auxiliary system of non-interacting electrons. It recasts the many-electron problem into a set of one-electron Schrödinger-like equations. The Hartree potential (representing the interaction of any electron with the electronic cloud) is given by

$$V_{Hartree}[n] = \frac{1}{8\pi\varepsilon_0} \int d\mathbf{r}' \frac{n(\mathbf{r})}{|\mathbf{r} - \mathbf{r}'|}, \tag{3.11}$$

and the external potential V_{ext} is also known. But the major problem of DFT is that the exact form of the exchange and correlation energy term E_{xc} (or ε_{xc}) is still not known. Even though DFT, in principle, yields the exact solution for the electronic problem, its practical implementation requires an approximation to E_{xc}.

The widely used approximation is the local density approximation (LDA), where the functional depends only on the density at the coordinate:

$$E_{xc}^{\mathrm{LDA}}[n] = \int d\mathbf{r} n(\mathbf{r}) \varepsilon_{xc}(n). \tag{3.12}$$

LDA tends to work well for homogeneous systems, but for inhomogeneous systems, generalized gradient approximation (GGA) is usually preferred which also takes into account the gradient of the density at the same coordinate:

$$E_{xc}^{\mathrm{GGA}}[n] = \int d\mathbf{r} n(\mathbf{r}) \varepsilon_{xc}(n, \nabla n). \tag{3.13}$$

The well-known GGA functionals include the Perdew-Wang 1991 [30] and Perdew-Burke-Ernzerhof [31]. The meta-GGA is potentially more accurate than the GGA, since it includes the second derivative of the electron density whereas the GGA considers only the first derivative. In addition, hybrid functionals incorporate a portion of exact exchange from HartreeFock theory [32] with exchange and correlation from other sources (*ab initio* or empirical). The most commonly used hybrid functionals include B3LYP (Becke, 3-parameter, Lee-Yang-Parr) [33, 34] and HSE (Heyd-Scuseria-Ernzerhof) [35].

In practical implementations of DFT, a wavefunction can be represented in either plane-wave or localized atomic-orbital basis. In the plane-wave basis, the wavefunction is linear combination of plane waves $e^{i(\mathbf{k}+\mathbf{G})\mathbf{r}}$, where $\mathbf{G}$ corresponds to reciprocal space lattice. The number of plane waves and the basis-set quality are controlled by a single energy-cutoff value. All plane waves in the basis are mutually orthogonal and are not associated with any particular atom. One disadvantage of the plane-wave approach is that the empty space in the supercell requires the same computational cost as the structure. As for the atomic-orbital basis, the wavefunction is described by the numerical atomic orbitals defined on a real-space grid. The localized atomic-orbital approach works more efficiently for molecules since it does not waste computational power on the vacuum. But the atomic-orbital basis is non-orthogonal and depends on atomic positions, which may lead to basis set superposition errors. In this thesis, we have used the VASP package for plane-wave DFT calculations and the SIESTA package for atomic-orbital DFT calculations.

To obtain electronic properties of GNWs systems depicted in Fig. 3.1, plane-wave DFT calculations are performed using the VASP package [36, 37] within GGA using the Perdew-Burke-Ernzerhof (PBE) exchange-correlation functional [31]. Atomic structures are fully relaxed until residual forces below 0.01 eV/Å, using fine k-point samplings within the Monkhorst-Pack scheme [38] and projector augmented wave (PAW) pseudopotentials with a cutoff energy of 400 eV. However, DFT is too computationally demanding to perform a systematic study. Therefore a less expensive self-consistent π band tight-binding+U (TBU) model has been used [25, 39]. Such TBU model is mainly developed by Dr. Girão [26] and the model presented below is inspired by his Ph.D. thesis [1].

3.3.2 Tight-binding+Hubbard model

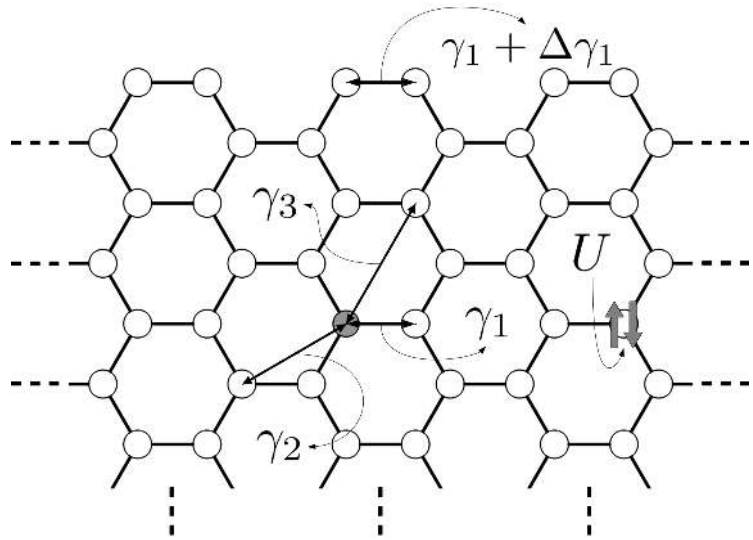

Figure 3.2: Schematic of the first-, second-, and third-nearest neighbor hopping integrals (γ_1, γ_2 and γ_3) on an armchair-edged graphitic structure. The different chemical environment at the edges is accounted for by a modified first neighbor interaction for these frontier atoms. From Ref. [26].

In a tight-binding model, the Hamiltonian is given as:

$$\hat{H}_0 = \sum_{\mathbf{R}}\sum_{i}\sum_{\sigma}|\mathbf{R},i,\sigma\rangle\varepsilon_i\langle\mathbf{R},i,\sigma| + \sum_{\mathbf{R}}\sum_{i}\sum_{\mathbf{R}'}\sum_{j}\sum_{\sigma}|\mathbf{R},i,\sigma\rangle\gamma_{(\mathbf{R},i),(\mathbf{R}',j)}\langle\mathbf{R}',j,\sigma|, \quad (3.14)$$

where $|\mathbf{R},i,\sigma\rangle$ denotes the orbital of atom i with spin σ in the real space cell at $\mathbf{R}$. $\gamma_{(\mathbf{R},i),(\mathbf{R}',j)}$ are the hopping integrals representing the real-space Hamiltonian elements between the orbitals $|\mathbf{R},i,\sigma\rangle$ and $|\mathbf{R}',j,\sigma\rangle$ (with $\gamma_{(\mathbf{R},i),(\mathbf{R},i)} = 0$) and ε_i is the on-site energy representing the real-space Hamiltonian element between the orbital $|\mathbf{R},i,\sigma\rangle$ and itself. Here we consider orthonormal orbitals so that $\langle\mathbf{R},i,\sigma|\mathbf{R}',j,\sigma'\rangle = \delta_{(\mathbf{R},i,\sigma),(\mathbf{R}',j,\sigma')}$.

For carbon based materials, we restrict the orthogonal basis to the π orbital and the interactions are accounted up to 3rd neighbors [19], which means that $\gamma_{(\mathbf{R},i),(\mathbf{R}',j)}$ is non zero only when $|\mathbf{R},i\rangle$ and $|\mathbf{R}',j\rangle$ are no more than 3 neighbors away. This π orbital description implicitly considers that carbon atoms on the edges are saturated with hydrogens. Using the parametrization proposed in Ref. [40], $\gamma_1 = 3.2$ eV, $\gamma_2 = 0$ eV and $\gamma_3 = 0.3$ eV for the first-, second-, and third-nearest neighbor hopping integrals, respectively, as illustrated in Fig. 3.2. The different chemical environment at the edges is accounted for by

including a $\Delta\gamma_1 = 0.2$ eV correction to the γ_1 parameter for the frontier atoms [40].

Furthermore, to consider the interaction between two electrons with opposite spins occupying the same state, a Hubbard-like (U) term is added to the Hamiltonian. This has been shown to reproduce quite well the most relevant physical aspects of magnetic states in a number of graphitic systems, including zigzag-edged GNRs [19]. The Hubbard Hamiltonian $\hat{H}'$ is written in terms of the number operators $\hat{n}_i^{\uparrow}$ and $\hat{n}_i^{\downarrow}$ for the spin-orbitals from atom i as

$$\hat{H}' = U \sum_i \hat{n}_i^{\uparrow} \hat{n}_i^{\downarrow}, \tag{3.15}$$

where the single parameter U corresponds to the on-site Coulomb repulsion. Due to the complexity of the two-body problem, this Hamiltonian is written in a mean-field fashion:

$$\hat{H}' = U \sum_i \left(\langle \hat{n}_i^{\uparrow} \rangle \hat{n}_i^{\downarrow} + \hat{n}_i^{\uparrow} \langle \hat{n}_i^{\downarrow} \rangle \right), \tag{3.16}$$

where the densities $\langle \hat{n}_i^{\uparrow} \rangle$ and $\langle \hat{n}_i^{\downarrow} \rangle$ are determined self-consistently [26]. Here the U is parameterized on DFT-PBE calculations as $0.92\gamma_1$, resulting in an excellent agreement between the DFT and TBU results, as demonstrated in Fig. 3.3.

3.4 Electronic and magnetic properties

In both DFT and TBU calculations, we observe the emergence of multiple magnetic states from GNWs (Fig. 3.3). This finding can be rationalized by the properties of individual armchair- and zigzag-edged GNRs: the ground state of AGNRs is paramagnetic (PM) while ZGNRs' ground state is anti-ferromagnetic (AFM) with possible metastable PM and ferromagnetic (FM) spin configurations, as discussed in Chapter 2. In the rest of this section, we discuss electronic and magnetic properties of each type of GNWs in detail, as well as the corresponding systematic TBU studies.

3.4.1 AA-GNWs

The AA GNW (9_A,6_A) in Fig. 3.1(b), made of both armchair parallel and oblique sectors, only has a PM electronic configuration (Fig. 3.3). A large DFT band gap (1.58 eV) is observed for (9_A,6_A), while DFT band gaps of its individual components AGNR-6 (oblique sector) and AGNR-9 (parallel sector) are 1.08 and 0.76 eV, respectively. This

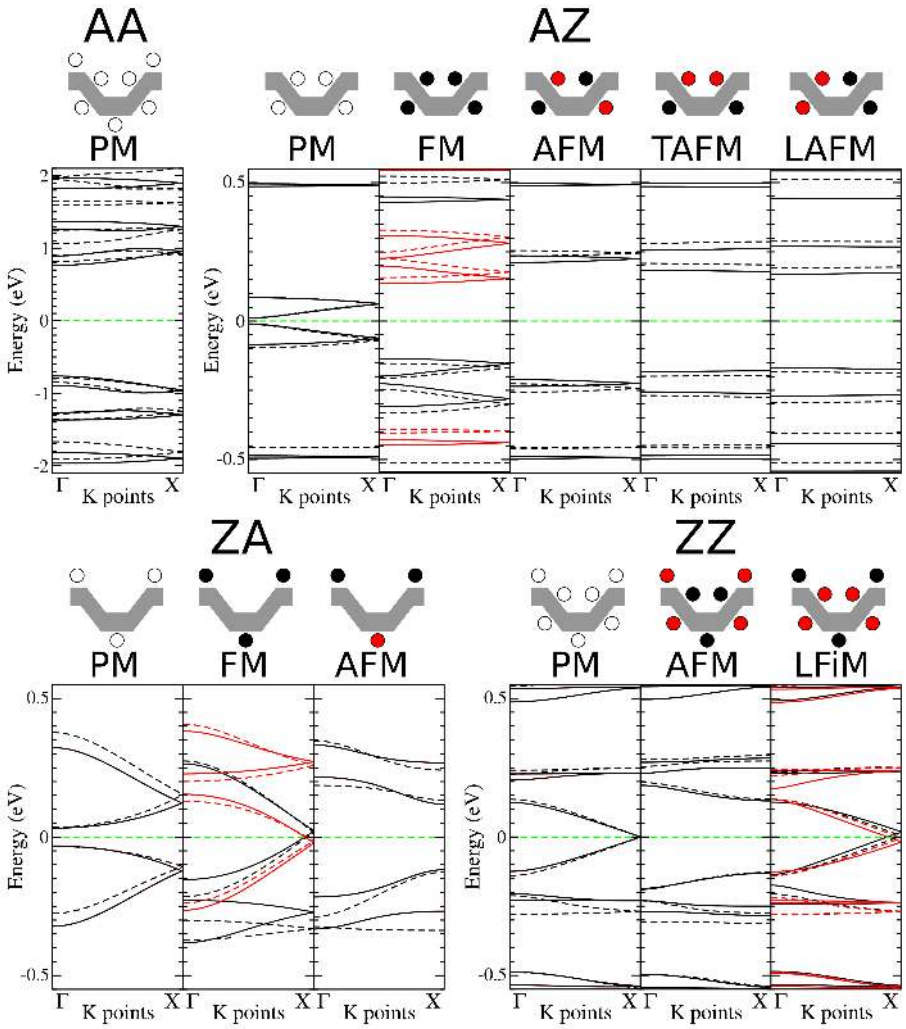

Figure 3.3: TBU (solid lines) and DFT (dashed lines) electronic band structures of different magnetic states for AA (9_A,6_A), AZ (6_A,7_Z), ZA (4_Z,9_A) and ZZ (7_Z,7_Z) GNWs. The schematic spin distributions (black: up, red: down) are shown on top of each panel. The Fermi level is set at 0 eV for each graph.

indicates that the interplay between the parallel and oblique constituents alters electronic properties of the GNW from its constituents. As shown in Fig. 3.3, the TBU model provides a good description of GNWs' electronic structures. This encourages us to conduct a systematic study using TBU in order to understand the relation between electronic structure and geometry for GNWs. The band gaps from TBU calculations are plotted for a variety of AA GNWs as a function of O_A and P_A in Fig. 3.4(a) (O_A and P_A are varied from 4 to 25). They can be classified according the multiple-of-three rules, as evidenced by grids evenly spaced in units of 3. As discussed in Chapter 2, for AGNRs, the en-

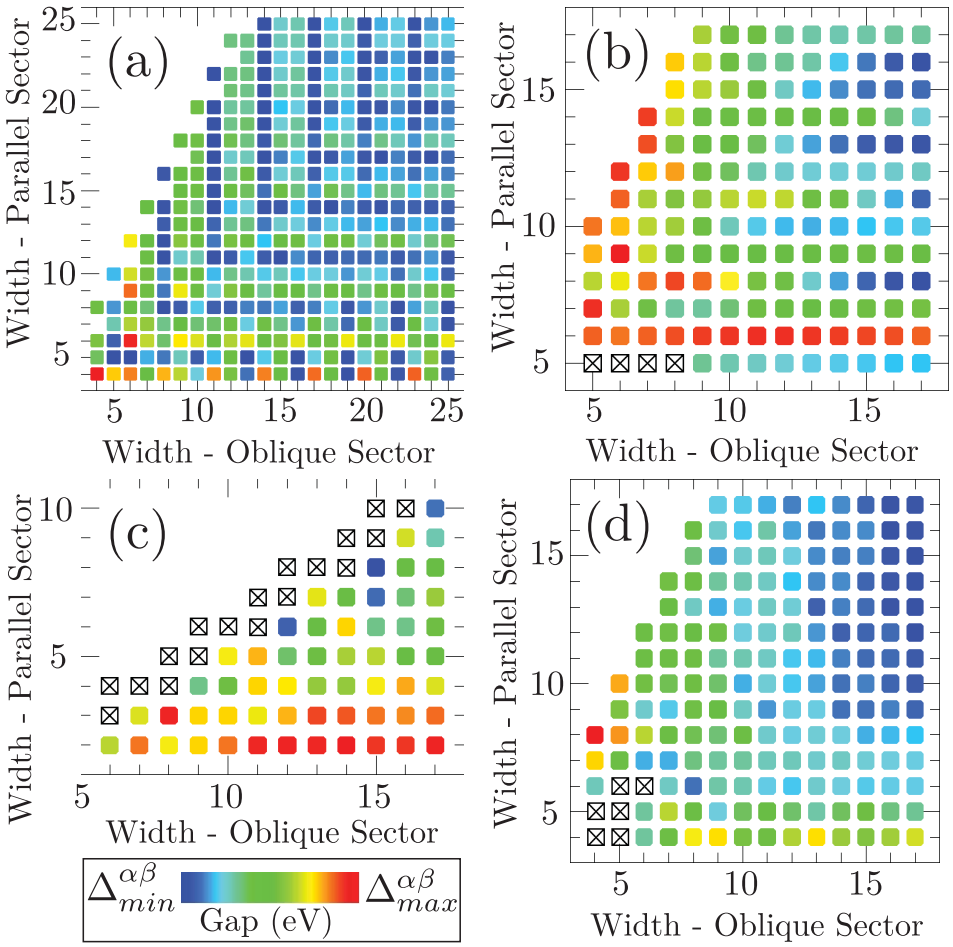

Figure 3.4: TBU energy band gap as a function of the widths of parallel (P) and oblique sectors (O) for (a) AA GNWs in the PM state, and for (b) AZ, (c) ZA and (d) ZZ GNWs in the AFM state. The points absent mainly on the upper-left corner of each graph correspond to geometries not allowed by the particular choice for P and O. For (b)-(d), the systems that do not possess a stable AFM state are marked by a cross. In these charts, the band gap minima and maxima (in unit of eV) are (a) Δ^{AA}_{min}=0.00, Δ^{AA}_{max}=1.70; (b) Δ^{AZ}_{min}=0.18, Δ^{AZ}_{max}=0.45; (c) Δ^{ZA}_{min}=0.11, Δ^{ZA}_{max}=0.48; (d) Δ^{ZZ}_{min}=0.21, Δ^{ZZ}_{max}=0.49.

ergy gap Δ_N with $N = (3i + j)$ C-C lines follows the relation $\Delta_{3i+1} \geq \Delta_{3i} \geq \Delta_{3i+2}$, which also explains why AA GNWs with mod(O_A,3)=mod(P_A,3)=2 possess the smallest gaps [shown in dark blue patterns in Fig. 3.4(a)].

3.4.2 AZ-GNWs

In contrast to the AA-GNW case, for GNWs with at least one zigzag edge, spin-dependent properties prove to be more intriguing. As presented in Fig. 3.3, unlike straight ZGNRs with two zigzag edges, (6_A,7_Z) has four zigzag edges in its one periodic unit

cell, giving rising to a variety of spin configurations. It not only exhibits paramagnetic (PM), ferromagnetic (FM), and anti-ferromagnetic (AFM) spin orderings, but also shows two new metastable states: longitudinal-anti-ferromagnetic (LAFM) and trans-anti-ferromagnetic (TAFM). For each state, the spin polarization is maximal on the zigzag edges, where it has a local ferromagnetic ordering. The AFM is the most energetically stable: compared to it, DFT (TBU) relative energy is 0.288 (0.852) eV for PM, 0.045 (0.046) eV for FM, 0.025 (0.027) eV for LAFM and 0.020 (0.027) eV for TAFM. Fig. 3.3 also shows that AFM has the largest DFT (TBU) band gap 0.46 (0.42) eV: compared to it, DFT (TBU) band gap is 0.02 (0. 02) eV for PM, 0.30 (0.27) eV for FM, 0.37 (0.34) eV for LAFM and 0.40 (0.36) eV for TAFM. Note that their band gaps open at either Γ or X point in the Brillouin zone, and bands around the Fermi level show a very small dispersion (< 0.1 eV), particularly for spin-polarized cases, because the spatial spin distribution is restricted to the portion of the nanowiggle with a zigzag edge (e.g., the zigzag portion behaves like a quantum dot). Since AFM is the most stable configuration, we performed the systematic band gap study based on this particular spin distribution. The AZ-GNW series considered here spans sector widths P_A and O_Z from 5 to 17 [Fig. 3.4(b)]. We observe three distinct behaviors corresponding to sector widths P_A such that mod(P_A,3)=0, 1, or 2. Moving horizontally across the chart, the band gap oscillates slightly for small O_Z values and gradually converges to a P_A-dependent constant corresponding to the isolated AGNR originated from the wedge-healed GNW.

3.4.3 ZA-GNWs

In Fig. 3.3, ZA GNW (4_Z,9_A) behaves most like a conventional ZGNR, which shows similar PM, FM and AFM states. Total energy calculations using DFT (TBU) show that the AFM state is more stable than both the PM and FM configurations, by 0.128 eV (0.438 eV) and 0.057 eV (0.131 eV), respectively. In contrast to the PM and FM configurations, the AFM spin distribution breaks the improper translational symmetry of the lattice, and the corresponding bands do not simply fold at the X point. The diffraction at the Bragg plane at X yields a fairly large Δ_{TBU}=0.23 eV (Δ_{DFT}=0.26 eV) band gap. Our systematic study of ZA GNWs focuses on the AFM spin arrangement [Fig. 3.4(c)] for P_Z and O_A sectors varying from 2 to 10 and 6 to 17, respectively. The general features of the

2D plot show a clear distinction between 3 families as we move along the plots vertical direction (i.e., P_Z as changes). These three families correspond to different values of O_A such that mod(O_A,3)=0, 1, or 2, for reasons similar to those given for the AZ systems.

3.4.4 ZZ-GNWs

ZZ GNWs constitute the fourth possibility of assembling achiral GNRs into GNWs. In Fig. 3.3, the PM state has a zero band gap. Interestingly, neither DFT nor TBU predict a stable FM state for the (7_Z,7_Z) system. This can be explained by the symmetry of the A and B graphene sublattices. The coexistence of spin-up along the entire length of the ZZ GNW edge would indeed require the local spin on sites belonging to both A and B sublattices on connected parallel and oblique sectors to be aligned, causing the FM configuration to be unstable. However, the A-B bipartition of the lattice does not preclude other spin configurations like a new longitudinal-ferrimagnetic (LFiM) state. Because of the quasi-AFM spin distribution (due to the A-B bipartition of the lattice), the total magnetization of LFiM is quite small ($M_{\mathrm{TBU}} = 0.07\mu_B, M_{\mathrm{DFT}} = 0.01\mu_B$). Hence, except for a small spin-up and spin-down splitting, the LFiM bands are very similar to the PM ones. Once again, DFT (TBU) predicts the AFM state to be more stable than the PM or LFiM states, by 0.055 eV (0.446 eV) and 0.056 eV (0.397 eV), respectively. The AFM state also has DFT (TBU) band gap as 0.25 (0.26) eV. The systematic study of the AFM state for a series of ZZ GNWs [Fig. 3.4(d)] indicates that the band gap changes smoothly as P_Z and O_Z cover the range of values from 4 to 17. The combined variations along the horizontal and vertical directions explain why the gap tends to get smaller along the chart's diagonal to eventually vanish as the 2D graphene character is recovered.

3.5 Quasiparticle corrections

So far, our DFT and TBU studies have shown that complex edge topologies of GNWs give rise to tunable band gaps and versatile magnetic states [25, 26]. However, the Kohn-Sham single-particle scheme of DFT is a ground state theory and hence (strictly speaking) it can only properly describe occupied bands [41]. Furthermore, Kohn-Sham DFT takes no account of many-body dynamical effects such as screening of added electrons or holes [42]. Consequently, while often qualitatively correct, its band structure

often fails to give reliable quantitative values for the band gaps of insulators and semiconductors, which are often underestimated by as much as 1.0 eV or more [41, 43].

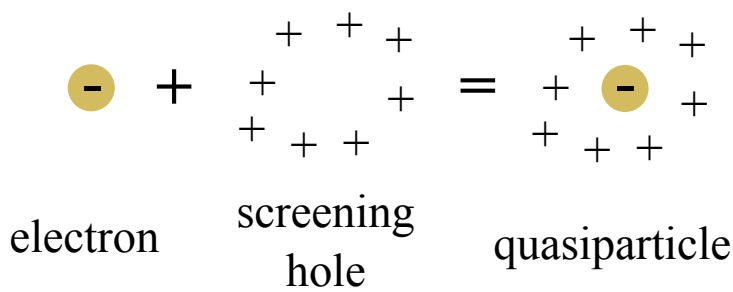

Figure 3.5: The repulsive Coulomb interaction creates a Coulomb hole (or cloud) around an electron to form a quasiparticle.

In a many-electron system, the electrons are correlated by the strong Coulomb interaction. The motion of one electron depends on the motion of all other electrons. For example, in a system composed of electrons in a background of positively-charged nuclei, electrons repel each other according to Coulomb's interaction. Consequently, an electron will repel other electrons creating a small region around itself in which there are fewer electrons. This region can be treated as a positively-charged screening hole (or cloud). The Coulomb hole behaves together with the electron like a single entity called quasiparticle, as shown in Fig. 3.5. The formation of the Coulomb hole around the electron enhances the attractive Coulomb potential felt by the electron, and thus more energy is required to excite the electron, leading to a larger band gap. The Kohn-Sham single-particle scheme fails to consider the Coulomb hole, and hence underestimates the band gap. By taking into account of the interaction between the electron and its surrounding Coulomb hole, the many-body perturbation approach within the *GW* approximation has proved to yield larger band gaps, closer to experimental data [43, 44].

Since the Coulomb hole reduces the total charge of the quasiparticle, the effective interaction between quasiparticles is screened and considerably weaker than the bare Coulomb interaction between electrons. In fact, the screened Coulomb interaction is sufficiently small so that the quasiparticles can be regarded as approximately independent [41]. In the many-body perturbation theory, for any state $|j>$, its quasiparticle (QP)

energy is given by

$$E_j^{\mathrm{QP}} = E_j^{\mathrm{KS}} + \langle \Psi_j | \Sigma(E_j^{\mathrm{QP}}) - V_{\mathrm{xc}} | \Psi_j \rangle \,, \tag{3.17}$$

where E_j^{KS} is the DFT Kohn-Sham (KS) eigenvalue of state $|j>$ and V_{xc} is the DFT exchange-correlation (xc) potential. Since the DFT xc potential is not sufficiently accurate, self-energy Σ is introduced as a correction term, which is the product of the noninteracting one-electron Green's function G and the screened Coulomb potential W under the GW approximation.

In this thesis, a first-principles many-body GW approach is used to provide more accurate description of GNWs' band gaps. Starting from DFT, QP energies are calculated within the self-consistent GW approximation as implemented in VASP. An iteration loop is run only for the calculation of G while W is fixed to the initial DFT obtained W_0 (called GW_0 in VASP). Since GW calculations are very computationally costly, depending on the size of a GNW, QP energies are iterated two or three times and the energy cutoff for response function is chosen between 80 to 120 eV, which is sufficient to yield QP shifts accurate to within 0.2 eV [27].

For AA (9_{A},6_{A}) in Fig. 3.6(a), its QP band gap is increased to 3.70 eV from the DFT one (1.58 eV), suggesting it as an insulator, in agreement with previous findings [45]. The significant self-energy correction can be attributed to the enhanced Coulomb interaction in such reduced dimensionality systems [44, 45]. For AZ (7_{A},4_{Z}) in Fig. 3.6(b), the AFM state has the largest DFT band gap 0.50 eV: compared to it, DFT band gap is 0.28 eV for PM, 0.18 eV for FM, 0.12 eV for LAFM, and 0.22 eV for TAFM. Self-energy corrections yield QP band gap 0.70 eV for PM, 0.61 eV for FM, 0.56 eV for LAFM, 1.14 eV for TAFM, and 1.46 eV for AFM. They are quite comparable to band gaps of conventional semiconductor elements such as Si (1.11 eV), Se (1.74 eV) and Ge (0.67 eV). More importantly, the existence of versatile magnetic configurations demonstrates the potential to utilize spin for band gap engineering in GNWs. Turning to ZA (3_{Z},8_{A}) [Fig. 3.6(c)], it shows PM (DFT band gap 0.00 eV), FM (DFT band gap 0.41 eV) and AFM (DFT band gap 0.53 eV) states. QP band gap remains zero for PM, while becomes 1.22 eV for FM and 1.52 eV for AFM. As for ZZ (7_{Z},6_{Z}) in Fig. 3.6(d), both DFT and QP band gaps of the PM and LFiM states are zero, while the most stable state AFM has a QP (DFT) band gap 0.93 eV (0.28 eV). Once again, self-energy corrections by GW demonstrate that ZA

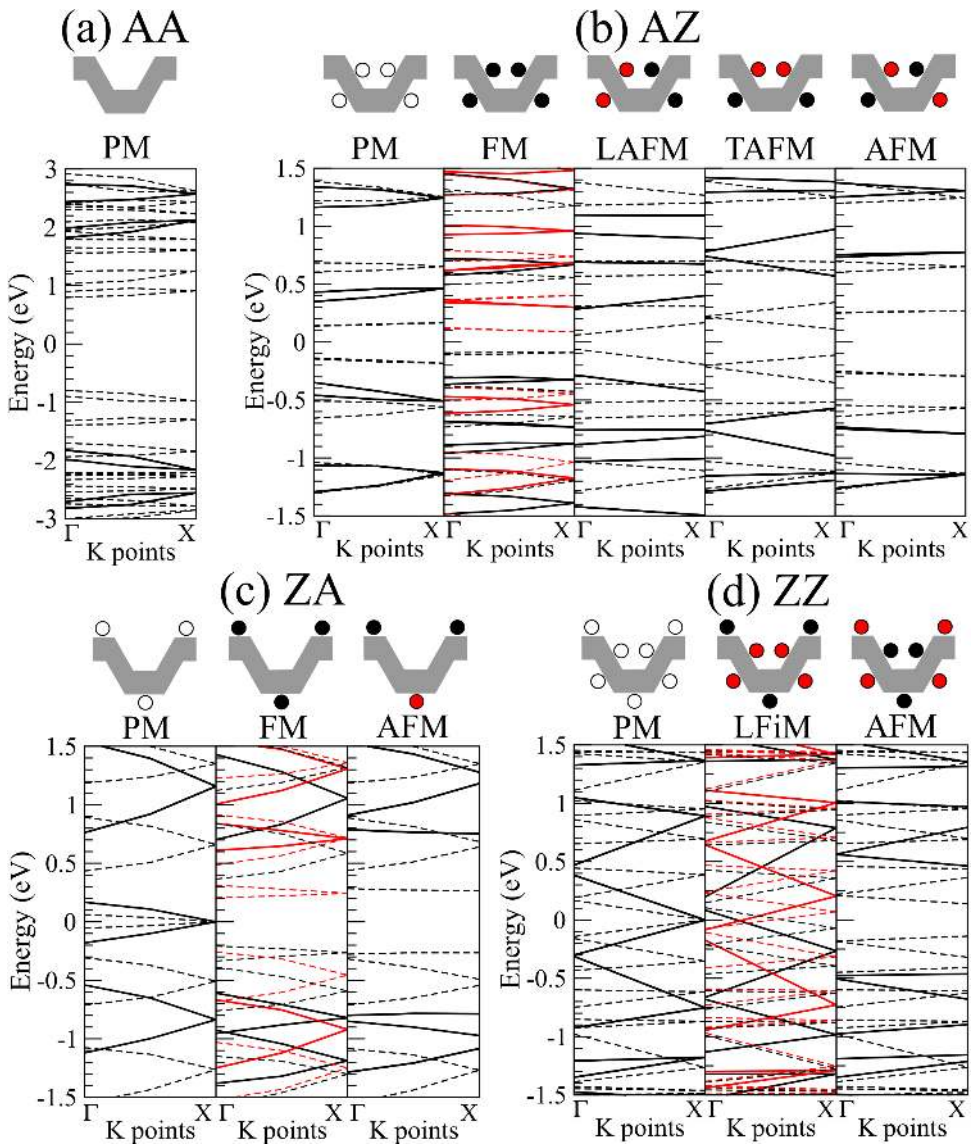

Figure 3.6: *GW* (solid lines) and DFT (dashed lines) electronic band structures of different magnetic states for the GNWs shown in Fig. 3.1. The schematic spin distributions (black: up, red: down) are shown on top of each panel. The Fermi level is set at 0 eV for each graph.

and ZZ GNWs can have band gaps comparable to Si. The *GW* and DFT band gaps of different magnetic states for all four GNWs are summarized in Table 3.1.

Clearly, the enhanced electron-electron interaction in the quasi-one-dimensional wiggle-edged systems results in significant self-energy corrections to their DFT band gaps. Consequently, the calculated QP band gaps are within the most interesting range 0.0-3.7 eV.

Table 3.1: The summary of *GW* and DFT band gaps of different magnetic states for the four GNWs.

magnetic states	GNW (9_A,6_A)	GNW (7_A,4_Z)	GNW (3_Z,8_A)	GNW (7_Z,6_Z)
	GW/DFT band gaps (eV)	*GW*/DFT band gaps (eV)	*GW*/DFT band gaps (eV)	*GW*/DFT band gaps (eV)
PM	3.70/1.58	0.70/0.28	0.00/0.00	0.00/0.00
FM		0.61/0.18	1.22/0.41	
LAFM		0.56/0.12		
TAFM		1.14/0.22		
AFM		1.46/0.50	1.52/0.53	0.93/0.28

3.6 Summary

In this chapter, we have predicted the emergence of physical phenomena in experimentally observed GNWs that are absent in their constitutive GNRs. The emergence of these properties is the result of the interplay between the properties of the GNR constituents, the symmetry of the atomic structure, and the bipartition of the graphene lattice. The relationship between the gap and the geometry is dictated by the armchair or zigzag characters of the corresponding parallel and oblique sectors, enabling GNWs to offer a broader set of geometrical parameters to tune the electronic structure compared to GNRs. All GNWs with at least one zigzag sector have an AFM ground state. More importantly, a number of new metastable spin distributions are found due to GNWs' unique wiggle-like edges. For instance, the existence of versatile magnetic states in the AZ GNW (7_A,4_Z) enables its QP band gap to be tuned from 0.56 to 1.46 eV, the ideal band gap range for semiconductor devices, thereby demonstrating GNWs' potential for nanoelectronic and spintronic applications. Finally, our systematic study establishes a road map for guiding the design and synthesis of specific GNWs for practical applications.

4. Thermal and thermoelectric properties of GNWs

In Chapter 3, we have shown that GNWs possess unusual electro-magnetic properties. In this chapter, we show that GNWs also possess superior thermoelectric properties compared to their straight GNR counterparts using a combination of density functional theory and semi-empirical approaches [46]. We also present a systematic study for a large set of nanowiggle structures to establish how geometry and spin influence the thermoelectric figure of merit ZT at room temperature. The highest ZT at room temperature is found to be 0.79. To further enhance ZT above 1 at room temperature, we devise a structural dislocation in the experimentally available GNW and find its ZT to exceed unity at room temperature [47].

4.1 Introduction

The thermoelectric effect is the direct conversion of temperature gradients into electric voltage and vice versa. This energy conversion mechanism can be used for power generation and refrigeration applications [48, 49]. Ideal thermoelectric materials are required to have good electrical conduction to allow facile transport of electrons across the structure. At the same time, to avoid the temperature gradient to be degraded by heat dissipation, good thermoelectric materials also need to be poor heat conductors. Quantitatively, the thermoelectric conversion efficiency is thus expressed by the dimensionless figure of merit $ZT = S^2 G_e T/k$, where S is the thermal power (or Seebeck coefficient), T is the average temperature, G_e is electrical conductance and $k = k_{\mathrm{el}} + k_{\mathrm{ph}}$ is the total thermal conductance, including contributions from electrons k_{el} and phonons k_{ph}. Much attention has been devoted to finding means to enhance ZT. For example, the Seebeck coefficient S can be improved by reducing the dimensionality of the system [50, 51]. ZT can also be boosted by degrading the thermal conductance due to phonons

---

Portions of this chapter previously appeared as: L. Liang, E. Cruz-Silva, E. C. Girão, and V. Meunier, Phys. Rev. B **86**, 115438 (2012).
Portions of this chapter previously appeared as: L. Liang and V. Meunier, Appl. Phys. Lett. **102**, 143101 (2013).

k_{ph} and the presence of sharp resonances in the electronic conductance G_e [52, 53].

Among new materials under intense scrutiny, graphene has attracted immense interest due to its outstanding thermal properties. However, its extremely high thermal conductivity (see Chapter 2) indicates that graphene is not intrinsically a good candidate for thermoelectric devices without tailored modifications. One such modification consists in reducing its dimensionality. To that respect, 1D GNRs stand out as better candidates for thermoelectric applications due to their semiconducting behaviors and reduced edge-dependent thermal conductivities [54]. Unfortunately, reported peak ZT values for pristine GNRs at room temperature remain inferior to 0.4 [55], a value shy of what other competing technologies can offer [49]. Here, we use DFT to investigate whether newly fabricated GNWs can be better candidates. We find that the presence of wiggle-like edges significantly reduces phonon thermal conductance without appreciably altering electrical transport, resulting in significant enhancement of ZT compared to GNRs. Then a semi-empirical approach is employed to perform a systematic study on geometrical and magnetic effects on thermoelectric properties.

4.2 Theoretical methods

Thermoelectric properties are obtained after the computation of the ballistic transport properties of electrons and phonons [52, 56]. The ballistic phonon thermal conductance k_{ph} is evaluated using the following Landauer-type formula [56, 57]

$$k_{\mathrm{ph}} = \frac{\hbar^2}{2\pi k_B T^2} \int_0^\infty d\omega \omega^2 T_{\mathrm{ph}}(\omega) \frac{e^{\hbar\omega/k_B T}}{(e^{\hbar\omega/k_B T} - 1)^2}, \tag{4.1}$$

where the phonon transmission function $T_{\mathrm{ph}}(\omega)$ is obtained using DFT calculations combined with the non-equilibrium Green's function formalism [52]. In the specific case of 1D systems, $T_{\mathrm{ph}}(\omega)$ is simply given by the number of phonon modes at frequency ω. It can be seen from Eq. (4.1) that, at low temperatures, low-frequency modes have dominating contributions to the thermal conductance.

Similarly, the electron transmission function $T_{\mathrm{el}}(E)$ leads to the computation of the

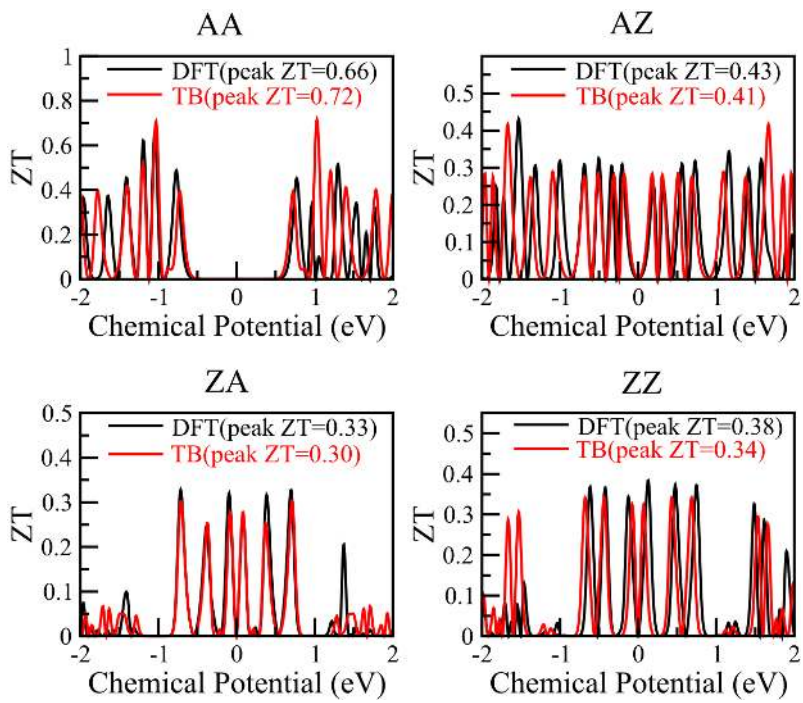

Figure 4.1: ZT versus chemical potential μ at T=300 K obtained both by DFT (black) and TB (red) for AA (9_A,6_A), AZ (7_A,4_Z), ZA (4_Z,9_A) and ZZ (6_Z,4_Z) GNWs. Except the AA GNW in the PM state, others are all in the AFM state.

following integral [58]:

$$K_n(\mu) = \frac{2}{h}\int_{-\infty}^{\infty} dE T_{\mathrm{el}}(E)(E-\mu)^n \left(-\frac{\partial f(E,\mu)}{\partial E}\right), \tag{4.2}$$

where $f(E,\mu) = 1/(1+e^{(E-\mu)/k_B T})$ is the Fermi-Dirac distribution function evaluated for chemical potential μ. Like the phonon transmission, $T_{\mathrm{el}}(E)$ is defined as the number of electronic bands crossing energy E for 1D systems. The integrals in the above equations are very sensitive to the electronic bands around the Fermi energy and provide all the quantities needed to evaluate ZT: $G_e = e^2 K_0(\mu)$, $S = K_1(\mu)/[eTK_0(\mu)]$ and $k_{\mathrm{el}} = \{K_2(\mu) - [K_1(\mu)]^2/K_0(\mu)\}/T$. Finally, the thermoelectric figure of merit ZT can be obtained by

$$ZT = \frac{S^2 G_e T}{k_{\mathrm{el}} + k_{\mathrm{ph}}}. \tag{4.3}$$

The formalism to compute ZT has been implemented using the electron and phonon transmission functions $T_{\mathrm{el}}(E)$ and $T_{\mathrm{ph}}(\omega)$, which are obtained by counting the number of bands at a given electronic energy or phonon frequency from the full electron and phonon

band structures of the system, respectively. For example, to obtain accurate full electron and phonon band structures for GNWs depicted in Fig. 3.1 in Chapter 3, DFT calculations are performed using the VASP package (more details in "Theoretical Methods" of Chapter 3). For phonon calculations, a supercell constructed from the optimized unit cell is used by VASP to generate the force constants matrix in the finite displacement scheme. Then PHONOPY code was utilized to obtain the phonon dispersion over the whole Brillouin zone [59]. However, DFT is too computationally demanding to perform a systematic study. Therefore, we use the TBU model developed in Chapter 3 to calculate electronic and magnetic properties of GNWs and GNRs systems, and a less expensive density-functional based tight binding method (DFTB+) [60] is used to build force constant matrices and compute phonon transmission functions. This combination of TBU and DFTB+ (referred as TB below) yields ZT in excellent agreement with DFT calculations, as exemplified by the case study shown in Fig. 4.1.

4.3 Thermal and thermoelectric properties

4.3.1 AA-GNWs

Fig. 4.2(a) shows DFT-calculated phonon dispersions and corresponding transmission functions of AA (9_A,6_A) and its straight counterpart AGNR-9 in their paramagnetic (PM) state. It can be readily seen that the nanoribbon exhibits more dispersive phonon branches than the nanowiggle, generally resulting in larger values of transmission function $T_{\mathrm{ph}}(\omega)$. The existence of a large number of flat phonon bands in (9_A,6_A) gives its $T_{\mathrm{ph}}(\omega)$ more frequencies that do not contribute to thermal transport compared to AGNR-9. Therefore, the thermal conductance of the nanowiggle is substantially lower than that of the nanoribbon, as clearly seen in Fig. 4.2(b). As a result, at room temperature, the straight AGNR-9 has a thermal conductance of 1.22 nW/K while the nanowiggle's one is decreased to 0.54 nW/K. Such spectacular suppression of phonon transmission and corresponding reduction of thermal conductance arise from the wiggle-like edges acting as scattering centers and the mismatch of phonon modes in the parallel and oblique sectors [53]. Conversely, the wiggle-like edges do not significantly disrupt electrical conduction [Figs. 4.2(c-d)]. Fig. 4.2(c) shows that a larger electronic band gap (1.48 eV) develops in the electrical conductance of the nanowiggle, compared to the band gap (0.58 eV) of

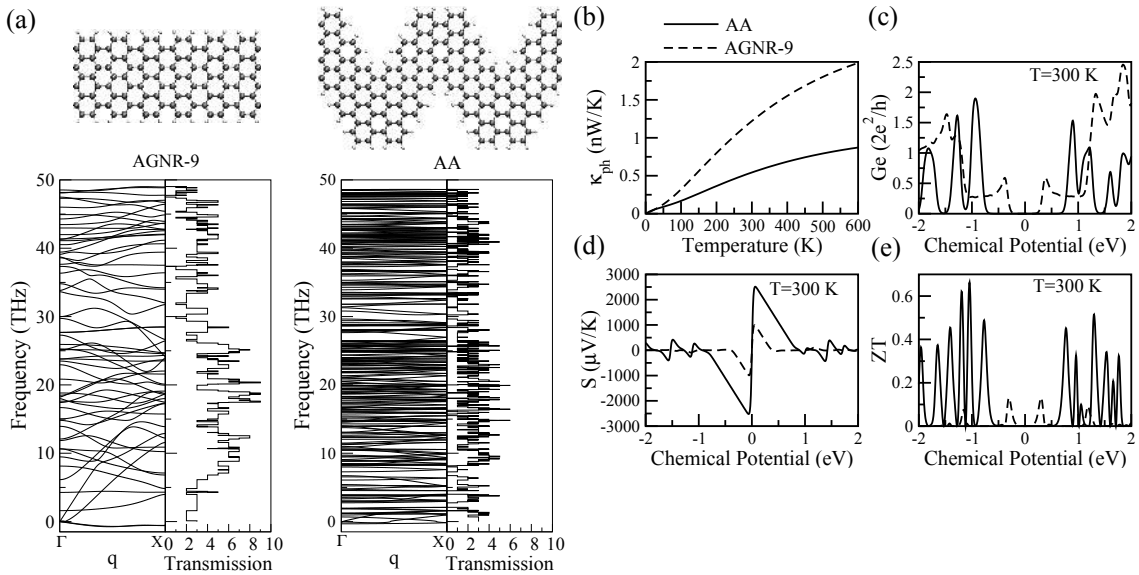

Figure 4.2: DFT Phonon dispersions and transmission functions of AGNR-9 and AA (9_A,6_A) with their structures on the top. AGNR-9 is the straight counterpart to (9_A,6_A) sharing the same width. (b) Thermal conductance k_{ph} versus temperature of (9_A,6_A) (solid line) and AGNR-9 (dashed line). (c) Electrical conductance G_e; (d) thermal power S; and (e) thermoelectric figure of merit ZT versus chemical potential μ at room temperature (T=300 K) of (9_A,6_A) (solid line) and AGNR-9 (dashed line). The zero in the chemical potential is chosen at the Fermi level. Both structures are in the PM state.

AGNR-9. Since a large electronic band gap can yield high thermopower values [53], (9_A,6_A) exhibits higher S than AGNR-9 [Fig. 4.2(d)]. This, combined with the preserved electrical conductance G_e and degraded phonon thermal conductance, gives (9_A,6_A) a high peak with ZT value 0.66 at μ=-1.08 eV [to be compared to 0.13 of the corresponding AGNR-9 in Fig. 4.2(e)], in excellent agreement with a previous study [55].

4.3.2 ZZ-GNWs

In contrast to AGNRs, ZGNRs in the PM configuration have a zero electronic band gap. The metallic behavior results in the mutual cancellation of electron and hole contributions to S, leading to very small values of S and subsequently almost zero ZT values for all widths [54, 61]. Our calculations show that ZGNR-6 [Fig. 4.3(a)] in the PM state has a peak ZT value of only 0.08 at room temperature (not shown). Clearly, opening a band gap is necessary to enhance ZT in ZGNRs. The AFM spin ordering opens a band gap of 0.40 eV for ZGNR-6 [Fig. 4.3(c)] and gives a corresponding ZT peak of 0.12 [shown as a dashed line in Fig. 4.3(e)]. To further increase ZT, thermal conductance needs to be

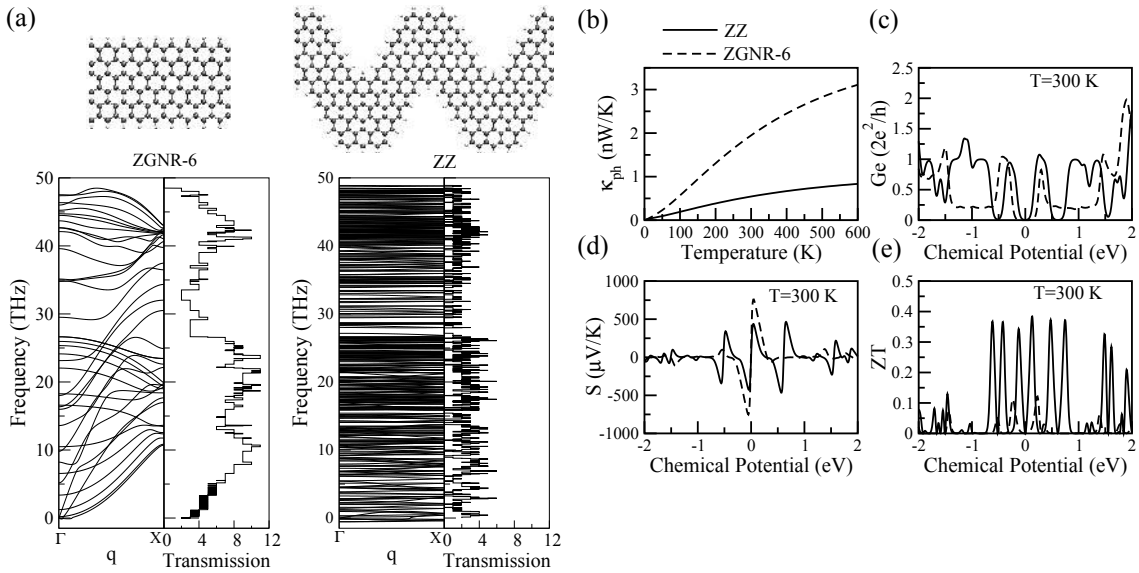

Figure 4.3: DFT Phonon dispersions and transmission functions of ZGNR-6 and ZZ (6_Z,4_Z) with their structures on the top. ZGNR-6 is the straight counterpart to (6_Z,4_Z) sharing the same width. (b) k_{ph} versus temperature of (6_Z,4_Z) (solid line) and ZGNR-6 (dashed line). (c) G_e; (d) S; and (e) ZT versus μ at room temperature of (6_Z,4_Z) (solid line) and ZGNR-6 (dashed line). The zero in the chemical potential is chosen at the Fermi level. Both structures are in their AFM state.

reduced. Similar to AA nanowiggles, the wiggle-like edges in ZZ systems also result in much less dispersive phonon branches compared to their straight GNR counterparts and thus generally smaller values of transmission functions [Fig. 4.3(a)]. Subsequently, k_{ph} of (6_Z,4_Z) is dramatically reduced, as shown in Fig. 4.3(b). At room temperature, (6_Z,4_Z) in the AFM spin ordering has a thermal conductance of 0.54 nW/K while ZGNR-6 shows k_{ph} as high as 1.95 nW/K. Similar reduction of k_{ph} is observed for the nanowiggle in the PM state as well (not shown). In addition, its particular edge structure opens up a band gap of 0.12 eV even in the PM state, indicative to a larger thermopower S. Indeed, at room temperature, the peak S of PM ZGNR-6 is only 97.06 μV/K but PM (6_Z,4_Z) has a S peak of 477.94 μV/K. The substantial reduction of k_{ph} with enhanced power factor S^2G_e enables the peak ZT of (6_Z,4_Z) in the PM configuration reaching 0.36 (not shown), more than four times that (0.08) of PM ZGNR-6. AFM spin ordering opens the band gap to 0.26 eV for (6_Z,4_Z) [Fig. 4.3(c)], resulting in the peak ZT of 0.38 at room temperature [solid line in Fig. 4.3(e)].

4.3.3 Electronic resonant tunneling

Turning to the two other types of nanowiggles AZ and ZA, DFT calculations also show flat phonon branches and reduced thermal conductance. It is important to note that many strategies, like the introduction of atomic vacancies and Stone-Wales defects, usually suppress both thermal and electrical conductance. Here, GNWs are able to have thermal conductance suppressed while essentially preserving electronic conduction, as shown in Figs. 4.2 (c-d) and Figs. 4.3 (c-d). This can be explained by electronic resonant tunneling. In a nanowiggle composed of alternate parallel and oblique sectors, the parallel sectors act as barriers between oblique sectors, and vice versa. In other words, GNWs can be seen as multi-barrier systems, where a resonant tunneling transport may occur and induce strong oscillations of the electrical conductance and thermopower [53, 62]. From Figs. 4.2(c) and 4.2(d), in comparison to AGNR-9, oscillations (multiple peaks) of the electrical conductance and thermopower of the nanowiggle (solid line) are clearly present, indicating the existence of resonant tunneling. Those peaks are directly responsible for multiple ZT peaks in Fig. 4.2(e). Similar oscillations of the electrical conductance and thermopower can be seen in Figs. 4.3(c) and 4.3(d) as well for (6_Z,4_Z), resulting in multiple peaks of ZT close to the Fermi level in Fig. 4.3(e). Such resonant tunneling effect not only preserves electrical conduction, but also leads to multiple ZT peaks so that good thermoelectric performance can occur at many chemical potential values. On the contrary, straight GNRs only show few significant ZT peaks close to Fermi level [see dashed line plots in both Figs. 4.2(e) and 4.3(e)].

4.4 Systematic study: establishing a roadmap to optimal ZT in GNWs

The charts shown in Fig. 4.4 describe how peak ZT values vary with respect to the widths of parallel (P) and oblique (O) sectors for AA nanowiggles in the PM state, and for AZ, ZA and ZZ nanowiggles in the AFM state, since only the PM spin ordering exists for AA GNWs and the AFM state is the most stable spin configuration for nanowiggles containing zigzag edges, as discussed in Chapter 3. Each color-coded square represents the highest ZT peak value for a specific GNW structure, with the chemical potential ranging from -2 eV to 2 eV at room temperature. Due to the dependence of ZT on both electric and thermal conductions, it exhibits complex relations to geometrical parameters P

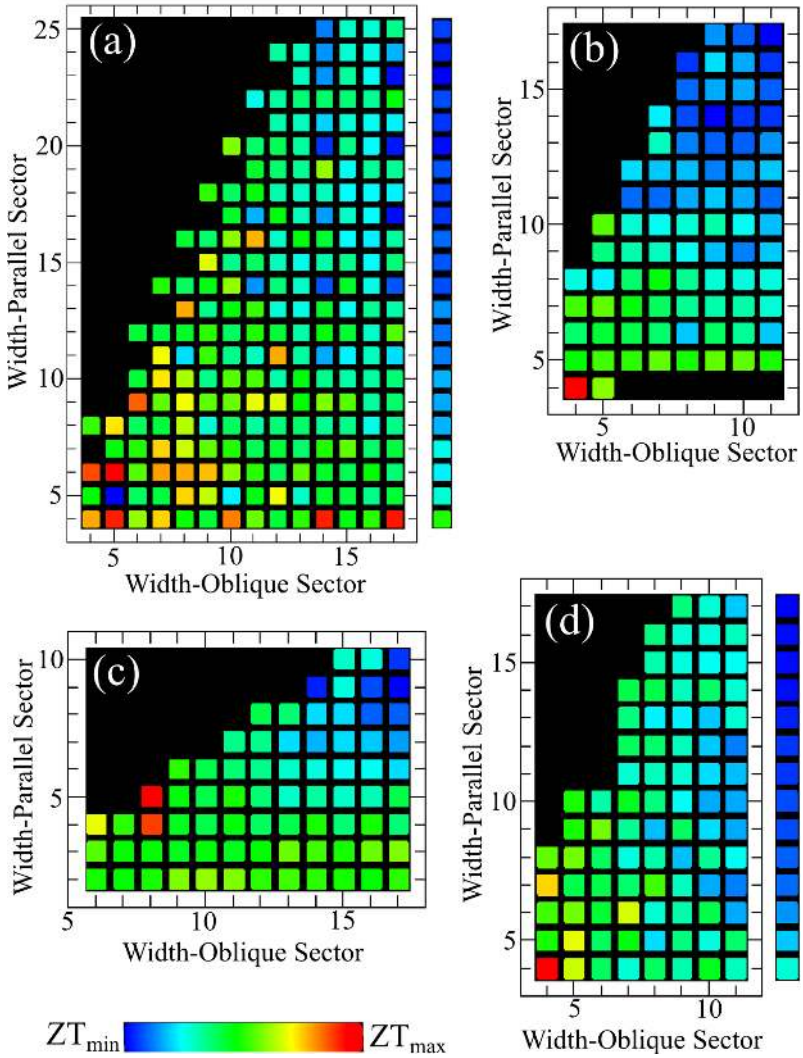

Figure 4.4: Peak ZT (room temperature) versus the widths of parallel (P) and oblique (O) sectors for (a) AA GNWs in the PM state, and for (b) AZ, (c) ZA and (d) ZZ GNWs in the AFM state. The points absent mainly on the upper-left corner of each graph correspond to geometries not allowed by the particular choice for P and O. In (a), the column on the right side of the frame represents peak ZT values of AA GNWs' straight counterparts in the PM state. Similarly in (d), the column next to the frame shows peak ZT of ZZ GNWs' straight counterparts in the AFM state. In these charts, minima and maxima of peak ZT values are (a) ZT_{min}=0.04, ZT_{max}=0.79; (b) ZT_{min}=0.12, ZT_{max}=0.65; (c) ZT_{min}=0.07, ZT_{max}=0.56; (d) ZT_{min}=0.04, ZT_{max}=0.57.

and O. In general, our calculations predict that k_{ph} gradually increases with the increase of P and O while electronic band gap decreases when the size of a structure gets larger. Therefore, small ZT values (shown in blue) are usually found in the upper-right portion of each graph where P and O are the largest, while ZT values exceeding a half of unity

(shown in red) appear mainly in the lower-left area of each graph. In addition to such general rule, for AA GNWs in Fig. 4.4(a), electronic band gaps can be classified according the multiple-of-three rules like straight AGNRs. The band gap Δ_N for AGNRs with $N = (3i + j)$ C-C lines follows the relation $\Delta_{3i+1} > \Delta_{3i} > \Delta_{3i+2}$, indicating that AA GNWs with mod(P_A,3)=mod(O_A,3)=2 possess the smallest band gaps. Generally, in these structures, small band gaps lead to small values of thermopower and therefore small ZT values [shown in blue marks in Fig. 4.4(a) evenly spaced in units of 3]. For many other systems, the existence of large band gaps (up to 1.7 eV) results in large thermopower values and ZT values usually higher than 0.5, indicating that AA GNWs are the best candidates as thermoelectrics among all four types of nanowiggle systems. Although straight AGNRs possess similarly large band gaps, the considerably higher thermal conductance renders their peak ZT values significantly smaller, as demonstrated in the column of data shown on the right side of the frame in Fig. 4.4(a). With the notable exception of very narrow AGNRs (P<8), the peak ZT value quickly decreases to the blue region as P increases. Similar results can be observed in Fig. 4.4(d) where peak ZT values of straight ZGNRs (shown as a column of data next to the frame) are much smaller than those of their nanowiggle counterparts.

4.5 Structural modifications to further enhance ZT

So far, we have shown that GNWs have better thermoelectric performance compared to GNRs. However, even so, the highest ZT at room temperature for pristine GNWs we studied is 0.79. For practical thermoelectric applications, it is often accepted that a system should have ZT higher than 1. Our DFT calculations show that a certain pattern of structural dislocation in the the experimentally available GNW (9_A,6_A) [Fig. 4.5(a)] can make ZT exceed 1 at room temperature [47]. The dislocation results in further thermal conductance reduction [Fig. 4.5(b)]. As a result, at room temperature, the dislocated GNW has a thermal conductance of 0.32 nW/K while the defect-free one's thermal conductance is 0.53 nW/K. As for electrical conduction, the dislocation also results in decrease of electrical conductance [Fig. 4.5(c)] and thermal power [Fig. 4.5(d)]. However, compared to the reduction in electrical conduction caused by the dislocation, the reduction of thermal conductance by the dislocation is more significant, leading to an overall

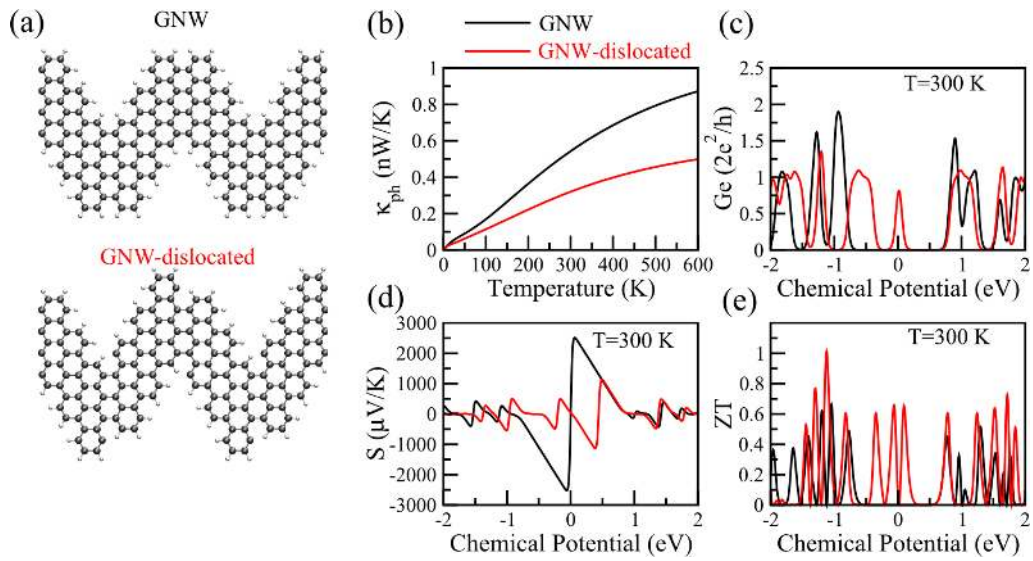

Figure 4.5: (a) Atomic structures of the defect-free GNW (9_A,6_A) (on the top) and its dislocated counterpart (on the bottom). They are periodic in the horizontal direction. (b) thermal conductance k_{ph} versus temperature of the GNW (black line) and dislocated counterpart (red line). (c) Electrical conductance G_e, (d) thermal power S, and (e) thermoelectric figure of merit ZT versus chemical potential μ at room temperature (T=300 K) of the GNW (black line) and dislocated counterpart (red line). The zero in the chemical potential is chosen at the Fermi level.

enhancement of ZT, as shown in Fig. 4.5(e). At room temperature, the peak ZT of the perfect GNW is 0.66 at μ=-1.08 eV while that of the dislocated counterpart is 1.01 at μ=-1.12 eV. At liquid nitrogen temperature (T=78K), the peak ZT of the dislocated GNW becomes 1.10 at μ=1.70 eV, which is also higher than 1.

4.6 Summary

In this chapter, GNWs are found to possess significantly enhanced thermoelectric performance compared to their straight GNRs counterparts. Such improvement originates from the combination of (i) reduced phonon thermal conductance due to phonon scattering by wiggle-like edges and the mismatch of phonon modes in the parallel and oblique sectors, and (ii) the electron resonant tunneling effect between these sectors which guarantee good electronic conduction. In general, peak ZT values of AA GNWs are more than triple those of straight AGNRs of the same width. For many GNWs with at least one zigzag sector, the interplay between parallel and oblique sectors opens a band gap, leading to larger thermopower and consequently to higher ZT while peak ZT values of straight

ZGNRs are almost zero due to their metallicity. Among all nanowiggle structures studied here, AA (6_A,5_A) has the maximum $ZT = 0.79$ at room temperature. A larger proportion of AA systems possess ZT higher than 0.5 in comparison to the other three types of achiral GNWs, leading to the conclusion that the experimentally available AA GNWs are the most promising candidates for thermoelectric applications. Additionally, our systematic study of the effects of geometry on ZT provides the guideline for the experimental design and synthesis of specific GNWs for thermoelectric applications. The highest ZT at room temperature for pristine GNWs we studied is 0.79. Finally, a structural dislocation in the experimentally available GNW (9_A,6_A) is found to further enhance ZT over 1 at room temperature.

5. Substrate effects on electronic and magnetic properties of GNRs and GNWs

In Chapters 3 and 4, we have discussed the electronic, magnetic and thermal properties of free-standing GNWs. In reality, however, they are synthesized on a gold substrate. Hence, in this chapter, the influence of the gold substrate on electronic properties of both GNRs and GNWs is investigated [63]. Furthermore, a particular armchair-zigzag GNW is chosen to study the substrate influence on its magnetic properties [27].

5.1 Introduction

While many of the predicted potential uses of graphene rely on its intrinsic properties, a substrate is usually required to support such an atomically thin material for practical applications [64]. In particular, metallic substrates are often used as catalysts in graphene formation, as probes during electrical measurements, or as source and drain electrodes in electronic devices [65]. It follows that one of the most important challenges for the use of graphene-based electronic devices is to develop a precise understanding of the interaction between graphene and its supporting metallic substrate.

As mentioned in Chapter 2, an atomically precise bottom-up approach has been developed [21] to grow subnanometer wide straight and wiggle-like armchair GNRs with clean edges on a gold substrate. The high quality of these samples allows their electronic properties to be measured with high fidelity on a stepped Au(788) surface. The corresponding band gaps are found to be smaller than theoretically predicted quasiparticle band gaps of their free-standing counterparts [66]. Evidently, these results indicate the gold substrate has a deep influence on their electronic properties and a satisfactory understanding of those effects calls for methods beyond density functional theory.

Portions of this chapter previously appeared as: L. Liang and V. Meunier, Phys. Rev. B **86**, 195404 (2012).
Portions of this chapter previously appeared as: L. Liang, E. C. Girão, and V. Meunier, Phys. Rev. B **88**, 035420 (2013).

Here, we first carry out DFT calculations to study electronic properties of experimentally synthesized AGNR-7 and AA GNW (9_A,6_A) on the gold substrate. DFT fails to capture the experimentally observed band gap reductions due to the substrate, and hence we combine the many-body *GW* approach (as discussed in Chapter 3) and a semi-empirical image charge model to describe the band gap reductions.

5.2 Theoretical methods

Previous DFT calculations showed that the bonding of graphene to a Au(111) surface is weak [65, 67] and also predicted weak physisorption for GNRs deposited on an Au/InAs(110) surface [68]. Local density approximation (LDA) is well known to overestimate the binding in such weakly bonded systems where van der Waals (vdW) interactions dominate, and is not suitable for inhomogeneous GNRs-metal interfaces in principle. A generalized gradient approximation (GGA) for inhomogeneous systems, however, does not necessarily improve the results due to its tendency to underestimate the binding. In practice, in the case of graphene on gold, no binding is predicted at all within GGA [65]. A solution is to complement GGA with the semi-empirical approach based on Grimme formula [69] to capture the vdW interaction.

DFT calculations are performed using the VASP package (more details in "Theoretical Methods" of Chapter 3). The vdW interaction is included within a DFT-D2 approach of Grimme [69], as implemented in VASP. We have used a value of 40.62 J nm^6/mol for the Au dispersion coefficient C_6 and of 1.772 Å for the Au vdW radius R_0 [65]. The simulated scanning tunneling microscopy (STM) images shown here are computed using converged electronic densities within the Tersoff-Hamann approximation [70].

The Au(111) surface is modeled by a periodic slab geometry constructed from the GGA-optimized Au bulk and each supercell contains seven gold layers with a GNR or GNW adsorbed over the top layer. A vacuum spacing of 16 Å is used to avoid spurious interactions with replicas. We adapt the graphene in-plane lattice constant according to the GGA-optimized gold lattice constants. It follows that the C-C bond length is slightly stretched to 1.45 Å compared to its experimental value 1.42 Å, corresponding to a small lattice mismatch of 2.1%. As shown in Fig. 5.1, due to symmetry, the most stable in-plane adsorption geometries of AGNR-7 and AA GNW (9_A,6_A) on the substrate correspond to

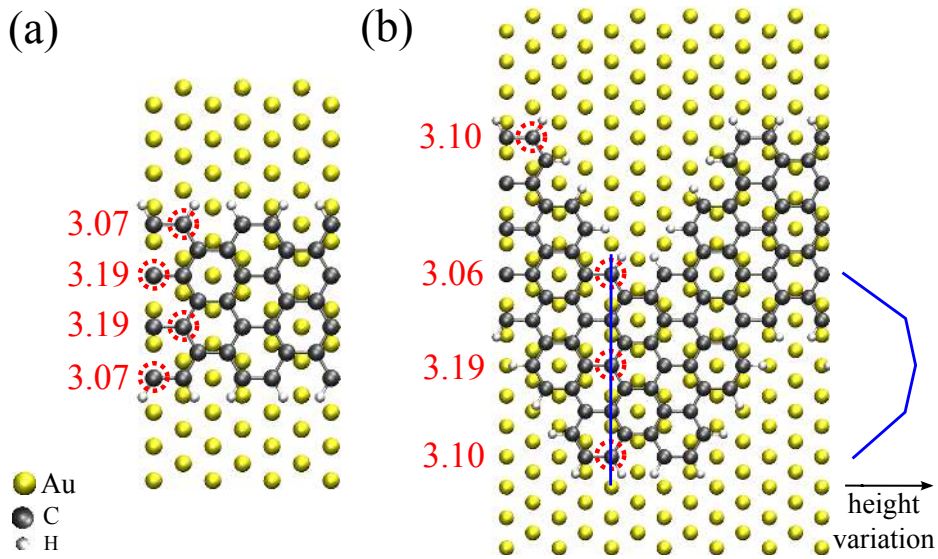

Figure 5.1: The adsorption geometry of a hydrogenated (a) AGNR-7 and (b) AA (9_A,6_A) on the Au(111) surface. One unit cell is shown for both cases. Numbers indicate separation distances in Å between circled C atoms and Au atoms right below them. To visualize the bulking of the GNW upon adsorption on the substrate, a height variation (blue curve) of the GNW along the blue line is shown on the right side.

a carbon atom either on top of a gold atom (e.g., carbon atoms highlighted by red dashed circles) or on top of the center of the bridge between two gold atoms [67].

5.3 Substrate effects on electronic properties

5.3.1 Geometry on the substrate

In Fig. 5.1(a), AGNR-7 is shown to exhibit a surface buckling of ∼0.12 Å. Edge C atoms move downwards more compared to basal C atoms. The average vertical separation distance between the straight GNR and Au(111) surface is in the range 3.07-3.19 Å, indicating only weak physisorption at the interface, as predicted previously [65, 67, 68]. Similar structural corrugation of ∼0.13 Å has been observed for (9_A,6_A) [Fig. 5.1(b)]. The equilibrium separation distance between edge C atoms (red dashed circles) of the nanowiggle and gold substrate is ∼3.06 Å, while the distance between atoms in the central nanowiggle and the substrate is ∼3.19 Å. (9_A,6_A) also has a separation distance to the substrate larger than 3.0 Å and hence is only physisorbed on the substrate.

We used the relaxed geometries to simulate constant current STM images, corresponding to the occupied states within 1 eV of the Fermi level. The images show both

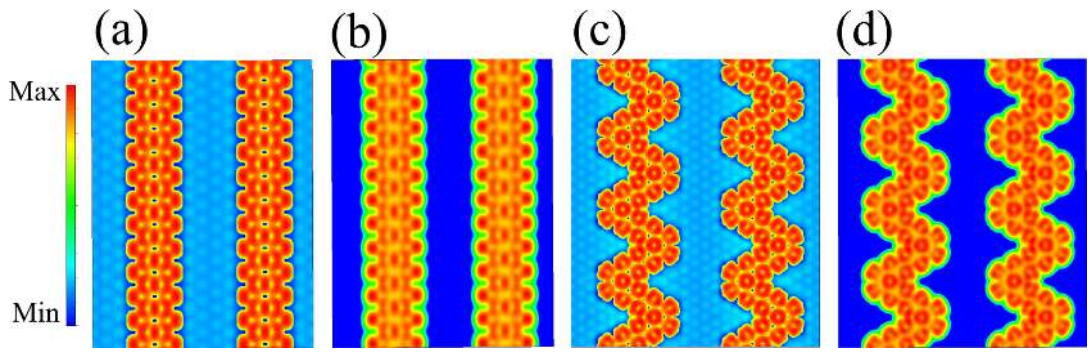

Figure 5.2: Simulated constant current STM images of AGNR-7 on the gold surface at -1 eV bias voltage with tip height range given by (a) H_{min} = 2.18 Å, H_{max} = 5.18 Å and (b) H_{min} = 4.42 Å, H_{max} = 6.40 Å. H_{min} and H_{max} represent the minimum and maximum tip-substrate distance, respectively. Simulated constant current STM images of (9_A,6_A) on the Au(111) surface at -1 eV bias voltage with (c) H_{min} = 2.20 Å, H_{max} = 5.23 Å and (d) H_{min} = 4.38 Å, H_{max} = 6.43 Å.

the GNR and GNW (mostly in red) with only a weak visible registry of the gold surface atoms (rendered in lightly blue circles), in Figs. 5.2(a) and 5.2(c). However, when a smaller constant current is chosen (equivalent to raising the STM tip away from the substrate at constant bias) in Figs. 5.2(b) and 5.2(d), the substrate can no longer be detected while atomic details of the the GNR and GNW are revealed, showing that electronic states close to the Fermi level are mostly concentrated at the edge. In other words, edge states can be detected at low bias, consistent with experimental STM observations [21, 66]. Furthermore, careful examination on Fig. 5.2(d) reveals that edge atoms at the bottom of V-shape valleys exhibit larger contrast than other edge atoms, in agreement with recent findings on the distribution of the local current flowing along the system [71].

5.3.2 Band structures on the substrate

Figs. 5.3(a) and 5.3(c) are DFT band structures of AGNR-7 supported on the Au(111) surface and its free-standing counterpart (dashed lines), respectively. Clearly, the GNR-Au(111) system is metallic. However, compared to bands of the isolated GNR, the GNR-projected bands [highlighted by red dots in Fig. 5.3(b)] still exhibit the main features of the isolated GNR. They are slightly perturbed due to the weak interaction between the AGNR-7 and substrate. Also, in comparison to the DFT band gap (1.47 eV) of the isolated AGNR-7, the DFT band gap (1.45 eV) of the adsorbed AGNR-7 is only slightly reduced. Similarly, as shown in Fig. 5.3(e), projection bands (in red dots) of the AA

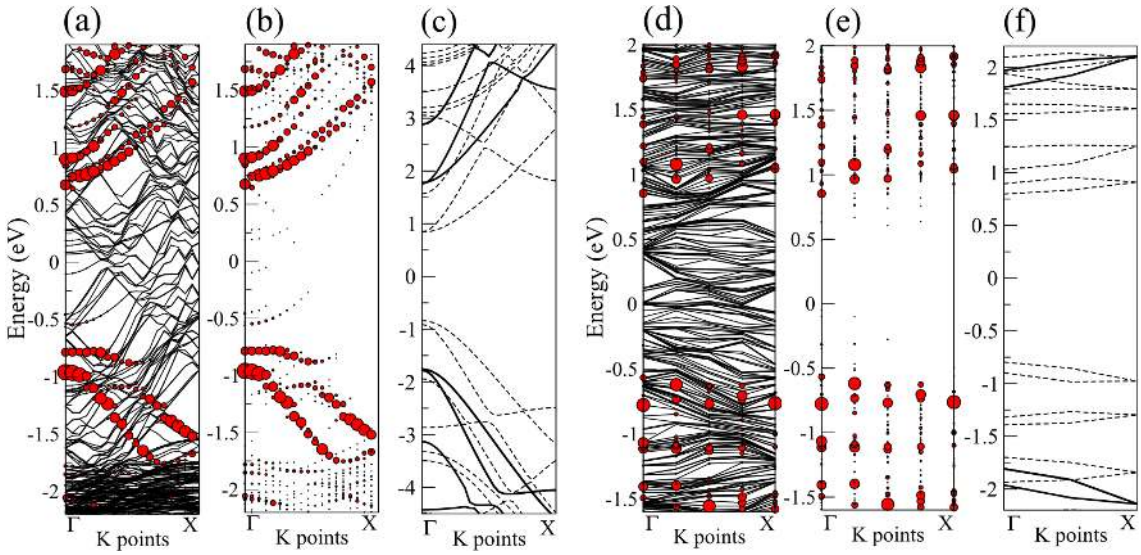

Figure 5.3: (a) Electronic band structures of AGNR-7 deposited on a Au(111) substrate. The dots superimposed on the bands correspond to projected bands due to AGNR-7. Panel (b) only shows the dots, for clarity. (d) Electronic band structures of (9_A,6_A) deposited on a Au(111) substrate. The dots show the projected bands of (9_A,6_A). Panel (e) only shows the projected bands of (9_A,6_A) for clarity. The size of the dot is proportional to the amplitude of the projection. (c) and (f) show electronic band structures of free-standing AGNR-7 and (9_A,6_A), respectively. Solid (dashed) lines represent bands at the *GW* (DFT) level. The Fermi level is set at 0 eV in each graph.

(9_A,6_A) adsorbed on the gold surface are weakly perturbed by the substrate, compared to bands of its isolated counterpart [Fig. 5.3(f) in dashed lines]. The DFT band gap (1.43 eV) of the adsorbed (9_A,6_A) is also reduced by 0.07 eV compared to the DFT band gap (1.50 eV) of the isolated counterpart.

5.3.3 Charge transfer and substrate polarization

Due to the vdW interaction between the adsorbates and gold substrate, previous works have shown that a small charge transfer often occurs at the interface, leading to the doping of the adsorbates [65, 67, 68]. To determine whether the adsorbed GNR and GNW are *n*- or *p*-typed doped, work functions of the isolated GNR (GNW) and the clean Au(111) surface are calculated. The work function of the surface is 5.21 eV, higher than the work functions of both the GNR and GNW, which are 4.71 eV and 4.80 eV, respectively. Thus, provided electronic band structures of isolated systems remain essentially unchanged upon formation of the interface, we can infer an electronic charge transfer from

the adsorbed GNR (GNW) to the surface and hence a p-type doping of the adsorbed GNR (GNW), consistent with previous results [67, 68]. Of course, band structures of both the adsorbates and substrate are weakly perturbed, but p- type doping of the adsorbates should still take place. To verify this hypothesis, we computed plane-averaged electronic densities $\rho(z)$ to visualize the electronic redistribution $\Delta\rho(z) = \rho_{\mathrm{M|G}}(z) - \rho_{\mathrm{M}}(z) - \rho_{\mathrm{G}}(z)$ upon formation of the interface, where $\rho_{\mathrm{M|G}}(z)$, $\rho_{\mathrm{M}}(z)$ and $\rho_{\mathrm{G}}(z)$ represent plane-averaged electronic densities of the GNR (GNW)-Au(111) system, isolated Au(111) surface and isolated GNR (GNW), respectively. As shown in Fig. 5.4(a), both electronic redistributions $\Delta\rho(z)$ are localized at the interface. For both AGNR-7 and (9_{A},6_{A}), it can be found that $\Delta\rho(z) < 0$ within around 1 Å below the adsorbate, while there is an increase in $\Delta\rho(z) > 0$ within $\sim$1.4 Å above the Au surface, clearly demonstrating electronic charge transfers from the adsorbate to the substrate. Such electronic charge redistributions at the interface lead to electronic dipole moments and thus substrate polarization.

5.3.4 Band gap reduction by substrate polarization: an image charge approach

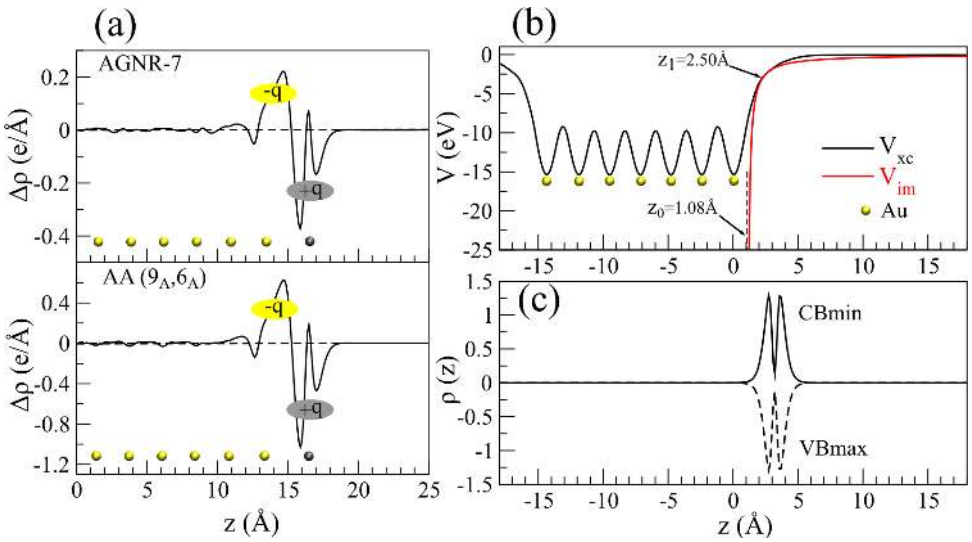

Figure 5.4: (a) Plane-averaged difference electronic charge densities $\Delta\rho(z) = \rho_{\mathrm{M|G}}(z) - \rho_{\mathrm{M}}(z) - \rho_{\mathrm{G}}(z)$ upon formation of the interface for AGNR-7 and AA (9_{A},6_{A}), respectively. (b) Plane-averaged exchange-correlation potential of a clean gold surface and image potential. The origin is set at the first gold layer, and z_0 and z_1 are fitted by setting the intersection of the two curves at z_1. (c) Plane-averaged charge densities for the conduction band minimum ($\mathrm{CB_{min}}$) and the valence band maximum ($\mathrm{VB_{max}}$) of the free-standing (9_{A},6_{A}).

As mentioned in Section 3.5 in Chapter 3, an electron will repel other electrons creating a small region around itself in which there are fewer electrons. This region can be treated as a positively-charged screening hole, which increases the attractive Coulomb potential felt by the electron inside the hole and subsequently increases the band gap. However, the substrate polarization is expected to screen the Coulomb potential experienced by the electron and in turn effectively reduce the band gap of the adsorbate compared to that of its isolated counterpart [42, 64, 72, 73]. Such long-range many-body polarization effect, however, cannot be easily modeled by conventional DFT using local or semi-local approximations as implemented in LDA or GGA since these xc potentials fail to reproduce the asymptotic image potential tail shape of a metal surface [72, 74]. In principle, this effect can be captured by more accurate *GW* calculations. However, it is very computationally demanding and complicated to perform *GW* calculations on a large metallic system. The slab model to simulate a metal surface usually requires many metal atoms, which significantly increases the computational cost of *GW* calculations. An even bigger challenge is that *GW* requires the computation of dielectric constants while they are infinity for perfect metals, and thus *GW* calculations are currently unavailable for metallic systems in most DFT softwares. Therefore in this thesis, instead of using *GW* on the gold surface, we adopt a semi-empirical image charge model as a computationally much less demanding alternative to estimate the band gap reduction.

In such a model [64, 73], the quasiparticle (QP) energy of a substrate-supported layer is given by $E^{\mathrm{QP}}_{j;\mathrm{supported}} = E^{\mathrm{QP}}_{j;\mathrm{free}} + \Delta P_j$, where $E^{\mathrm{QP}}_{j;\mathrm{free}}$ is the QP *GW* energy of state $|j>$ of the free-standing layer (GNR or GNW here), and ΔP_j is the correction term to account for substrate polarization. Although conventional DFT accurately models the short-range surface potential, it fails to depict the potential far from the surface. In the long-range limit, effective potential due to the surface is better described by an image potential, V_{im} [74]. Hence, ΔP_j can be approximated as

$$\Delta P_j = \int_{z>z_1} dr[V_{\mathrm{im}}(z) - V_{\mathrm{xc}}^{\mathrm{Au(111)}}(r)]\rho_j(r), \tag{5.1}$$

where $V_{\mathrm{im}}(z) = -e^2/4|z-z_0|$ is the image potential and $V_{\mathrm{xc}}^{\mathrm{Au(111)}}(r)$ is the xc potential of a clean Au(111) surface; $\rho_j(r)$ is the charge density of state $|j>$ of the free-standing

layer. z_0 is the image plane position and z_1 is where the transition from short-range to long-range limit takes place and $V_{\mathrm{im}}(z)$ starts to deviate from $V_{\mathrm{xc}}^{\mathrm{Au(111)}}(r)$ [74] .

To calculate ΔP_j, simulations are performed separately for the two subsystems, using atomic positions determined in the optimized GNR(GNW)-Au(111) system. The clean gold surface is first treated to obtain the xc potential $V_{\mathrm{xc}}^{\mathrm{Au(111)}}(r)$; the free-standing AGNR-7 or (9_{A},6_{A}) is used to obtain the DFT charge densities at the conduction band minimum ($\mathrm{CB_{min}}$) and the valence band maximum ($\mathrm{VB_{max}}$). Finally, the QP band gap of a substrate-supported GNR (GNW) can be obtained using $E^{\mathrm{QP}}_{\mathrm{gap;supported}}$=$E^{\mathrm{QP}}_{\mathrm{gap;free}}$+$\Delta P_{\mathrm{CB_{min}}}$-$\Delta P_{\mathrm{VB_{max}}}$, where $\Delta P_{\mathrm{CB_{min}}}$ and $\Delta P_{\mathrm{VB_{max}}}$ are corrections to the $\mathrm{CB_{min}}$ and $\mathrm{VB_{max}}$, respectively.

Table 5.1: DFT and *GW* band gaps of free-standing and substrate-supported AGNR-7 and GNW (9_{A},6_{A}). For the substrate-supported case, the *GW* band gaps are estimated in combination of *GW* and the image charge model. The experimental band gaps [66] of substrate-supported AGNR-7 and (9_{A},6_{A}) are also shown for comparison.

	free-standing AGNR-7	substrate-supported AGNR-7	free-standing GNW (9_{A},6_{A})	substrate-supported GNW (9_{A},6_{A})
DFT band gap (eV)	1.47	1.45	1.50	1.43
GW band gap (eV)	3.53	2.85	3.62	2.96
experimental band gap (eV)		2.8 ± 0.4		3.1 ± 0.4

As shown in Figs. 5.3(c) and 5.3(f) (solid lines), the *GW* band gaps of the free-standing AGNR-7 and (9_{A},6_{A}) are 3.53 eV and 3.62 eV respectively, much larger than their DFT band gaps (1.47 eV and 1.50 eV) [Table 5.1]. Previous works [44, 45] show *GW* band gaps of AGNR-7 and (9_{A},6_{A}) are 3.80 and 3.71 eV respectively, slightly larger than ours. This can be explained by the fact that the GNR (GNW) is deposited on the gold substrate and stretched slightly to ensure lattice match between them. This stretch tends to decrease band gaps slightly [75]. From Fig. 5.4(b), by computing the intersection of the xc potential and image potential, we find z_0 and z_1 as 1.08 Å and 2.50 Å respectively. These values agree with the results by Li *et al.* [73]. In Fig. 5.4(c), charge densities of (9_{A},6_{A}) reach zero rapidly as they approach the surface, indicating weak coupling at the interface. The image charge model can be used only in the weak-coupling limit, which holds for our

case here. Hence, $\Delta P_{\mathrm{CB_{min}}}$-$\Delta P_{\mathrm{VB_{max}}}$ is calculated as -0.66 eV and therefore the QP band gap of the adsorbed (9_A,6_A) is reduced to 2.96 eV [see Table 5.1], in agreement with the experimental value (3.1 $\pm$ 0.4 eV) [66]. Similarly, as shown in Table 5.1, the band gap reduction of the straight AGNR-7 by the substrate is estimated as 0.68 eV and thus its QP band gap is 2.85 eV, well consistent with the experimental one (2.8 $\pm$ 0.4 eV) [66]. As discussed above, conventional DFT calculations yield only a DFT band gap reduction of 0.02 eV for the adsorbed AGNR-7 and 0.07 eV for the adsorbed (9_A,6_A), as shown in Table 5.1. Clearly, DFT fails to quantitatively capture band gap reductions by substrate polarization while the semi-empirical image charge model offers a very satisfactory and computationally less demanding (compared to a full *GW* method) tool to estimate such band gap reductions.

5.4 Substrate effects on magnetic properties

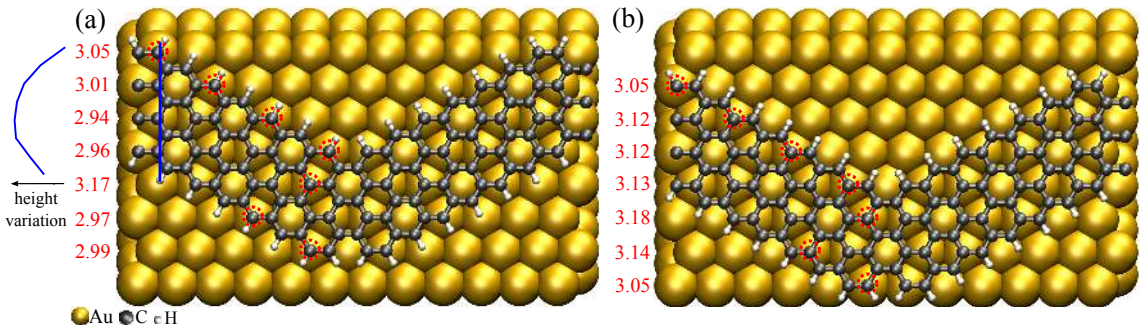

Figure 5.5: Top view of two most stable adsorption geometries of the GNW (7_A,4_Z) in the AFM state on the Au(111) surface. The system is periodic in both horizontal and vertical directions and one unit cell is shown. To ensure the strongest binding with the substrate, a carbon atom should be either on top of a gold atom or on top of the center of the bridge between two gold atoms. Numbers in red indicate separation distances in Å between circled C atoms and Au atoms right below them. To visualize the bulking of the GNW upon adsorption on the substrate, a height variation (blue curve) of the GNW along the blue line is shown on the left side.

In Chapter 3, we have predicted that versatile spin orderings are present in GNWs. However, those findings are based on free-standing GNWs and the experimentally fabricated GNWs are supported on a gold substrate. In this chapter, we have already demonstrated that the gold substrate can have significant influence on electronic properties of GNWs. Therefore, it is essential to find out how the substrate affects their magnetic prop-

erties. As a case study, we chose the AZ GNW (7_A,4_Z) in Fig. 3.1(c), one thoroughly studied in Chapter 3, to investigate the influence of the Au(111) surface on its spin properties.

Due to symmetry, a stable in-plane adsorption geometry of (7_A,4_Z) on the gold substrate corresponds to a carbon atom either on top of a gold atom (e.g., carbon atoms highlighted by red dashed circles in Fig. 5.5) or on top of the center of the bridge between two gold atoms [63, 67]. Both geometries shown in Fig. 5.5 satisfy such requirement. Our DFT calculations indicate that the left geometry is more stable than the right one by 0.484 eV because half of zigzag edge C atoms in the left panel stay right on top of gold atoms while none of zigzag edge C atoms in the right panel do. Hence, zigzag edge C atoms have stronger binding with the Au(111) surface in Fig. 5.5(a), subsequently leading to slightly shorter separation distances (see red numbers in Fig. 5.5) and more stable adsorption geometry. In Fig. 5.5(a), edge C atoms of (7_A,4_Z) move downwards more compared to basal C atoms, resulting in a surface buckling of $\sim$0.19 Å, similar to the structural corrugation observed for (9_A,6_A) on the Au(111) surface [Fig. 5.1(b)]. More importantly, the vertical separation distance between the (7_A,4_Z) GNW and Au(111) surface ranges from 2.94 Å to 3.17 Å, indicating relatively weak physisorption at the interface. Similar conclusions can be reached for the configuration shown in Fig. 5.5(b). Spin-polarized DFT calculations show that the magnetic configuration does not significantly vary in the presence of the gold substrate while its strength is only mildly weakened. For example, in the AFM (TAFM) state, the maximum atomic magnetic moment is 0.127 (0.119) μ_B for unsupported (7_A,4_Z) and decreases to 0.108 (0.095) μ_B when it is gold-supported for both geometries in Fig. 5.5. This can be understood by the fact that the gold substrate only interacts with the GNW by weak physical forces. Additionally, for conventional ZGNR-6 adsorbed on the Au(111) surface, its AFM state also remains with the maximum atomic magnetic moment reducing to 0.133 μ_B compared to 0.145 μ_B of the free-standing one, consistent with recent experimental observations [76]. Therefore, it seems that the versatile magnetic states of GNWs are indeed present even when they are on the Au(111) substrate.

Note that the magnetic robustness of GNWs on the gold substrate is assessed by spin-polarized DFT calculations, which cannot fully capture many-body polarization ef-

fects by the substrate [63, 64]. Such many-body effects are found to reduce the band gap of the adsorbate and may influence its magnetic properties as well. Due to the extreme difficulty to perform spin-polarized *GW* calculations for GNWs on the metallic substrate, the study on the many-body effects on magnetism of GNWs is beyond the scope of this thesis.

5.5 Summary

In this chapter, we have used first-principles theory to show that both the GNR and GNW are weakly adsorbed on the Au(111) surface by the vdW force. Particularly, carbon atoms located at the edge tend to bend more towards to the substrate than basal carbon atoms. Despite being at lower vertical positions, simulated STM images show larger corrugation at edge atoms. The small net charge transfer detected from the GNR (GNW) to the substrate results in a *p*-type doping of the GNR (GNW). Such charge transfer gives rise to an electric dipole at the interface, leading to substrate polarization. A semi-empirical image charge model has been developed to assess polarization-induced band gap reductions. The band gap reductions of AGNR-7 and (9_A,6_A) by the gold substrate are estimated as 0.68 eV and 0.66 eV, respectively. Consequently, the quasiparticle band gaps of the adsorbed AGNR-7 and (9_A,6_A) are 2.85 eV and 2.96 eV respectively, which agree well with experimentally measured values. This indicates that the image charge model provides a satisfactory and computationally tractable method (compared to full *GW* calculations) to predict band gap reductions for both AGNR-7 and (9_A,6_A) supported on the Au(111) surface. Furthermore, metal substrates like gold affect significantly electronic properties of atomically thin materials such as GNRs and GNWs, and accurate theoretical calculations of these materials should always take in account substrate effects. Finally, our spin-polarized DFT calculations indicate that the Au(111) substrate on which GNWs are synthesized does not considerably alter their magnetic properties.

6. Heterojunctions of pure and nitrogen-doped GNWs

So far, we have studied pure GNWs. Recently, nitrogen atoms have been doped to GNWs and heterojunctions consisting of pure and nitrogen-doped GNWs have been synthesized [Cai *et al.*, Submitted] [24]. In this chapter, the electronic and transport properties of GNW heterojunctions are studied. Furthermore, as shown below, nitrogen doping results in type-II band alignments at the interface, demonstrating the potential of heterojunctions for excitonic solar cell applications. In this chapter, we also estimate the maximum solar power conversion efficiency of heterojunctions.

6.1 Introduction

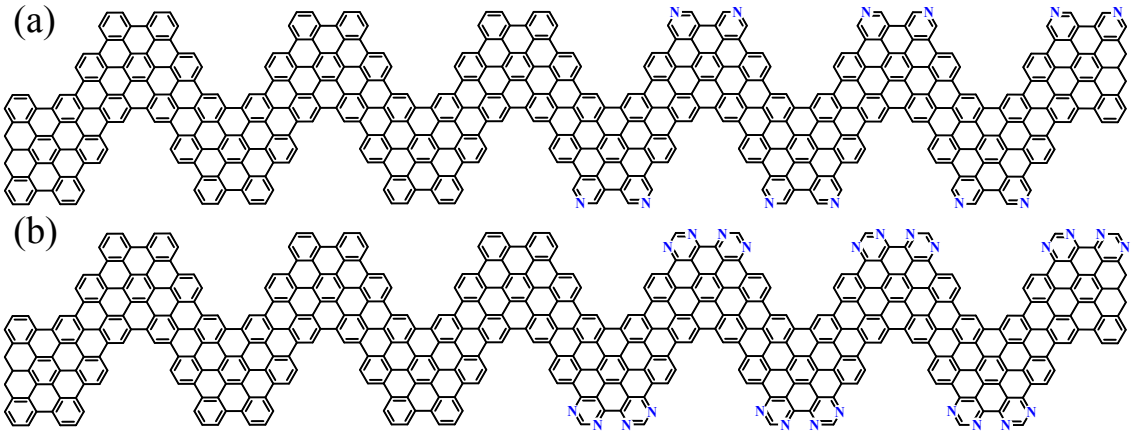

Figure 6.1: For a GNW heterojunction, the pure GNW (p-GNW) is on the left side of the interface and the nitrogen-doped GNW (N-GNW) is on the right side. There are two types of experimentally realized nitrogen doping in the GNW (9_A,6_A): (a) two nitrogen atoms per monomer unit and (b) four nitrogen atoms per monomer unit. They are denoted as N2 and N4, respectively. Then the corresponding nitrogen-doped GNWs are labeled as N2-GNW and N4-GNW, respectively. Hence, the two types of GNW heterojunctions are denoted as (a) p-N2-GNW heterojunction (b) p-N4-GNW heterojunction.

As mentioned in Fig. 2.5 of Chapter 2, nitrogen-doped GNWs with an atomically precise edge structure have been synthesized recently [22]. Furthermore, heterojunctions combining segments of pure and nitrogen-doped GNWs have been also synthesized (denoted as p-N-GNW heterojunctions) [24]. Here, we investigate two types of nitrogen doping which have been experimentally realized: two nitrogen atoms per monomer unit

(denoted as N2) and four nitrogen atoms per monomer unit (denoted as N4), as shown in Fig. 6.1. Then the corresponding nitrogen-doped GNWs are labeled as N2-GNW and N4-GNW, respectively. Hence, the heterojunction consisting of the pure GNW (p-GNW) and N2-GNW is denoted as p-N2-GNW heterojunction [Fig. 6.1(a)], and the heterojunction consisting of the p-GNW and N4-GNW is denoted as p-N4-GNW heterojunction [Fig. 6.1(b)]. For a better understanding of the nitrogen doping effects on GNW heterojunctions, we use the non-equilibrium Green's function formalism combined with density functional theory (NEGF-DFT) computational methodology to study the electronic and transport properties of heterojunctions.

6.2 Theoretical methods

Localized orbital DFT calculations have been performed with SIESTA [77] on the heterojunctions shown in Figs. 6.3(a) and 6.4(a), within GGA using the Perdew-Burke-Ernzerhof (PBE) exchange-correlation functional [31]. A real-space mesh equivalent to a plane-wave cutoff energy of 250 Ryd and the Γ-point sampling in the Brillouin zone were used. The size of the unit cell along the periodic direction was sufficiently large (in excess of 6 nm) for the Γ-point sampling to yield converged results. The basis set was composed of double-zeta with single polarization (DZP) orbitals, with an energy shift of 50 meV. All atoms were relaxed until the residue forces were all below 0.04 eV/Å. After reaching the equilibrium, the converged Hamiltonians and overlap matrices were cast in a format suitable for electronic transport and density of states calculations within NEGF formalism framework [78]. Our electronic transport codes are mainly developed by Prof. Meunier and Dr. Girão. The NEGF formalism presented below is partially taken from their works [1, 78].

6.2.1 Non-equilibrium Green's function (NEGF) formalism

Figure 6.2: Schematic of a transport system consisting of a conductor and two semi-infinite leads: left and right leads.

At nanometer distances, electrons can move ballistically through a device, without any scattering. For ballistic transport, the relation between the current I and the voltage (V) is $I = GV$, where G is the quantum conductance. The famous Landauer formula [79] relates G to the transmission coefficient $\mathscr{T}$ via

$$G = (2e^2/h)\mathscr{T}. \tag{6.1}$$

Since metallic systems have a number n of bands crossing at the Fermi level, they do typically behave like ideal n-channel ballistic conductor: every electron injected into it should pass through without scattering. The theoretical conductance should thus be a constant $G = 2 \times G_0 = 2 \times (2e^2/h) \approx 2 \times (12.9K\Omega)^{-1}$. In principle, at larger electron energies the electrons are able to probe additional bands, which would give a corresponding increase in G. In practice, the propagating electrons will be scattered by lattice defects and phonons, and the injection of electrons must proceed through contacts, which can act as strong scatterers. In addition, Luttinger liquid effects can substantially reduce conductance in the limit of weak coupling to the electrodes.

A calculation of quantum conductance requires the evaluation of the transmission probability $\mathscr{T}$ through an open system, consisting of a conductor and two or more leads [80, 81], as shown in Fig. 6.2. A popular approach to calculate the transmission probability $\mathscr{T}$ has been established by means of an entity called Green's function (GF). The GF is defined as

$$G(E) = [\varepsilon S - H]^{-1}, \tag{6.2}$$

where $\varepsilon = E \pm i\delta$ and δ being an infinitesimal real positive number ($\varepsilon = E + i\delta$ for the retarded GF G^r and $\varepsilon = E - i\delta$ for the advanced GF G^a). H and S are the Hamiltonian and overlap matrices of the system. If we partition the system into a left electrode (L), a conductor (or central region) (C), and a right electrode (R), we can write its Hamiltonian in terms of a local-orbital basis as

$$\begin{pmatrix} H_L & H_{LC} & 0 \\ H_{CL} & H_C & H_{RC} \\ 0 & H_{CR} & H_R \end{pmatrix}, \tag{6.3}$$

where H_C describes the conductor and $H_{\{L,R\}}$ represent the semi-infinite left/right leads. Also, $H_{\{L,R\}C}$ and $H_{C\{L,R\}}$ describe the interaction between the conductor and the leads. The interaction between the leads is considered as zero, corresponding to zero elements in the Hamiltonian. The overlap matrix S has a similar form to H.

For the orthogonal basis, S is simply an unity matrix I. Then from Eq. 6.2, we have

$$\begin{pmatrix} G_L & G_{LC} & G_{LR} \\ G_{CL} & G_C & G_{CR} \\ G_{RL} & G_{RC} & G_R \end{pmatrix} \begin{pmatrix} \varepsilon - H_L & -H_{LC} & 0 \\ -H_{CL} & \varepsilon - H_C & -H_{RC} \\ 0 & -H_{CR} & \varepsilon - H_R \end{pmatrix} = I, \tag{6.4}$$

and after some derivations, the GF of the central region is expressed as

$$G_C = (\varepsilon I_C - H_C - \Sigma_L - \Sigma_R)^{-1}. \tag{6.5}$$

$\Sigma_{\{L,R\}}$ are the "self-energies" of the left/right electrodes, and assume the form

$$\Sigma_{\{L,R\}} = H^{\dagger}_{\{L,R\}C} G_{\{L,R\}} H_{\{L,R\}C}, \tag{6.6}$$

where $G_{\{L,R\}} = [\varepsilon I_{\{L,R\}} - H_{\{L,R\}}]^{-1}$ are the surface GF of the semi-infinite free leads, and $H_{\{L,R\}C}$ are coupling Hamiltonians between the conductor and the leads. Therefore, the self-energies $\Sigma_{\{L,R\}}$ can be interpreted as effective potentials which describe the effects of the semi-infinite leads on the finite conductor.

One can then show that the transmission function is

$$\mathscr{T} = Tr(\Gamma_L G^r_C \Gamma_R G^a_C), \tag{6.7}$$

where $\Gamma_{\{L,R\}} = \mathrm{i}[\Sigma^r_{\{L,R\}} - \Sigma^a_{\{L,R\}}]$ for describing the coupling of the conductor to the left/right leads. The localized Hamiltonian in Eq. 6.3 is known and provided by the tight-binding methodology [82, 83] or localized-orbital DFT like SIESTA. G^r_C and G^a_C can be obtained from Eq. 6.5 as long as $\Sigma_{\{L,R\}}$ have been computed. In other words, the computation of the transmission function is reduced to the calculation of self-energies, which depend on the surface GF $G_{\{L,R\}}$ of the semi-infinite electrodes. $G_{\{L,R\}}$ can be obtained for any periodic electrode by recursively doubling the period [1, 84, 85].

Furthermore, a unique feature of the GF is that it has a direct relation to the density of electronic states (DOS) of the system, as shown below:

$$D(E) = -\frac{1}{\pi}\mathrm{Im}Tr\left(G^r(E)\right). \tag{6.8}$$

Therefore, the local DOS of the conductor and left/right leads are given as $-\frac{1}{\pi}\mathrm{Im}Tr\left(G^r_C(E)\right)$ and $-\frac{1}{\pi}\mathrm{Im}Tr\left(G^r_{\{L,R\}}(E)\right)$, respectively.

So far we have considered an orthonormal basis. The corresponding extension for the non-orthogonal case is straightforward. In this scenario we have to modify

$$(\varepsilon S - H)G = I \tag{6.9}$$

to

$$\left(\varepsilon I - \left(H - \varepsilon(S-I)\right)\right)G = (\varepsilon I - H')G = I, \tag{6.10}$$

and we can take advantage of the tools described above, but now applied to the modified Hamiltonian $H' = H - \varepsilon(S-I)$ [1].

6.3 Electronic and transport properties of p-N-GNW heterojunctions

As shown in the blue dashed line of Fig. 6.3(b), the DOS of N2-GNW [Fig. 6.3(a)] indicates that it has an electronic band gap of 1.58 eV in the energy range (-0.97, 0.61) eV, which is barely changed compared to the electronic band gap 1.56 eV of the p-GNW in the energy range (-0.67, 0.89) eV [see the red dashed line in Fig. 6.3(b)]. However, the gap energy range of the doped GNW is approximately shifted by 0.29 eV to the left compared to the pure one's gap energy range, suggesting that nitrogen doping has shifted down the Fermi level. As a result, the p-N2-GNW heterojunction should present a band alignment and indeed its DOS shows a smaller electronic gap of 1.28 eV [black solid line in Fig. 6.3(b)]. We also adopt the NEGF formalism to perform transport calculations on this heterojunction. As shown in Fig. 6.3(b), in the energy range (-0.9, -0.7) eV, the p-GNW has non-zero DOS values while DOS of the doped one is zero. Therefore, an electron in such energy range is allowed in the p-GNW while forbidden in the doped one, preventing it from transport through the heterojunction. Similarly, in the energy range

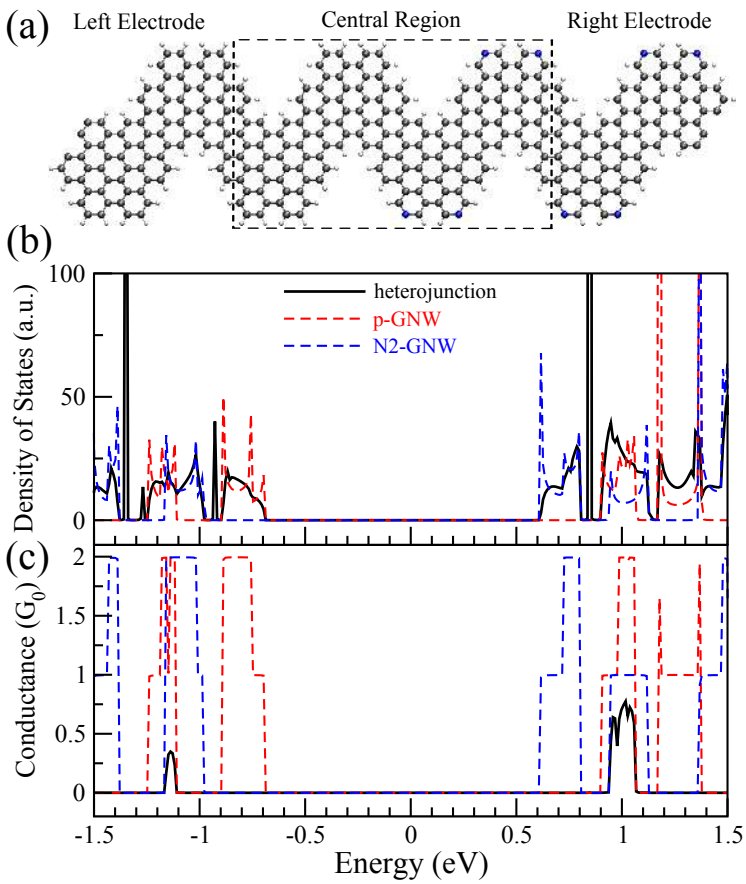

Figure 6.3: (a) Transport device built from a p-N2-GNW heterojunction. The left (right) electrode is semi-infinite in the left (right) direction. (b) Densities of states of the heterojunction (black solid line), p-GNW (red dashed line) and N2-GNW (blue dashed line). (c) Electrical conductance of the heterojunction (black solid line), p-GNW (red dashed line) and N2-GNW (blue dashed line). Fermi level of the heterojunction is at 0 eV.

(0.6, 0.8) eV, the doped GNW has non-zero DOS values while DOS of the pure one is zero, indicating that an electron in the same energy range is allowed in the doped GNW while forbidden in the pure one and hence making it impossible to transfer through the heterojunction as well. Consequently, as demonstrated in Fig. 6.3(c), the electrical conductance of the heterojunction (black solid line) is zero within both the aforementioned energy ranges. Non-zero electrical conductance is only for the energies where DOSs of both the pure and doped GNWs are non-zero, so the transport gap is as large as 2.05 eV. Compared to the electrical conductances of both the pure and doped GNWs [red and blue dashed lines in Fig. 6.3(c), respectively], the heterojunction has an overall decreased electrical conductance (due to the nitrogen scattering) and larger transport gap.

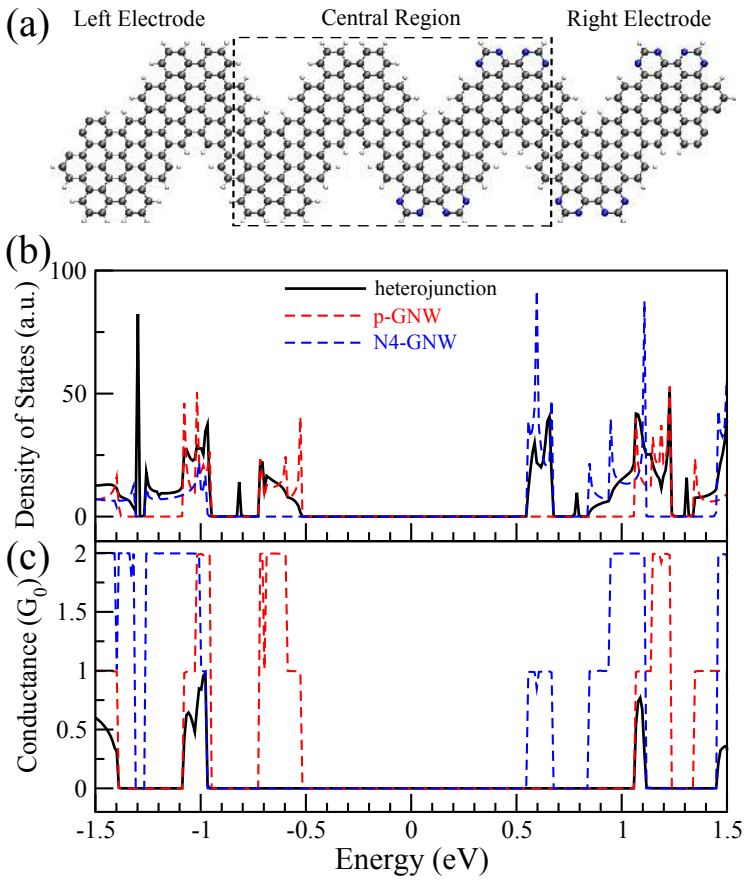

Figure 6.4: (a) Transport device built from p-N4-GNW heterojunction. The left (right) electrode is semi-infinite in the left (right) direction. (b) Densities of states of the heterojunction (black solid line), p-GNW (red dashed line) and N4-GNW (blue dashed line). (c) Electrical conductance of the heterojunction (black solid line), p-GNW (red dashed line) and N4-GNW (blue dashed line). Fermi level of the heterojunction is at 0 eV.

For the second type of nitrogen doping shown in [Fig. 6.4(a)], Fig. 6.4(b) indicates that DOS of N4-GNW has an electronic band gap of 1.50 eV in the energy range (-0.96, 0.54) eV while DOS of the p-GNW has an electronic band gap of 1.56 eV in the energy range (-0.51, 1.05) eV. Again, they have similar electronic band gaps but the gap energy range of the doped GNW is approximately shifted by 0.48 eV to the left compared to the pure one's gap energy range. So N4 nitrogen doping also shifts down the Fermi level and the heterojunction has a smaller electronic band gap of 1.05 eV [see its DOS represented by black solid line in Fig. 6.4(b)]. However, for the transport properties of the heterojunction (black solid line in Fig. 6.4(c)], due to the same argument above, the Fermi level shift leads to much larger transport gap (2.02 eV).

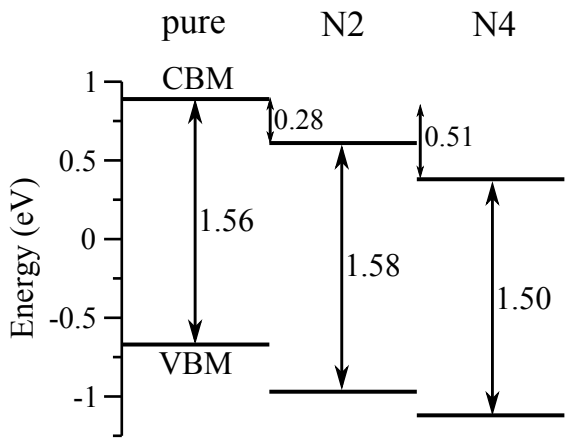

Figure 6.5: DFT calculated type-II band alignments for the pure, N2-doped and N4-doped GNWs (9_A,6_A). VBM and CBM stand for valence band maximum and conduction band minimum, respectively.

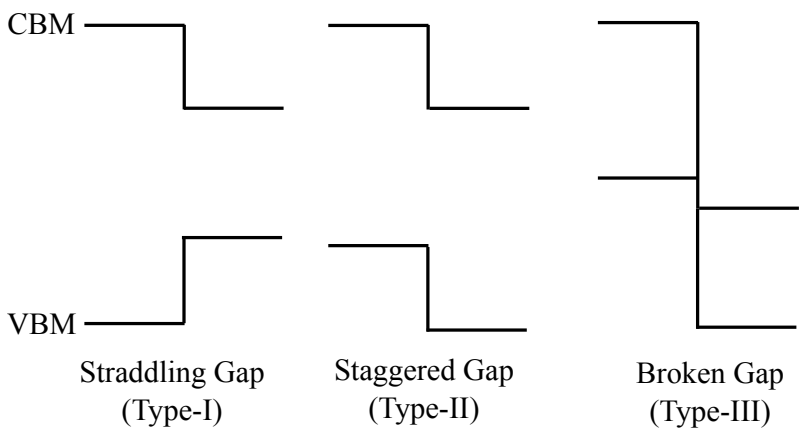

Figure 6.6: Three types of band alignments at the interface of semiconductor heterojunctions: straddling gap (type-I), staggered gap (type-II) or broken gap (type-III).

Clearly, the doping of nitrogen atoms has significant influence on the electronic and transport properties of GNW heterojunctions. More importantly, as shown in Fig. 6.5, nitrogen doping in the GNW (9_A,6_A) leads to the downshift of the Fermi level with little change of the electronic band gap, thus resulting in a band alignment at the interface of the heterojunction. Typically, there are three types of band alignments in semiconductor heterojunctions: straddling gap (type-I), staggered gap (type-II) or broken gap (type-III), as shown in Fig. 6.6. Therefore, nitrogen doping in the GNW (9_A,6_A) results in the second type of band alignment (i.e., type-II staggered band alignment). Furthermore, both the conduction and valence band offsets (ΔE_c and ΔE_v) can be tuned by nitrogen

doping concentration levels. N4 doping has twice of nitrogen concentration per monomer as N2 doping, and hence its ΔE_c (0.51 eV) is roughly twice as ΔE_c (0.28 eV) of N2 doping, as demonstrated in Fig. 6.5. So the highly-controllable nitrogen doping technique from the bottom-up fabrication approach can not only result in a type-II band alignment in the heterojunction, but also open a unique route to tailor the interface band offsets.

6.4 Type-II band alignment for solar cell applications

For the p-N-GNW heterojunctions with the type-II band alignments, free electrons and holes will be spontaneously separated, which is suited for optoelectronics and solar energy conversion. In the rest of this chapter, we will explore the potential of p-N-GNW heterojunctions for excitonic solar cell applications.

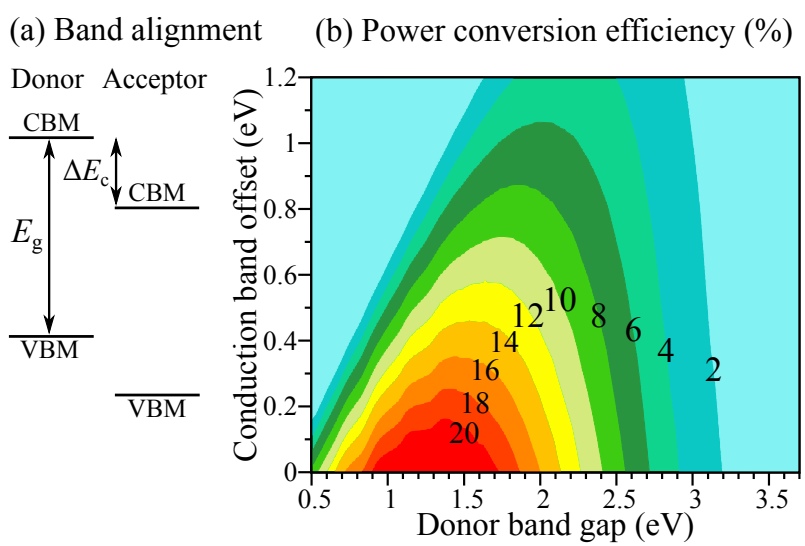

Figure 6.7: (a) Schematic diagram of the type-II band alignment with donor band gap (E_g) and conduction band offset (ΔE_c). VBM and CBM stand for valence band maximum and conduction band minimum, respectively. (b) Power conversion efficiency contour plot as a function of the donor band gap (E_g) and conduction band offset (ΔE_c).

The maximum power conversion efficiency η for an excitonic solar cell can be

estimated according to the type-II band alignment [86–89].

$$\eta = \frac{\beta_{\mathrm{FF}} V_{\mathrm{oc}} J_{\mathrm{sc}}}{P_{\mathrm{solar}}} = \frac{0.65(E_{\mathrm{g}} - \Delta E_{\mathrm{c}} - 0.3)\int_{E_{\mathrm{g}}}^{\infty} \frac{J_{\mathrm{ph}}(\hbar\omega)}{\hbar\omega} d(\hbar\omega)}{\int_{0}^{\infty} J_{\mathrm{ph}}(\hbar\omega) d(\hbar\omega)}, \tag{6.11}$$

where 0.65 is the fill factor (β_{FF}), E_{g} is the band gap of the donor, and ΔE_{c} is the conduction band offset [Fig. 6.7(a)]. V_{oc} the maximum open circuit voltage, calculated as the effective interface gap ($E_{\mathrm{g}} - \Delta E_{\mathrm{c}}$) minus 0.3 eV, which accounts for energy conversion kinetics [86, 89, 90]. Here we employ the standard AM1.5G solar spectrum (available from the NREL website: http://rredc.nrel.gov/solar/spectra/am1.5) [87, 89], as shown in Fig. 6.8. So $J_{\mathrm{ph}}(\hbar\omega)$ is the AM1.5G solar energy flux (expressed in W m^{-2} eV^{-1}) at the photon energy $\hbar\omega$, and $\frac{J_{\mathrm{ph}}(\hbar\omega)}{\hbar\omega}$ is the photon flux at the photon energy $\hbar\omega$. The integral in the numerator is the short circuit current J_{sc} calculated using a limit external quantum efficiency (EQE) of 100% (i.e., one incident photon creating one electron as photocurrent), and the denominator P_{solar} is the integrated solar energy flux, equal to 1000 W m^{-2} [87]. Since $J_{\mathrm{ph}}(\hbar\omega)$ is known from the solar spectrum, the efficiency η is a function of E_{g} and ΔE_{c}. In Fig. 6.7(b), the maximum power conversion efficiency contour plot as a function of E_{g} and ΔE_{c} is shown, and this chart can guide us for the design of a solar cell.

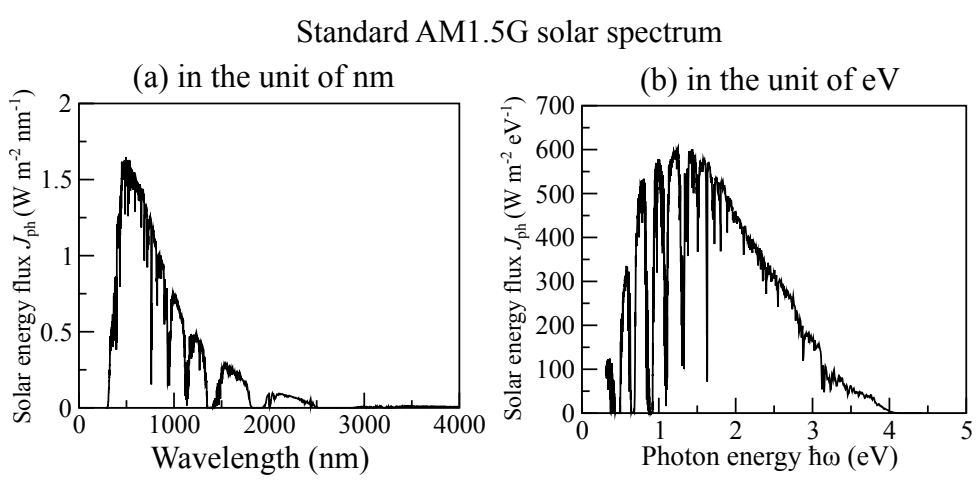

Figure 6.8: The standard AM1.5G solar spectrum with respect to (a) the wavelength (nm) and (b) the photon energy (eV). From Ref. [91].

In our case, the donor is the pure GNW (9_A,6_A) with a direct band gap at the Γ point (Fig. 3.6), and the acceptor is the nitrogen-doped GNW, as shown in Fig. 6.5. For the p-N2-GNW heterojunction, $E_g = 1.56$ eV and $\Delta E_c = 0.28$ eV, and hence its power conversion efficiency is computed as 17.1%. The p-N4-GNW heterojunction has an efficiency of about 13.1% with a $\Delta E_c = 0.51$ eV. However, it is important to point out that the band alignments obtained in Fig. 6.5 are based on DFT calculations, which tend to underestimate the band gaps of GNWs, as discussed in Chapter 3 and Chapter 5. For the p-N2-GNW interface, $E_g = 2.80$ eV and $\Delta E_c = 0.32$ eV according to experimental measurements by Bronner *et al.* [22], so the efficiency is decreased to 4.3%. For the p-N4-GNW heterojunction, Cai *et al.* measurement shows $E_g =\sim 2.0$ eV and $\Delta E_c =\sim 0.5$ eV, and hence its efficiency is computed to be about 11.3% [24]. Currently, for organic or nanomaterial-based solar cells, the best certified observed efficiency is found for a polymer solar cell (8.62%) [92] as well as nanoparticle-aided polymer solar cell (8.92%) [93], and $\eta > 10\%$ remain a challenge. Hence, for the experimentally available p-N4-GNW heterojunction [24], its maximum power conversion efficiency exceeds 10%, demonstrating its potential for solar cell applications.

6.5 Summary

In this chapter, we have considered two types of experimentally realized nitrogen doping scheme in the GNW (9_A,6_A) and studied the corresponding GNW heterojunctions: the p-N2-GNW and p-N4-GNW heterojunctions. NEGF-DFT computational method has been used to investigate the electronic and transport properties of heterojunctions. We find that nitrogen doping in the GNW (9_A,6_A) tends to shift down the Fermi level without significantly change the electronic band gap, thus resulting in a type-II band alignment at the heterojunction interface. The band alignment subsequently reduces the electronic band gap of the heterojunction and increases its transport gap. More interestingly, as the nitrogen doping concentration increases, both the conduction and valence band offsets (ΔE_c and ΔE_v) at the interface increase almost linearly. Hence, the highly-controllable (at the atomic level) nitrogen doping technique not only enables the fabrication of atomically-precise and defect-free p-N-GNW heterojunctions with type-II band alignments, but also offers a unique approach to engineer the interface band offsets of heterojunctions. The

p-N-GNW heterojunctions bear high potential for applications in electronics and photovoltaics. In particular, the recently synthesized p-N4-GNW heterojunction is estimated to have a maximum power conversion efficiency of 11.3% as an excitonic solar cell, and hence is very promising for photovoltaics.

PART II

Graphene-like materials: transition metal dichalcogenides

7. Background on transition metal dichalcogenides

This chapter provides a short overview of graphene-like materials: transition metal dichalcogenides, especially MoS_2 and WS_2. We first discuss their structural, electronic and photoluminescence properties, and then highlight their Raman spectra, which are the focus of our theoretical study.

7.1 Structural, electronic and photoluminescence properties of TMDs

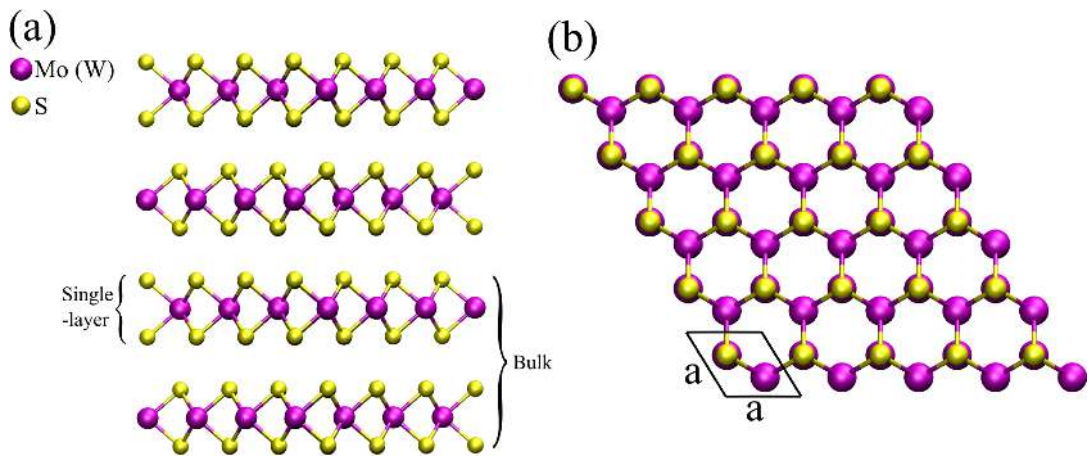

Figure 7.1: (a) Side view of MoS_2 bulk and single layer (analogous for WS_2). (b) Top view of MoS_2 (analogous for WS_2) with the unit cell delineated. The interaction between layers is dominated by vdW forces. The hexagonal lattice similar to graphene is clearly seen in (b). The primitive vectors are $\vec{a} = (a,0,0)$, $\vec{b} = (-a/2, \sqrt{3}a/2, 0)$, and $\vec{c} = (0,0,c)$. According to experimental data [94], $a = 3.15$ and $c = 12.3$ Å for MoS_2; $a = 3.153$ and $c = 12.323$ Å for WS_2.

Transition metal dichalcogenides (TMDs) MX_2 (M = Mo, W; X = S) are layered structures stacked by van der Waals (vdW) forces, where one X-M-X layer is a covalently bonded hexagonal quasi-2D network [96, 97]. As shown in Fig. 7.1, for one layer, a plane of Mo (or W) atoms is sandwiched covalently between two planes of S atoms in a trigonal prismatic arrangement [98]. From the top view [Fig. 7.1(b)], a hexagonal lattice consisting of Mo (or W) and S atoms is clearly seen, similar to graphene and hexagonal boron nitride (h-BN).

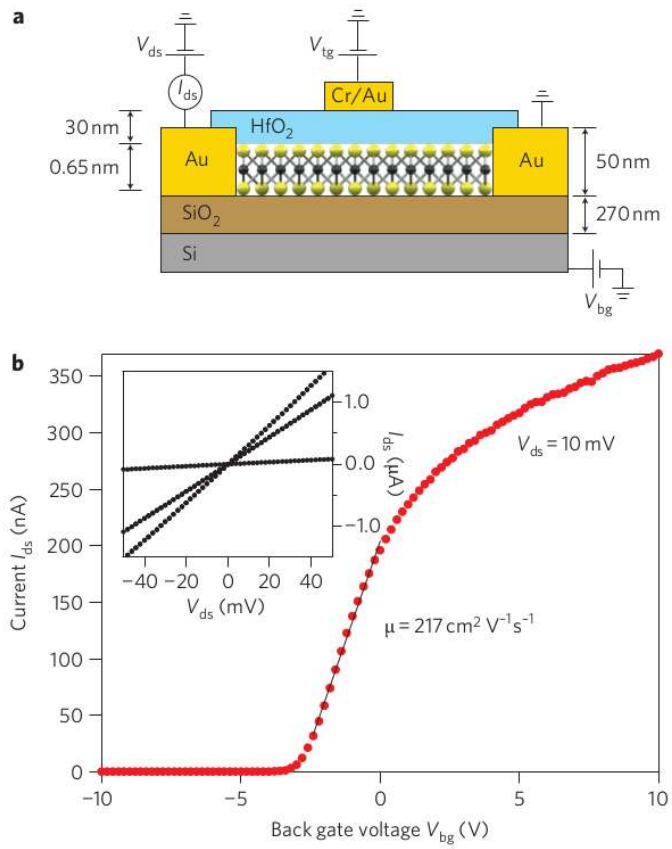

Figure 7.2: (a) A monolayer MoS_2 field-effect transistor (FET) connected to external electrodes. MoS_2 is deposited on a degenerately doped silicon substrate with 270-nm-thick SiO_2. The substrate acts as a back gate. One of the gold electrodes acts as drain and the other source electrode is grounded. The monolayer is separated from the top gate by 30 nm of ALD-grown HfO_2. The top gate width for the device is 4 mm and the top gate length, source-gate and gate-drain spacings are 500 nm. (b) Room temperature transfer characteristic for the FET with 10 mV applied bias voltage V_{ds}. Back-gate voltage V_{bg} is applied to the substrate and the top gate is disconnected. Inset: I_{ds}-V_{ds} curve acquired for V_{bg} values of 0, 1 and 5 V. From Ref. [95].

Bulk MoS_2 is an attractive semiconducting material for photovoltaic and photocatalyst applications [99]. However, it is the monolayer MoS_2 that has been attracting increasing research attention. Using the similar mechanical exfoliation technique leading to the fabrication of atomically thin graphene from vdW-bonded graphite [3], monolayer MoS_2 can be obtained from vdW-bonded bulk MoS_2 [95]. For pristine graphene, despite its high electronic mobility, the absence of a band gap makes its use in electronic devices (transistors) difficult. Although single layers of MoS_2 have a large intrinsic band gap of 1.8 eV [100], their mobilities have been reported to be in the 0.5-3 $cm^2V^{-1}s^{-1}$ range

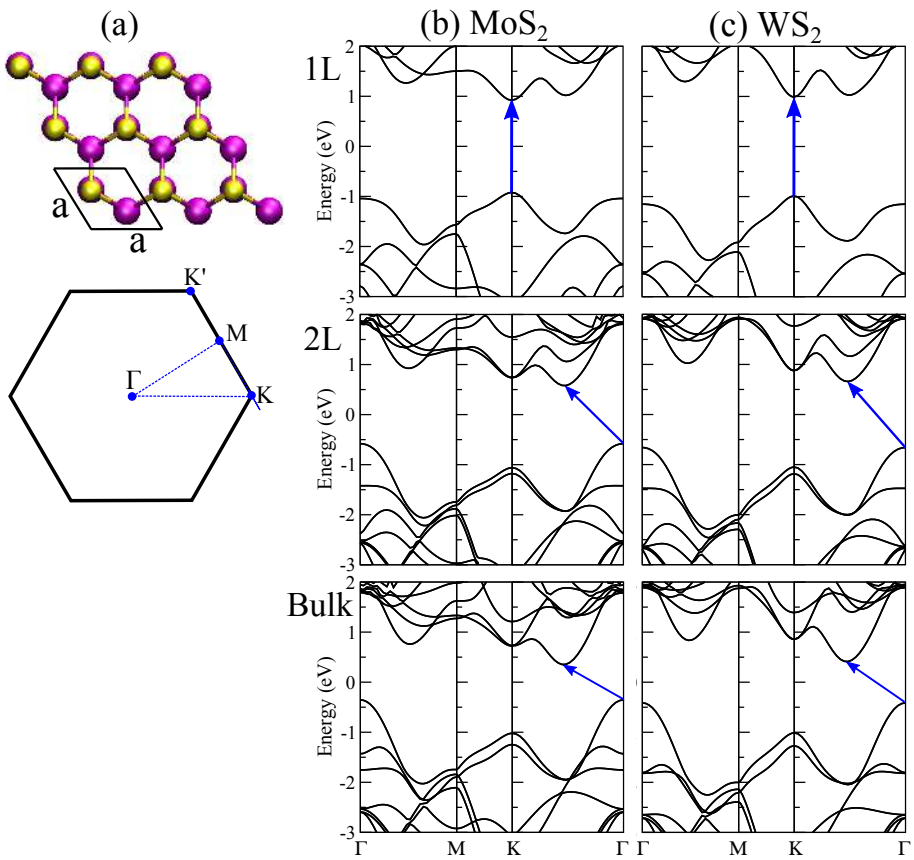

Figure 7.3: (a) The hexagonal lattice and corresponding 2D Brillouin zone for MoS_2 or WS_2. (b) Along the high symmetry lines in the Brillouin zone, DFT calculated electronic band structures of (b) MoS_2 and (c) WS_2 from the bulk (bottom panels) to double-layer (2L, middle panels) to single-layer (1L, top panels). The solid blue arrows indicate the lowest energy transitions. The Fermi level is set at 0 eV.

[101], too low for practical devices. Recently, by putting a halfnium oxide (HfO_2) gate dielectric on top of monolayer MoS_2, a field-effect transistor (FET) based on MoS_2 shows an enhanced room temperature electron mobility close to that of graphene nanoribbons (at least 200 $cm^2V^{-1}s^{-1}$) and a current on/off ratio up to 10^8 [95], as shown in Fig. 7.2. Such breakthrough has spurred tremendous interests in MoS_2 and a variety of its family members such as WS_2, $MoSe_2$, WSe_2, etc.

In addition to enhanced electron mobilities, MoS_2 and WS_2 also exhibit interesting electronic band structures [104]. As shown in Fig. 7.3, from the bulk phase to single-layer phase, a transition from indirect to direct electronic band gap occurs in both MoS_2 and WS_2. The direct band gaps in monolayer systems result in a dramatic enhancement of photoluminescence (PL) [100, 102]. In Fig. 7.4(a), single-layer MoS_2 has been measured

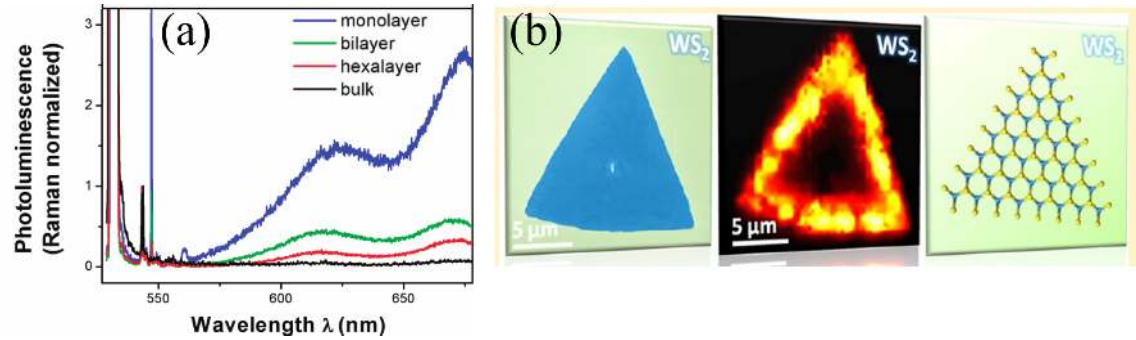

Figure 7.4: (a) Photoluminescence (PL) spectra normalized by Raman intensity for MoS_2 layers with different thickness, showing a dramatic increase of luminescence efficiency in MoS_2 monolayer. From Ref. [102]. (b) Photoluminescence map of a WS_2 triangular island. The edges of WS_2 monolayers exhibit PL signals with extraordinary intensity, around 25 times stronger than that at the platelets center. From Ref. [103].

to show significantly higher luminescence efficiency [102]. Single-layer WS_2 triangular islands have been also synthesized and found to show intense room temperature PL associated with specific edges [103], as shown in Fig. 7.4(b). These superior optical and electronic properties make ultrathin MoS_2 and WS_2 attractive for numerous applications, and they have been considered as replacements or complements to graphene in nanoscale applications.

7.2 Raman spectra of TMDs

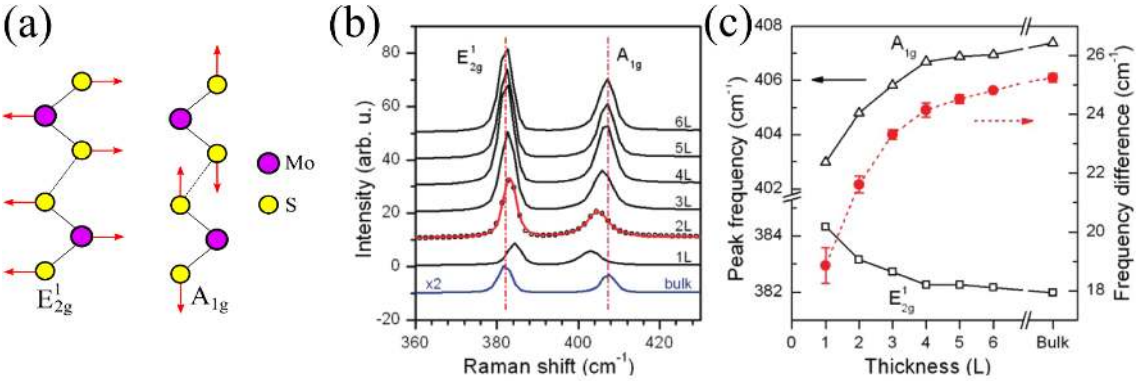

Figure 7.5: (a) Schematic of Raman-active modes E^1_{2g} and A_{1g} of bulk MoS_2. (b) Raman spectra of thin (nL) and bulk MoS_2 films. (c) Frequencies of E^1_{2g} and A_{1g} (left vertical axis) and their difference (right vertical axis) as a function of layer thickness. From Ref. [105].

Since atomically thick MoS_2 and WS_2 become increasingly important, their precise characterization and easy identification are in high demand [98]. Raman spectroscopy is a powerful nondestructive characterization tool used extensively to study MoS_2 [98, 105–108] and WS_2 [96, 109, 110]. Bulk MoS_2 shows two main Raman-active peaks, the in-plane E^1_{2g} mode at $\sim$382 cm^{-1} and out-of-plane A_{1g} mode at $\sim$407 cm^{-1} [105, 111], as shown in Fig. 7.5(a) and Fig. 7.5(b). In Fig. 7.5(c), The former red-shifts while the latter blue-shifts with the number of layers, and thus their frequency difference can be used to identify the number of layers [105]. A similar thickness dependence of frequencies of E^1_{2g} and A_{1g} modes has been observed in WS_2 [110].

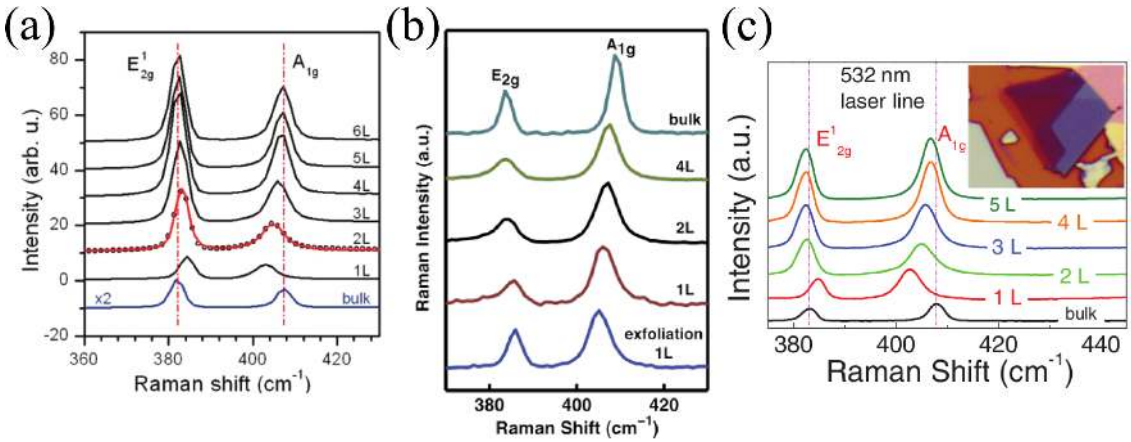

Figure 7.6: Raman spectra of MoS_2 films from (a) Ref. [105], (b) Ref. [106] and (c) Ref. [98].

However, it remains unclear how Raman intensities and intensity ratio depend on the materials' thickness. As shown in Fig. 7.6(a), Lee *et al.* [105] reported that, for MoS_2 on SiO_2/Si substrates with a laser wavelength of 514.5 nm, Raman intensities rise up from one to four layers and then decrease for thicker samples, while the peak intensity ratio between E^1_{2g} and A_{1g} is always higher than 1. Yu *et al.* [106] found that, for MoS_2 on SiO_2/Si substrates with a laser wavelength of 532 nm, the peak intensity ratio between E^1_{2g} and A_{1g} remains lower than unity regardless of thickness [Fig. 7.6(b)]. Reporting on MoS_2 deposited on the same substrate with various laser wavelengths, Li *et al.* [98] found that Raman intensities and intensity ratio of the E^1_{2g} and A_{1g} peaks vary arbitrarily with thickness [Fig. 7.6(c)]. Similar conflicting results about Raman intensities and intensity ratio have been observed in WS_2 [96, 109].

7.3 Overview for the rest of Part II

To further understand Raman spectra of TMDs, for free-standing and defect-free MoS_2 and WS_2 up to six-layer-thick, we have carried out first-principles DFT calculations to simulate their Raman spectra in Chapter 8. We quantitatively analyze the laser polarization effect on the intensity ratio and reveal the high sensitivity of the intensity ratio to laser polarization. We also study the Raman spectra of MoS_2/WS_2 heterostructures up to four layers in Chapter 8 to facilitate their identification.

8. First-principles Raman spectra of MoS_2, WS_2 and their heterostructures

In this chapter, Raman spectra of MoS_2, WS_2, and their heterostructures are studied by density functional theory. We quantitatively reproduce existing experimental data and present evidence that the apparent discrepancy between intensity ratios observed experimentally can be explained by the high sensitivity of the Raman-active modes to laser polarization. MoS_2/WS_2 heterostructures up to four layers are considered in every possible combinations and stacking orders. Each heterostructure configuration possesses a unique Raman spectrum in both frequency and intensity that can be explained by changes in dielectric screening and interlayer interactions [112].

8.1 Introduction

As mentioned in Chapter 7, MoS_2 and WS_2 have enjoyed increasing attention due to their superior electronic and optical properties. Raman spectroscopy is a powerful nondestructive characterization tool used extensively to study them. However, it remains unclear how Raman intensities and intensity ratio depend on the materials' thickness. Numerous factors can contribute to this puzzling result: sample quality, substrate [105, 113], laser polarization [110], laser wavelength [98, 109], etc. To clarify this issue, in this chapter, we choose free-standing and defect-free MoS_2 and WS_2 up to six-layer-thick, and perform first-principles DFT calculations to simulate their Raman spectra and reveal the intrinsic thickness dependence of Raman intensities and intensity ratio of E^1_{2g} and A_{1g} modes. We quantitatively analyze the laser polarization effect on the intensity ratio and reveal the high sensitivity of the intensity ratio to laser polarization. We also study the Raman spectra of MoS_2/WS_2 heterostructures up to four layers to predict the influence of thickness and stacking orders on the details of the spectra [112].

This chapter previously appeared as: L. Liang and V. Meunier, Nanoscale **6**, 5394 (2014).

8.2 Theoretical methods

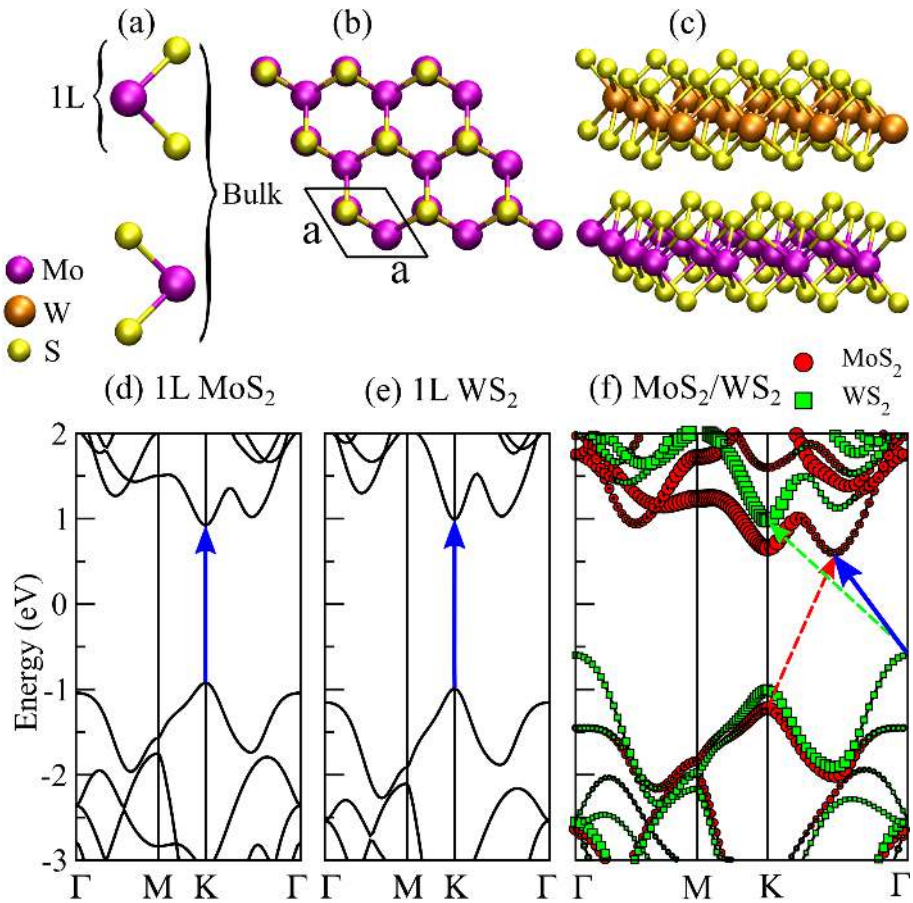

Figure 8.1: (a) Side view of MoS_2 bulk and single layer (1L in short). (b) Top view of MoS_2 with the unit cell delineated (analogous for WS_2). (c) Heterostructure consisting of 1L MoS_2 and 1L WS_2. Electronic band structures of (d) 1L MoS_2, (e) 1L WS_2 and (f) the heterostructure shown in (c). The solid blue arrows indicate the lowest energy transitions. In (f), red circles (green squares) correspond to projected bands of the MoS_2 (WS_2) layer with the red (green) dashed arrow showing the layer's lowest energy transition. The Fermi level is set at 0 eV.

As shown in Figs. 8.1(a) and 8.1(c), for one layer, a plane of Mo (or W) atoms is sandwiched covalently between two planes of S atoms in a trigonal prismatic arrangement [98]. The interaction between layers is dominated by vdW forces. From the top view [Fig. 8.1(b)], a hexagonal lattice consisting of Mo (or W) and S atoms is clearly seen, similar to graphene and hexagonal boron nitride (h-BN). Its primitive vectors are $\vec{a} = (a,0,0)$, $\vec{b} = (-a/2, \sqrt{3}a/2, 0)$, and $\vec{c} = (0,0,c)$. The symmetry space group of bulk MoS_2 or WS_2 is $P6_3/mmc$ (point group D_{6h}). The space group of MoS_2 or WS_2 with

odd number of layers is P6m2 (point group D_{3h}), while systems with even number of layers belong to P3m1 (point group D_{3d}). All systems exhibit two signature Raman-active modes: E^1_{2g} and A_{1g} for bulk systems, E' and A'_1 for systems with odd number of layers, and E_g and A_{1g} for systems with even number of layers [114, 115]. For simplicity, the notations of E^1_{2g} and A_{1g} are used for all systems studied below, which is a common practice in the literature [98, 105].

The calculations of Raman scattering start with the determination of the equilibrium geometries. Plane-wave DFT calculations were performed using the VASP package [36] equipped with the projector augmented-wave (PAW) method [116] for electron-ion interactions. Local density approximation (LDA) has been shown to yield excellent description of graphite [117], h-BN [118], graphene/h-BN heterostructures [119] and MoS_2 [94]. Hence, LDA was adopted here for the exchange-correlation interaction with the energy cutoff set at 500 eV. For bulk MoS_2 and WS_2, both atoms and cell volumes were allowed to relax until the residual forces were below 0.001 eV/Å. We used a $24 \times 24 \times 4$ k-point sampling in the Monkhorst-Pack scheme [38]. The optimized lattice parameters of MoS_2 are $a = 3.130$ and $c = 12.039$ Å (experimental values $a = 3.15$ and $c = 12.3$ Å) [94]. For WS_2, $a = 3.131$ and $c = 12.115$ Å (experimental data $a = 3.153$ and $c = 12.323$ Å) [94]. Obviously, LDA slightly underestimates lattice parameters since it tends to overestimate covalent binding. Single- and few-layer systems, including MoS_2/WS_2 heterostructures, were modeled by a periodic slab geometry using optimized bulk in-plane lattice constants. A vacuum spacing of 18 Å in the z direction was used to avoid spurious interactions with replicas. For the 2D slab calculations, all atoms were relaxed until the residual forces were below 0.001 eV/Å and we used a $24 \times 24 \times 1$ k-point sampling. Since the in-plane lattice mismatch between MoS_2 and WS_2 is very small ($\sim$0.1%) [94, 104], the probability of stacking disorders in MoS_2/WS_2 heterostructures is expected to be much smaller than that in graphene/h-BN or $MoS_2/MoSe_2$ heterostructures [120]. Hence, for MoS_2/WS_2 heterostructures, we adapt the in-plane lattice constant of MoS_2 and considered no stacking disordering.

We performed non-resonant first-order Raman calculations using the fully relaxed

geometries. The Raman intensity of the j-th phonon mode is given by [121–123]

$$\frac{d\sigma}{d\Omega} = N_{prim}\frac{\omega_s^4}{c^4 V_{prim}}|\mathbf{g}_s \cdot \boldsymbol{\alpha}(j) \cdot \mathbf{g}_i^T|^2 \times \frac{\hbar}{2\omega_j}(n_j+1), \tag{8.1}$$

where ω_i and ω_s are the frequencies of the incoming and scattered light, respectively; ω_j is the frequency of the j-th phonon mode of the crystal. Energy conservation imposes $\omega_s = \omega_i \mp \omega_j$, where the minus (plus) sign applies to the Stokes (anti-Stokes) process. In the non-resonant Raman scattering, ω_i only appears in the prefactor ω_s^4. V_{prim} is the volume of primitive unit cell, N_{prim} is the number of primitive unit cells in the sample, and c is the speed of light. The Bose factor of the j-th phonon mode is $n_j = (e^{\hbar\omega_j/k_BT} - 1)^{-1}$. $\mathbf{g}_i$ and $\mathbf{g}_s$ are the polarization vectors of the incoming and scattered light.

The Raman susceptibility $\boldsymbol{\alpha}(j)$ is a symmetric (3×3) tensor associated with the j-th phonon mode. It can be computed as [121, 122]

$$\boldsymbol{\alpha}_{\alpha\beta}(j) = V_{prim}\sum_{\mu=1}^{N}\sum_{l=1}^{3}\frac{\partial\chi_{\alpha\beta}}{\partial r_l(\mu)}\frac{e_l^j(\mu)}{\sqrt{M_\mu}}, \tag{8.2}$$

where $\chi_{\alpha\beta} = (\varepsilon_{\alpha\beta} - \delta_{\alpha\beta})/4\pi$ is the electric polarizability tensor related to tensor of dielectric constant $\varepsilon_{\alpha\beta}$. $r_l(\mu)$ is the position of μ-th atom along direction l. $\frac{\partial\chi_{\alpha\beta}}{\partial r_l(\mu)}$ is the first derivative of the polarizability tensor (essentially the dielectric constant tensor) over the atomic displacement. $e_l^j(\mu)$ is the displacement of μ-th atom along direction l in the j-th phonon mode, and M_μ is the mass of μ-th atom. Note that e^j and ω_j^2 are the eigenvectors and eigenvalues of the dynamical matrix at the Brillouin zone center, respectively [122].

The dynamic matrix at the Brillouin zone center is defined as [94, 121]

$$\begin{aligned} D_{\mu l,\nu k}(\mathbf{q{=}0}) &= \frac{1}{\sqrt{M_\mu M_\nu}}\frac{\partial^2 E_{\text{tot}}}{\partial r_l(\mu)\partial r_k(\nu)} \\ &= -\frac{1}{\sqrt{M_\mu M_\nu}}\frac{\partial F_l(\mu)}{\partial r_k(\nu)}. \end{aligned} \tag{8.3}$$

To obtain Raman scattering from Eqs. (8.1-8.2), one needs to calculate the dynamic matrix and derivatives of the dielectric constant tensor. The dynamic matrix was calculated using the *ab initio* direct method [124], implemented in the PHONON software

[123]. In the finite difference scheme [46], the Hellmann-Feynman forces of the supercell were computed by VASP for both positive and negative atomic displacements (0.03 Å) and used in PHONON to construct the dynamic matrix, whose diagonalization provides phonon frequencies ω_j and normal vectors e^j. The derivatives of the dielectric constant tensor were also calculated by the finite difference approach. For both positive and negative atomic displacements in the single unit cell, the dielectric tensors were computed by VASP using density functional perturbation theory and then imported into PHONON to generate their derivatives. Then Raman intensity for every phonon mode was obtained for a given laser polarization set-up ($\mathbf{g}_i$, $\mathbf{g}_s$) and wavelength to finally yield the Raman spectrum after Gaussian broadening.

8.3 Electronic and dielectric properties of MoS_2 and WS_2

The electronic band structures of monolayer (1L) MoS_2, WS_2 and their bilayer heterostructure are shown in Figs. 8.1(d-f). Both 1L MoS_2 and WS_2 exhibit the well-documented direct band gaps [102, 104]. The heterostructure 1L MoS_2/1L WS_2 presents an indirect band gap, as highlighted by the solid blue arrow in Fig. 8.1(f), consistent with previous theoretical results [125]. Similar indirect band gaps are observed for multilayer and bulk MoS_2 and WS_2 [102, 104]. To further verify that the direct band gap is not preserved in the individual layer component of the heterostructure, we also computed their projected bands, as shown by red circles and green squares in Fig. 8.1(f). Clearly, the interlayer coupling between MoS_2 and WS_2 yields indirect band gaps, as indicated by the red and green dashed arrows, just as in multilayer homostructures. Interestingly, in the heterostructure, the lowest energy transition paths [three arrows in Fig. 8.1(f)] of 1L MoS_2, 1L WS_2 and the whole system are quite different from one another.

The thickness dependence of band gaps of MoS_2 and WS_2 was also studied and shown in Fig. 8.2(a). From 1L to bulk MoS_2 (WS_2), the band gap decreases monotonically from 1.84 (1.98) eV to 0.71 (0.82) eV [104]. The noticeable jump of the band gap from 2L and 1L is another sign of the indirect-to-direct gap transition. For semiconducting MoS_2 and WS_2, non-diagonal elements of the dielectric constant tensor ε are zero, and the in-plane dielectric constants $\varepsilon_{xx} = \varepsilon_{yy}$ due to symmetry. We also computed the thickness dependence of ε_{xx} and ε_{zz} of MoS_2 and WS_2, as shown in Fig. 8.2(b). From 1L

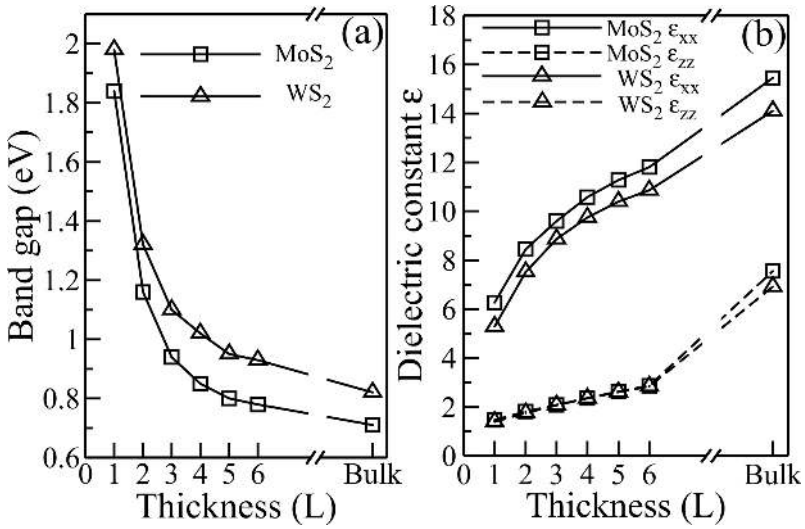

Figure 8.2: DFT calculated thickness dependence of (a) electronic band gaps and (b) dielectric constants of MoS_2 and WS_2. For dielectric tensor ε, non-diagonal elements are zero and $\varepsilon_{xx} = \varepsilon_{yy}$.

to bulk MoS_2, ε_{xx} (ε_{zz}) monotonically increases from 6.269 (1.471) to 15.452 (7.553), in agreement with previous calculations [94]. Similar trend is also observed for WS_2 [lines with triangles in Fig. 8.2(b)]. A semiconductor with a smaller band gap generally has larger dielectric constants, and hence the variations of band gaps and dielectric constants with thickness show opposite trends.

8.4 Raman spectra of MoS_2 and WS_2

Fig. 8.3(a) shows *ab initio* Raman spectra of free-standing MoS_2 with various thicknesses using a 488 nm laser line. The polarization of incident and scattered light are set as to $\mathbf{g}_i$=$\mathbf{g}_s$=(1,0,0). The in-plane E^1_{2g} and out-of-plane A_{1g} Raman modes [Fig. 8.3(b)] exhibit the strongest signals among all phonon modes. For single-layer MoS_2, the calculated frequencies of E^1_{2g} and A_{1g} are 391.50 and 411.07 cm^{-1}, respectively. Compared to experimental data ~384.3 (E^1_{2g}) and ~403 (A_{1g}) cm^{-1} [98, 105], our LDA calculations systematically overestimate the phonon frequencies by ~7-8 cm^{-1}, since LDA tends to overbind. Despite the limits of LDA, it successfully reproduces the experimentally observed continuous red-shift of E^1_{2g} and blue-shift of A_{1g} with increasing thickness [98, 105], as shown in solid lines in Fig. 8.3(c). More importantly, it is the frequency difference between A_{1g} and E^1_{2g} that is an effective indicator of the number of layers. The systematic

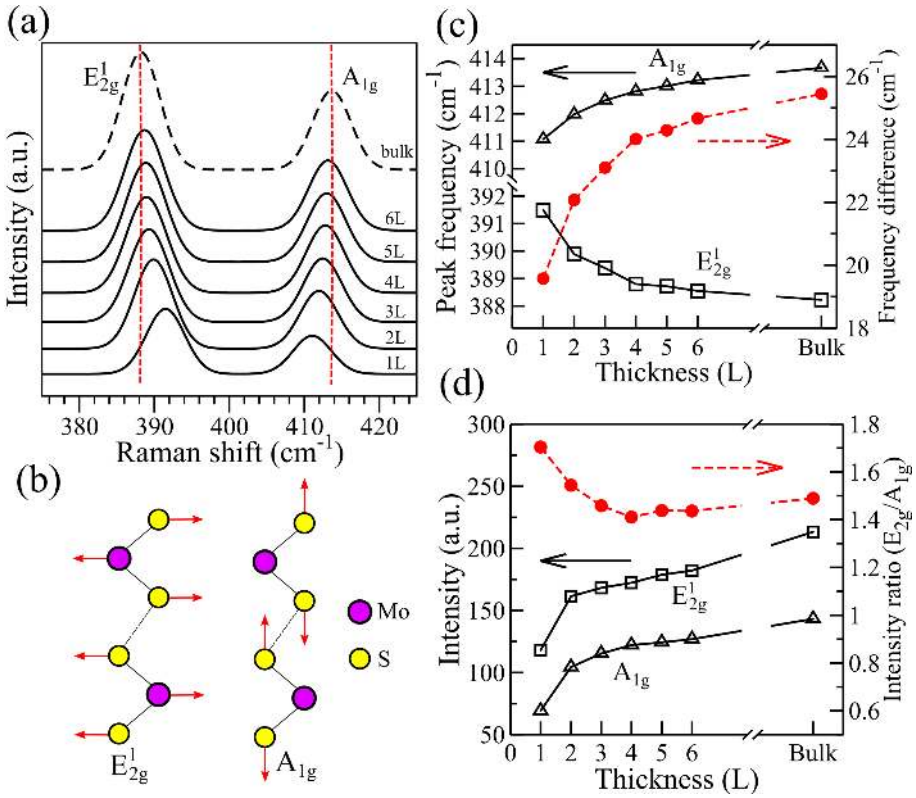

Figure 8.3: (a) *Ab initio* Raman spectra of free-standing *n*-layer (*n*L) and bulk MoS_2, with laser polarization $\mathbf{g}_i$=$\mathbf{g}_s$=(1,0,0) and wavelength 488 nm. (b) Schematic of Raman-active modes E^1_{2g} and A_{1g} of bulk MoS_2. (c) Frequencies of E^1_{2g} and A_{1g} (left vertical axis) and their difference (right vertical axis) as a function of layer number. (d) Peak intensities of E^1_{2g} and A_{1g} (left vertical axis) and their intensity ratio (right vertical axis) as a function of thickness.

overestimation of frequencies by LDA is expected to be largely canceled out for the frequency difference. Indeed, from 1L to bulk MoS_2 [red dashed line in Fig. 8.3(c)], the computed frequency difference monotonically increases from 19.57 (experimental value $\sim$18.7) cm^{-1} to 25.44 (experimental value $\sim$25.5) cm^{-1}, in excellent agreement with experimental data and confirming the frequency difference as a reliable thickness indicator [105]. As for the mechanisms, the upshift of A_{1g} with increasing thickness is due to the increasing interlayer interactions which enhance the effective restoring forces acting on the atoms, while the unexpected downshift of E^1_{2g} with increasing thickness has been attributed to the increasing dielectric screening of the long-range Coulomb forces which reduces the overall restoring force on the atoms [94, 105]. The interlayer coupling and dielectric screening are also vital to explain Raman scattering of the heterostructures

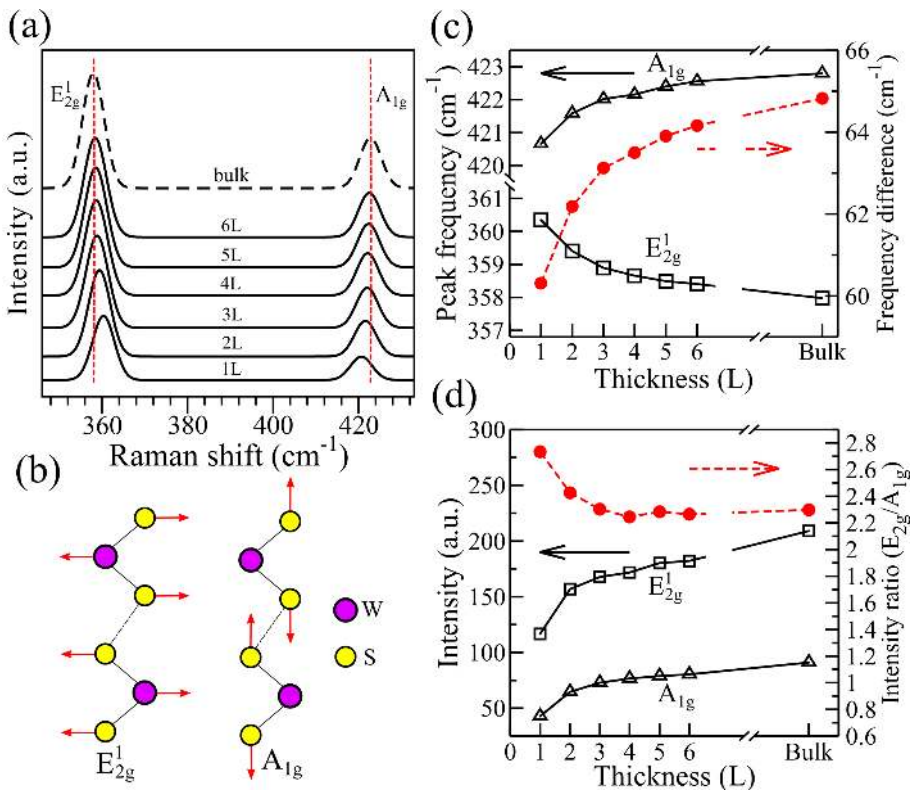

Figure 8.4: (a) *Ab initio* Raman spectra of free-standing *n*-layer (*n*L) and bulk WS_2, with laser polarization $\mathbf{g}_i$=$\mathbf{g}_s$=(1,0,0) and wavelength 488 nm. (b) Schematic of Raman-active modes E^1_{2g} and A_{1g} of bulk WS_2. (c) Frequencies of E^1_{2g} and A_{1g} (left vertical axis) and their difference (right vertical axis) as a function of layer number. (d) Peak intensities of E^1_{2g} and A_{1g} (left vertical axis) and their intensity ratio (right vertical axis) as a function of layer number.

discussed below.

Ab initio Raman spectra of free-standing WS_2 are also presented in Fig. 8.4(a) with the same laser conditions as those used for MoS_2. E^1_{2g} and A_{1g} modes still exhibit strongest Raman signals. However, the frequencies of WS_2 E^1_{2g} mode at any thickness are softened by more than 30 cm^{-1} compared to those of MoS_2 E^1_{2g}, due to the larger mass of W atoms. For A_{1g} mode in which only sulfur atoms vibrate [Fig. 8.3(b)], WS_2 has larger frequencies than MoS_2 by more than 9 cm^{-1}. For WS_2 [solid lines in Fig. 8.4(c)], our calculations show again the experimentally observed monotonic downshift of E^1_{2g} and upshift of A_{1g} with increasing thickness [110]. Hence, the frequency difference between A_{1g} and E^1_{2g} [red dashed line in Fig. 8.4(c)] increases monotonically from 60.31 to 64.82 cm^{-1}, in great agreement with experimental data [110] and confirming the frequency

difference as a reliable thickness indicator for WS_2 too.

Despite that phonon frequencies have been extensively studied [94, 126, 127], little has been reported regarding a systematic DFT study on Raman intensities of MoS_2 and WS_2 [114]. Here we focus on the evolution of Raman peak intensities with thickness. For free-standing MoS_2 and WS_2, the peak intensities of E^1_{2g} and A_{1g} increase significantly from 1L to 2L and then slowly increase until converging to bulk values [solid lines in Fig. 8.3(d) and Fig. 8.4(d) respectively]. Indicated by Eqs. (8.1-8.2), Raman intensity is directly related to derivatives of the dielectric tensor. As discussed above, the dielectric tensor increases with thickness, hence contributing to the increase of peak intensity with thickness. Furthermore, 1L MoS_2 has the highest peak intensity ratio between E^1_{2g} and A_{1g} (1.71). The intensity ratio drops until 4L and then converges to the bulk value (1.49) [red dashed line in Fig. 8.3(d)]. Similarly, 1L WS_2 has the highest intensity ratio (2.73), while decreases until 4L and then recovers the bulk value (2.30) [red dashed line in Fig. 8.4(d)].

8.5 Laser polarization effect on Raman spectra

The calculated thickness dependence of peak intensities and intensity ratio is not consistent with experimental observations. In fact, as mentioned in Chapter 7, there is also a large discrepancy among different experimental works. For MoS_2 on SiO_2/Si substrates, Lee *et al.* reported that Raman intensities rise up to four layers and then decrease for thicker samples with the peak intensity ratio always higher than 1 [105], and Yu *et al.* found that the intensity ratio stays lower than 1 at any thickness [106], while Li *et al.* claimed that Raman intensities and intensity ratios vary arbitrarily with thickness [98]. Similar conflicting results have been observed for WS_2 [96, 109]. The optical interference occurring between incident and scattered laser light, enhanced by SiO_2/Si substrates [105, 113], has been considered as a plausible explanation for the observed puzzling behavior of Raman intensities with thickness. Our work on free-standing MoS_2 and WS_2 without substrate and optical interference effects reveals the intrinsic thickness dependence of Raman intensities, and thus the deviation from experimental observations to some extent is expected. However, since the substrate and optical interference effects are expected to similarly affect both E^1_{2g} and A_{1g} modes [105, 113], the discrepancy between

the computed and measured intensity ratios, and particularly the inconsistency between measured intensity ratios by different experimental groups, are perplexing. Keys to addressing this issue can be found by examining Eq. (8.1): this relationship establishes that Raman intensity depends on the polarization of incident and scattered light $\mathbf{g}_i$ and $\mathbf{g}_s$ (i.e., laser set-up). To quantify the effect of laser polarization on intensity ratios, we now carefully explore different laser set-ups.

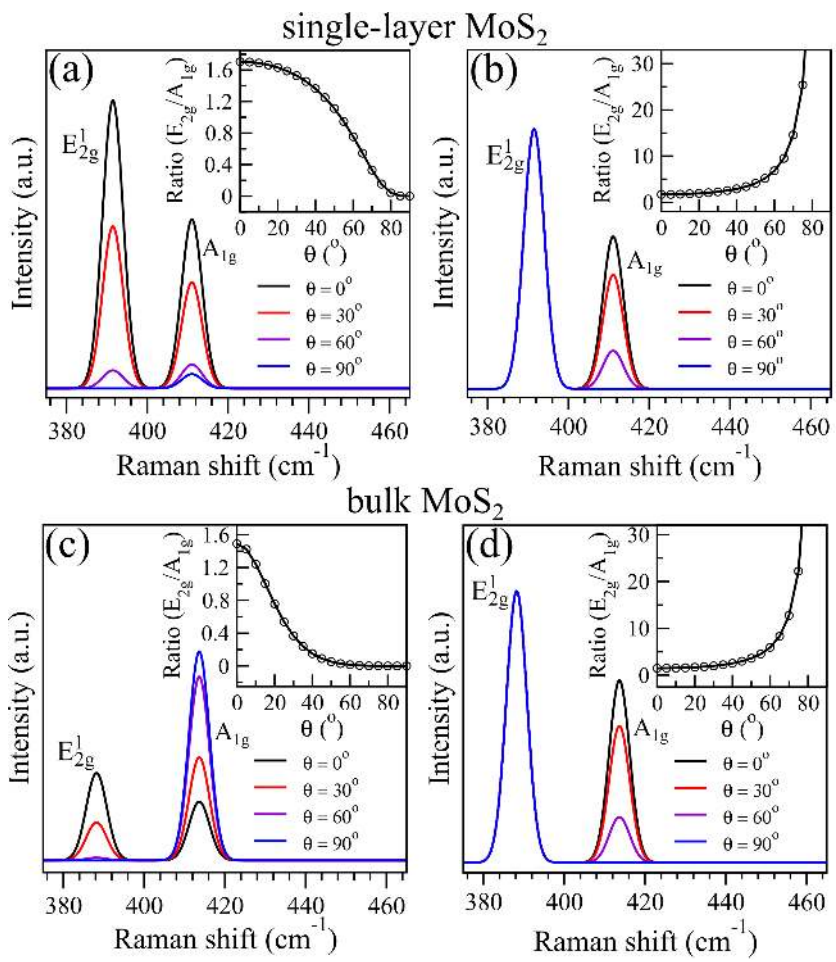

Figure 8.5: Raman spectra of (a) single-layer and (c) bulk MoS_2 with laser polarization $\mathbf{g}_i$=$\mathbf{g}_s$=($\cos\theta$,0,$\sin\theta$). Raman spectra of (b) single-layer and (d) bulk MoS_2 with laser polarization $\mathbf{g}_i$=(1,0,0) and $\mathbf{g}_s$=($\cos\theta$,$\sin\theta$,0). In (a) and (c), some of Raman spectra are scaled for comparison purpose. The inset figures show the intensity ratio between E^1_{2g} and A_{1g} as a function of θ.

The in-plane E^1_{2g} mode is double-degenerated and can vibrate along the x and y directions. The out-plane A_{1g} mode is non-degenerated. For E^1_{2g}-x, E^1_{2g}-y and A_{1g} modes,

the Raman tensor $\boldsymbol{\alpha}(j)$ in Eq. (8.2) assume well-defined forms

$$\begin{pmatrix} . & a & . \\ a & . & . \\ . & . & . \end{pmatrix}, \begin{pmatrix} a & . & . \\ . & -a & . \\ . & . & . \end{pmatrix} \text{and} \begin{pmatrix} b & . & . \\ . & b & . \\ . & . & c \end{pmatrix},$$

respectively. Other terms in the Raman tensors are either zero or negligible due to symmetry [121, 122]. From Eq. (8.1), Raman intensity $I \propto |\mathbf{g}_s \cdot \boldsymbol{\alpha}(j) \cdot \mathbf{g}_i^T|^2$. Hence, when the laser polarization is set as $\mathbf{g}_i$=$\mathbf{g}_s$=(cos θ,0,sin θ),

$$\begin{aligned} I(\mathrm{A_{1g}}) &\propto \left| (\cos\theta, 0, \sin\theta) \begin{pmatrix} b & . & . \\ . & b & . \\ . & . & c \end{pmatrix} \begin{pmatrix} \cos\theta \\ 0 \\ \sin\theta \end{pmatrix} \right|^2 \\ &\propto \left| (b-c)\cos^2\theta + c \right|^2 \end{aligned} \tag{8.4}$$

and similar matrix operations yield $I(\mathrm{E^1_{2g}}\text{-}x) = 0$, $I(\mathrm{E^1_{2g}}\text{-}y) \propto a^2\cos^4\theta$ and $I(\mathrm{E^1_{2g}}) = I(\mathrm{E^1_{2g}}\text{-}x) + I(\mathrm{E^1_{2g}}\text{-}y) \propto a^2\cos^4\theta$. Therefore, when θ is tuned from 0° to 90°, $I(\mathrm{E^1_{2g}})$ monotonically decreases from its maximum to zero for both single-layer and bulk MoS_2 [Fig. 8.5(a) and Fig. 8.5(c)]. For single-layer MoS_2, $b > c$, and hence $I(\mathrm{A_{1g}})$ monotonically reduces from maximum to minimum with θ tuned from 0° to 90° [Fig. 8.5(a)]. In contrast, $b < c$ for bulk MoS_2, and thus $I(\mathrm{A_{1g}})$ monotonically increases from minimum to maximum with θ varied from 0° to 90° [Fig. 8.5(c)]. For both single-layer and bulk MoS_2, with θ tuned from 0° to 90°, the intensity ratio between $\mathrm{E^1_{2g}}$ and $\mathrm{A_{1g}}$ monotonically decreases to absolute zero [inset figures in Fig. 8.5(a) and Fig. 8.5(c)]. In another laser set-up $\mathbf{g}_i$=(1,0,0) and $\mathbf{g}_s$=(cos θ,sin θ,0), following matrix operations in Eq. (8.4), we have $I(\mathrm{E^1_{2g}}\text{-}x) \propto a^2\sin^2\theta$, $I(\mathrm{E^1_{2g}}\text{-}y) \propto a^2\cos^2\theta$, $I(\mathrm{E^1_{2g}}) = I(\mathrm{E^1_{2g}}\text{-}x) + I(\mathrm{E^1_{2g}}\text{-}y) \propto a^2$, and $I(\mathrm{A_{1g}}) = b^2\cos^2\theta$. $I(\mathrm{E^1_{2g}})$ is independent of θ and unchanged when θ is tuned from 0° to 90°, while $I(\mathrm{A_{1g}})$ monotonically decreases from its peak to zero for both single-layer and bulk MoS_2 [Fig. 8.5(b) and Fig. 8.5(d)], in agreement with recent Raman measurements [110, 115]. Hence, the intensity ratio between $\mathrm{E^1_{2g}}$ and $\mathrm{A_{1g}}$ monotonically increases to infinity with θ tuned from 0° to 90° [inset figures in Fig. 8.5(b) and Fig. 8.5(d)]. Similar results are found for WS_2 too, as shown in Fig. 8.6.

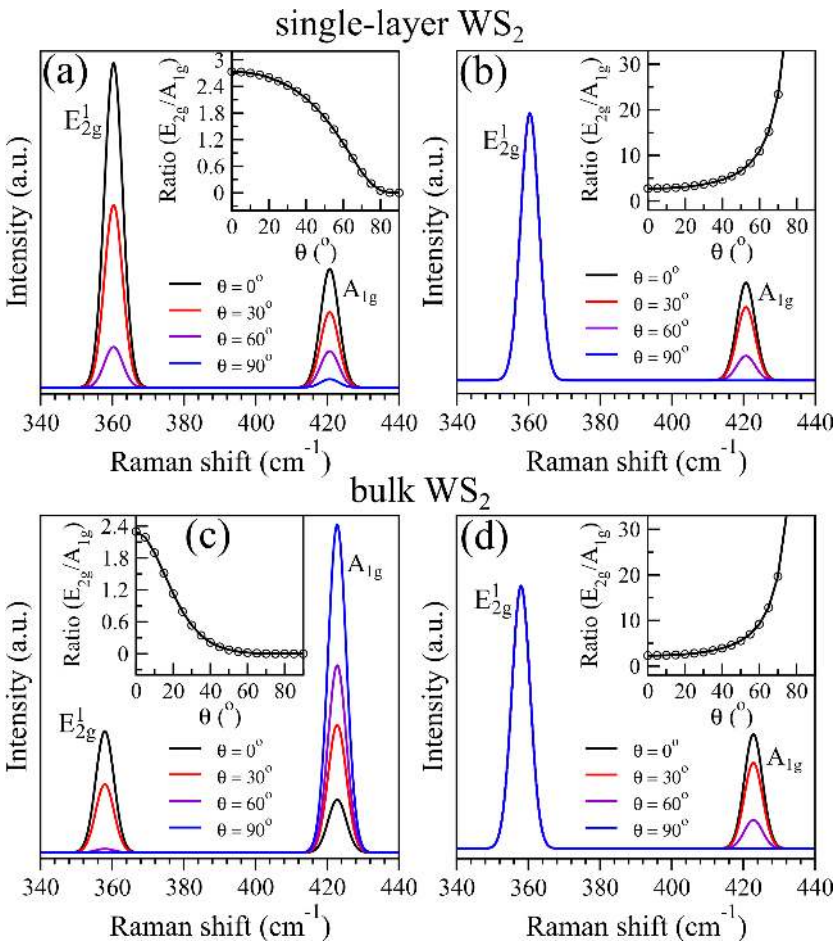

Figure 8.6: Raman spectra of (a) single-layer and (c) bulk WS_2 with laser polarization $\mathbf{g}_i$=$\mathbf{g}_s$=($\cos\theta$,0,$\sin\theta$). Raman spectra of (b) single-layer and (d) bulk WS_2 with laser polarization $\mathbf{g}_i$=(1,0,0) and $\mathbf{g}_s$=($\cos\theta$,$\sin\theta$,0). In (a) and (c), some of Raman spectra are scaled for comparison purpose. The inset figures show the intensity ratio between E^1_{2g} and A_{1g} as a function of θ.

For both MoS_2 and WS_2, our calculations show that the intensity ratio between E^1_{2g} and A_{1g} is very sensitive to the laser set-up and can be essentially tuned from 0 to infinity, which could be key to explaining the large discrepancy between measured intensity ratios by different experimental groups. Even in the same experimental work using the same laser set-up, the samples with different layers could have different orientations, equivalent to different polarization set-ups for the samples with the same orientation, which might lead to the arbitrary evolution of the intensity ratio with thickness observed by Li *et al.* [98]. Note that in the non-resonant first-order Raman scattering, the laser frequency ω_i only appears in the prefactor $(\omega_i \mp \omega_j)^4$ in Eq. (8.1), and ω_i is typically in the range

18797-30769 cm^{-1} (laser wavelength typically in the range 325-532 nm), much larger than frequencies ω_j of E^1_{2g} and A_{1g} modes (between 358 and 423 cm^{-1}). Thus, the prefactor $(\omega_i \mp \omega_j)^4 \approx \omega_i^4$ and hence the laser frequency affects both modes identically, exerting essentially no influence on the intensity ratio.

8.6 Raman scattering of MoS_2/WS_2 heterostructures

Table 8.1: Frequency differences and intensity ratios for MoS_2, WS_2 and their heterostructures.

(a) For MoS_2 and WS_2, $\Delta\omega$ indicates frequency differences between A_{1g} and E^1_{2g} modes. Mo (W) means 1L MoS_2 (WS_2), MoMo (WW) means 2L MoS_2 (WS_2), etc.

stacking	Mo	MoMo	MoMoMo	MoMoMoMo
$\Delta\omega$ (cm^{-1})	19.58	22.08	23.10	24.01
stacking	W	WW	WWW	WWWW
$\Delta\omega$ (cm^{-1})	60.31	62.18	63.13	63.50

(b) For heterostructures, $\Delta\omega$-Mo ($\Delta\omega$-W) means frequency differences between A_{1g} and E^1_{2g} modes of MoS_2 (WS_2), and r-E^1_{2g} (r-A_{1g}) means the intensity ratio between MoS_2 and WS_2 E^1_{2g} (A_{1g}).

stacking	$\Delta\omega$-Mo (cm^{-1})	$\Delta\omega$-W (cm^{-1})	r-E^1_{2g}	r-A_{1g}
MoW	20.83	61.33	0.96	0.90
MoMoW	22.90	61.53	1.89	2.29
MoWMo	20.94	62.26	1.45	1.02
MoWW	21.04	62.97	0.50	0.46
WMoW	22.06	61.82	0.60	0.51
MoMoMoW	23.98	61.34	2.99	3.63
MoMoWMo	22.37	62.61	1.89	1.64
MoMoWW	23.07	62.80	0.93	1.13
MoWMoW	21.47	62.31	0.89	0.67
MoWWMo	20.58	63.55	0.74	0.70
WMoMoW	23.45	61.31	1.22	1.16
MoWWW	20.41	63.38	0.30	0.31
WMoWW	21.91	62.45	0.41	0.35

For vdW-bonded layered systems such as graphite, h-BN and MX_2, layers can be micromechanically separated and reassembled to form heterostructures, which could

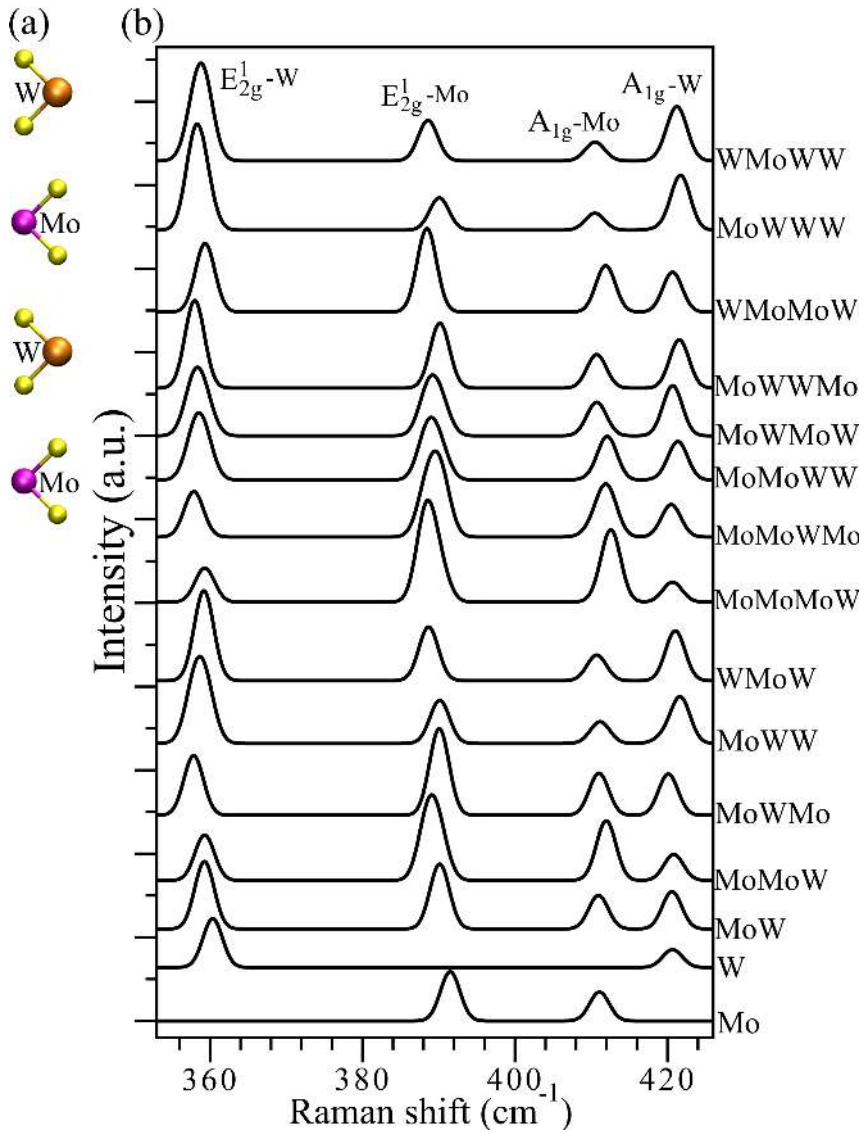

Figure 8.7: (a) A MoS_2/WS_2 heterostructure. For simplicity, a MoS_2 (WS_2) layer is denoted as Mo (W). So the heterostructure is named as MoWMoW for its stacking pattern. (b) *Ab initio* Raman spectra of various MoS_2/WS_2 heterostructures, with laser polarization $\mathbf{g}_i$=$\mathbf{g}_s$=(1,0,0) and wavelength 488 nm. The Raman spectra of single-layer MoS_2 (Mo) and WS_2 (W) are also shown for comparison.

show combined functionality of the individual layers, lead to new emergent properties and thus are very desirable [97, 111]. Here, we carefully examine first-principles Raman scattering of MoS_2/WS_2 heterostructures (Fig. 8.7) to establish that their Raman spectra can be used to identify the stoichiometry and stacking patterns. For simplicity, a MoS_2 (WS_2) layer is denoted as Mo (W) in Fig. 8.7. Hence, MoW stands for the heterostructure 1L MoS_2/1L WS_2, MoMoW for 2L MoS_2/1L WS_2, and MoMoWW for 2L MoS_2/2L

WS_2, etc. From 2L to 4L heterostructures, Raman spectra of all non-equivalent stacking patterns are examined in Fig. 8.7(b). For MoW, its Raman spectrum shows features of both MoS_2 and WS_2. Compared to the Raman spectra of Mo and W in Fig. 8.7(b), the E^1_{2g} peak of MoW corresponding to Mo (E^1_{2g}-Mo) is clearly red-shifted, and the E^1_{2g} peak of MoW corresponding to W (E^1_{2g}-W) is red-shifted too, while A_{1g}-Mo and A_{1g}-W peaks of MoW are barely shifted. As mentioned above, red-shift of E^1_{2g}-Mo of MoW is due to the increased dielectric screening to the Mo layer in the presence of the W layer, and vice versa [94]. For MoW, its $\Delta\omega$-Mo ($\Delta\omega$-W), the frequency difference between A_{1g} and E^1_{2g} of MoS_2 (WS_2) inside the heterostructure, is 20.83 (61.33) cm^{-1}, according to Table 8.1(b). From Table 8.1(a), $\Delta\omega$ are 19.58 and 22.08 cm^{-1} for Mo and MoMo, respectively. $\Delta\omega$ are 60.31 and 62.18 cm^{-1} for W and WW, respectively. Obviously, $\Delta\omega$-Mo of MoW is between $\Delta\omega$ of Mo and MoMo, and its $\Delta\omega$-W is between $\Delta\omega$ of W and WW. In other words, for MoW, the addition of the W (Mo) layer leads to an increase of $\Delta\omega$ of the Mo (W) layer but not as significant as the addition of another Mo (W) layer.

For 3L heterostructures MoMoW in Fig. 8.7(b), compared to MoW, its E^1_{2g}-Mo peak is red-shifted (due to increased dielectric screening to Mo) while A_{1g}-Mo peak is blue-shifted (due to increased interlayer interaction to Mo), while its E^1_{2g}-W and A_{1g}-W peaks are hardly shifted (since little environment change of W). Therefore, $\Delta\omega$-Mo of MoMoW is increased to 22.90 cm^{-1} [Table 8.1(b)], between $\Delta\omega$ of MoMo and MoMoMo [Table 8.1(a)]. Similarly, for MoWW in Fig. 8.7(b), compared to MoW, its E^1_{2g}-W peak is red-shifted (due to increased dielectric screening to W) while A_{1g}-W peak is blue-shifted (due to increased interlayer interaction to W), while its E^1_{2g}-Mo and A_{1g}-Mo peaks are hardly shifted (since the environment of Mo is hardly modified). Hence, $\Delta\omega$-W of MoWW is increased to 62.97 cm^{-1} [Table 8.1(b)], between $\Delta\omega$ of WW and WWW [Table 8.1(a)]. Similarly, for MoMoW (MoWW), the addition of the W (Mo) layer increases $\Delta\omega$ of the Mo (W) layers but not as significant as the addition of another Mo (W) layer. Another interesting phenomenon is that $\Delta\omega$-Mo and $\Delta\omega$-W for the heterostructures are also sensitive to stacking patterns. For MoWMo in Fig. 8.7(b), compared to MoMoW, the dielectric screening to W is increased since the W layer is now sandwiched between two Mo layers, while the dielectric screening to Mo is decreased. It follows that the E^1_{2g}-W peak of MoWMo is clearly red-shifted while its E^1_{2g}-Mo peak is blue-shifted.

Therefore, in spite of the same stoichiometry of Mo:W, from MoMoW to MoWMo in Table 8.1(b), $\Delta\omega$-W increases from 61.53 to 62.26 cm^{-1}, while $\Delta\omega$-Mo decreases from 22.90 to 20.94 cm^{-1}. Conversely, from MoWW to WMoW in Fig. 8.7(b), the dielectric screening to Mo (W) is increased (decreased) and thus the E^1_{2g}-Mo (E^1_{2g}-W) peak is red-shifted (blue-shifted). Hence in Table 8.1(b), in spite of the same stoichiometry, from MoWW to WMoW, $\Delta\omega$-Mo increases from 21.04 to 22.06 cm^{-1}, while $\Delta\omega$-W decreases from 62.97 to 61.82 cm^{-1}. For 4L heterostructures, similar trends can be observed in Fig. 8.7 and Table 8.1.

As discussed above, frequency difference $\Delta\omega$ has been established as a reliable thickness indicator for pure MoS_2 and WS_2. For heterostructures, the distinctive dependence of $\Delta\omega$-Mo and $\Delta\omega$-W on both stoichiometry and stacking patterns revealed in Table 8.1 can be very valuable to determine both stoichiometry and stacking patterns. Turning to intensity ratios, we defined r-E^1_{2g} (r-A_{1g}) as the intensity ratio between MoS_2 and WS_2 E^1_{2g} (A_{1g}) in the heterostructures. They are also found to exhibit unique dependence on both stoichiometry and stacking patterns.

With a laser set-up $\mathbf{g}_i$=$\mathbf{g}_s$=(1,0,0) in Table 8.1(b), r-E^1_{2g} and r-A_{1g} of MoW are 0.96 and 0.90 respectively, close to the stoichiometry of Mo:W (1:1). For MoMoW, r-E^1_{2g} (r-A_{1g}) grows to 1.89 (2.29), around the stoichiometry of Mo:W (2:1). For MoWW, r-E^1_{2g} (r-A_{1g}) drops to 0.50 (0.46), around the stoichiometry of Mo:W (1:2). For MoMoMoW, r-E^1_{2g} (r-A_{1g}) is 2.99 (3.63), around the stoichiometry of Mo:W (3:1). For MoWWW, r-E^1_{2g} (r-A_{1g}) is 0.30 (0.31), close to the stoichiometry of Mo:W (1:3). Hence, r-E^1_{2g} and r-A_{1g} can be an indicator of the stoichiometry of heterostructures. Furthermore, r-E^1_{2g} and r-A_{1g} are sensitive to the stacking order as well. Based on the same argument applied for pure MoS_2 and WS_2 above, from MoMoW to MoWMo, the dielectric screening to W (Mo) is increased (decreased), the localized band gap of W (Mo) is decreased (increased), the effective dielectric constant tensor of W (Mo) is slightly increased (decreased), and thus Raman intensities of W (Mo) should be increased (decreased). Indeed, from MoMoW to MoWMo in Fig. 8.7(b), Raman intensities of E^1_{2g}-W and A_{1g}-W are increased while those of E^1_{2g}-Mo and A_{1g}-Mo are slightly decreased, and hence r-E^1_{2g} (r-A_{1g}) is decreased to 1.45 (1.02) in Table 8.1(b). Similarly, from MoMoMoW to MoMoWMo, the dielectric screening to W (Mo) is increased (decreased), Raman intensities of W (Mo)

are increased (decreased) [Fig. 8.7(b)], and hence r-E^1_{2g} and r-A_{1g} are decreased [Table 8.1(b)]. On the contrary, from MoWW to WMoW, the dielectric screening to Mo (W) is increased (decreased), eventually leading to the increase of r-E^1_{2g} and r-A_{1g} in Table 8.1(b). From MoWWW to WMoWW, the dielectric screening to Mo (W) is again increased (decreased), and thus r-E^1_{2g} and r-A_{1g} are increased.

8.7 Summary

In this chapter, we have performed a comprehensive first-principles study of Raman scattering of MoS_2, WS_2 and their heterostructures. For MoS_2 and WS_2, our calculations successfully reproduce the experimentally observed continuous downshift of E^1_{2g} mode and upshift of A_{1g} mode with increasing thickness. The increasing dielectric screening (interlayer coupling) is found to be responsible for the downshift of E^1_{2g} (upshift of A_{1g}) with increasing thickness. In MoS_2/WS_2 heterostructures, the same dielectric screening and interlayer coupling effects lead to a distinctive dependence of $\Delta\omega$-Mo and $\Delta\omega$-W on both the stoichiometry and stacking patterns.

For free-standing MoS_2 and WS_2, we also report the intrinsic thickness dependence of Raman intensities and intensity ratio of E^1_{2g} and A_{1g} modes. More importantly, both Raman intensities and intensity ratio are found to be very sensitive to the laser set-up, and we reveal how the intensity ratio can be essentially tuned from zero to infinity by adjusting laser polarization, which might explain the inconsistency in measured intensity ratios by different experimental groups. For the heterostructures, r-E^1_{2g} and r-A_{1g} shows a distinctive dependence on both the stoichiometry and stacking patterns as well, in which the dielectric screening plays a key role. The combination of $\Delta\omega$-Mo, $\Delta\omega$-W, r-E^1_{2g} and r-A_{1g} in Table 8.1 is expected to serve as a guideline for experimental characterization of the heterostructures. Despite that our data cannot be absolutely quantitatively accurate due to precision limit of theoretical methods, the revealed trends and the underlying mechanisms (particularly dielectric screening effect) are expected to hold.

Very recently, surface effects have been proposed by Luo *et al.* as an alternative mechanism to explain the anomalous downshift of E^1_{2g} with increasing thickness [114]. For MoS_2, surface effects refer to the larger Mo-S force constants at the surface of thin film MoS_2, which results from a loss of neighbors in adjacent MoS_2 layers. With increas-

ing thickness, there are more neighbors from adjacent layers and hence surface force constants decrease, resulting in the frequency decrease of E^1_{2g}. It is still under alive debate whether dielectric screening [94] or surface effects [114] are responsible for the downshift of E^1_{2g} with increasing thickness. Nevertheless, surface effects can be also applied to explain the dependence of the E^1_{2g}-Mo and E^1_{2g}-W peaks on both stoichiometry and stacking patterns in the heterostructures. For example, from MoMoW to MoWMo in Figure 8.7(b), the surface force constants of W are decreased since the W layer is now sandwiched between two Mo layers (more neighbors), while the surface force constants of Mo are increased (less neighbors). It follows that the E^1_{2g}-W peak of MoWMo is clearly red-shifted while its E^1_{2g}-Mo peak is blue-shifted. In short, the conclusions made for heterostructures hold no matter which mechanism (dielectric screening or surface effects) is predominant.

PART III

Fe-based superconductors: spin-dependent surface reconstruction

9. Spin ordering in the (1×2) surface reconstruction of $Ca(Fe_{1-x}Co_x)_2As_2$

In the previous chapters, we have focused on theoretical studying of graphene nanowiggles and transition metal dichalcogenides. Here, we focus on the experimental collaboration project with Prof. Plummer's group from Louisiana State University: surface reconstruction of layered Fe-based superconductors $CaFe_2As_2$.

Low energy electron diffraction, scanning tunneling microscopy and spectroscopy, and first-principles spin-dependent density functional theory are utilized to investigate the geometric, electronic, and magnetic structures of the stripe-ordered (1×2) surface of $Ca(Fe_{1-x}Co_x)_2As_2$ ($x = 0, 0.075$). The surface is terminated with a 50% Ca layer. Compared to the bulk, the surface Ca layer has a large inward relaxation (∼0.5 Å), and the underneath As-Fe_2-As layer displays a significant buckling. First-principles calculations show that the (1×2) phase is stabilized by the bulk anti-ferromagnetic spin ordering through the spin-charge-lattice coupling. Strikingly, a superconducting gap (∼7 meV at 7.4 K) is observed on such surface ($x = 0.075$ compound), suggesting the coexistence of both superconductivity and AFM ordering at the surface [128].

9.1 Introduction

The discovery of high-temperature superconductivity (SC) in layered Fe-based compounds has brought to the attention of the materials community a very interesting class of materials [129–134]. One of the most intriguing aspects of these materials is the coupling of structure, magnetism, and superconductivity. There is a concurrent structural and magnetic transition in AFe_2As_2 (or A122 where A = Ba, Sr, Ca) [Fig. 9.1(a)]: from tetragonal (Tet) - paramagnetic (PM) at high temperatures to orthorhombic (Ort)-anti-ferromagnetic (AFM) at low temperatures [129, 135]. The coupled transitions split and decrease in

---

This chapter previously appeared as: G. Li, L. Liang, Q. Li, M. Pan, V. Nascimento, X. He, A. Karki, V. Meunier, R. Jin, J. Zhang, and E. Plummer, Phys. Rev. Lett. **112**, 077205 (2014).

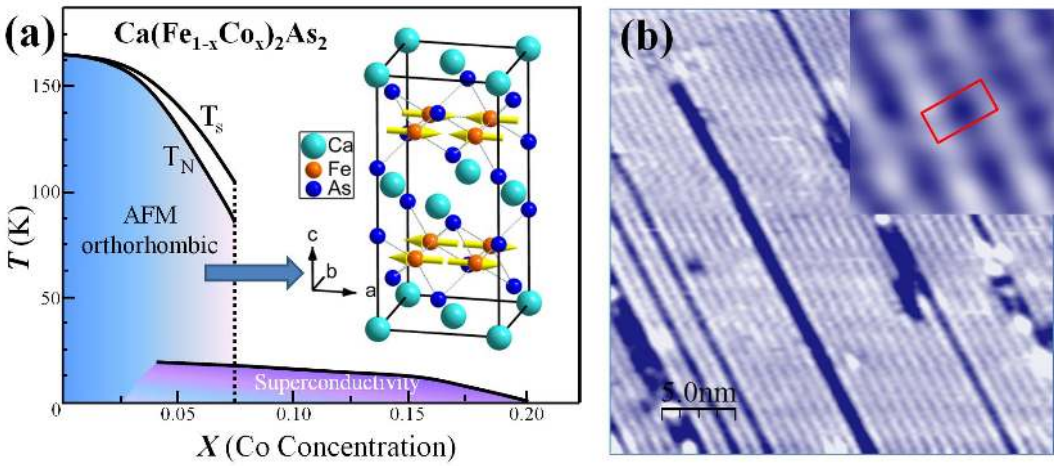

Figure 9.1: (a) Phase diagram of $Ca(Fe_{1-x}Co_x)_2As_2$. Inset is the schematic view of the orthorhombic unit cell with spin structure; (b) STM topography of stripe-ordered surface on $CaFe_2As_2$ at (V_{bias} = 1.0 V, I_t = 200 pA). Inset is the zoom-in image, where the red rectangle shows the (1×2) unit cell.

temperature with chemical doping [Fig. 9.1(a)] or the application of hydrostatic pressure [136]. Unlike compounds such as $SmFeAsO_{1-x}F_x$ [137] and $CeFeAsO_{1-x}F_x$ [138], superconductivity in A122 seems to emerge prior to the complete suppression of AFM [135]. As shown in [Fig. 9.1(a)], $Ca(Fe_{1-x}Co_x)_2As_2$ has an apparent overlap of superconducting and AFM phases in the bulk underdoped region [135].

There is growing evidence that the creation of a surface by cleaving stabilizes the orthorhombic phase [130, 134] and presumably AFM ordering. For example, the surface of $Ba(Fe_{1-x}Co_x)_2As_2$ exhibits a higher transition temperature than observed in the bulk [130]. Topographic measurements of $BaFe_2As_2$ show that the surface stabilizes its structure with an enhanced orthorhombicity. The domain structure at $BaFe_2As_2$ surface is further locked by AFM ordering, indicated by the broken mirror symmetry at the domain boundaries [134]. Interestingly, a superconducting energy gap is observed in such a surface. Recently, scanning tunneling microscopy (STM) studies of $K_{0.73}Fe_{1.67}Se_2$ revealed that superconductivity is observed at the surface with a charge-modulation resulting from the block-AFM ordering of the Fe layer [139]. Another STM study on $NaFe_{1-x}Co_xAs$ speculated that a spin density wave (SDW) gap coexists with SC gap at the surface [139]. However, to figure out whether these phenomena are surface properties or associated with the bulk, it is important to first develop a detailed understanding of the surface structure,

and then its connection to magnetism and superconductivity.

AFM ordering at the surface is difficult to probe directly, and thus has to be determined indirectly. Here, we present a study of the (1×2) surface of $Ca(Fe_{1-x}Co_x)_2As_2$ ($x = 0, 0.075$) where we combine low energy electron diffraction (LEED), scanning tunneling microscopy and spectroscopy (STM/S), and DFT calculations to address the coupling between spin, charge and lattice at the (1×2) surface of Ca122 [128]. The Ca122 surface was chosen for this study because it is predominantly (1×2) and simpler than its sister compound Ba122 [131]. We first use LEED intensity (I) versus voltage (V) (I-V) analysis to determine that the (1×2) reconstructed surface is a half monolayer (50%) Ca with a large inward relaxation (∼0.5 Å), and with a significant buckling in the underneath As-Fe_2-As layer. Then, spin-dependent DFT calculations are performed to demonstrate that the surface lattice structure is reproduced if and only if the surface possesses bulk AFM ordering. A superconducting gap is found at this reconstructed surface by STS, presumably as the consequence of the proximity to superconductivity in the bulk.

9.2 Experimental and theoretical methods

Single crystals of $Ca(Fe_{1-x}Co_x)_2As_2$ ($x = 0, 0.075$) were grown out of Sn flux [140]. Magnetic susceptibility and electrical resistivity measurements show the bulk magnetic/structural transition temperature is TN/S∼170 K for $x = 0$. For the $x = 0.075$ compound, the bulk TN∼90 K while TS∼100 K. Superconductivity occurs at T_c 19 K (bulk). STM/S measurements were carried out at 85 K, 20 K, 16 K, and 7.4 K with a home-built variable temperature STM [141] with a tungsten tip at 85 K and Pt/Ir tip at 20 K, 16 K and 7.4 K. For LEED experiments, the sample position was adjusted to achieve normal incidence for the primary electron beam. The LEED patterns were recorded at 85 K over a beam energy range of 40 eV to 400 eV by a CCD camera with a LabView interface. LEED I-V patterns were collected right after the fresh cleave at 85 K.

Plane-wave DFT calculations were performed using the VASP package [36, 37] within the generalized gradient approximation using the Perdew-Burke-Ernzerhof xc function [31]. Projector augmented wave pseudo-potentials were used with a 400 eV energy cutoff. Sampling in the Brillouin zone was (16×16×8) for the bulk and (8×8×1) for the (1×2) surface structure within the Monkhorst-Pack scheme [38]. For the bulk, both

atom positions and cell dimensions were relaxed until the residual forces are all lower than 0.02 eV/Å. Then two optimized bulk unit cells [see the inset of Fig. 9.1(a)] were taken along the c-axis direction to model the surface in the repeated slab model with a vacuum spacing of 14 Å. The surface was relaxed with in-plane lattice parameters fixed to the bulk ones until all the residual forces are lower than 0.04 eV/Å. For spin-polarized calculations, both the lattice and magnetic moments were determined self-consistently to minimize the total energy, starting with a number of different initial spin orderings.

9.3 Results and discussions

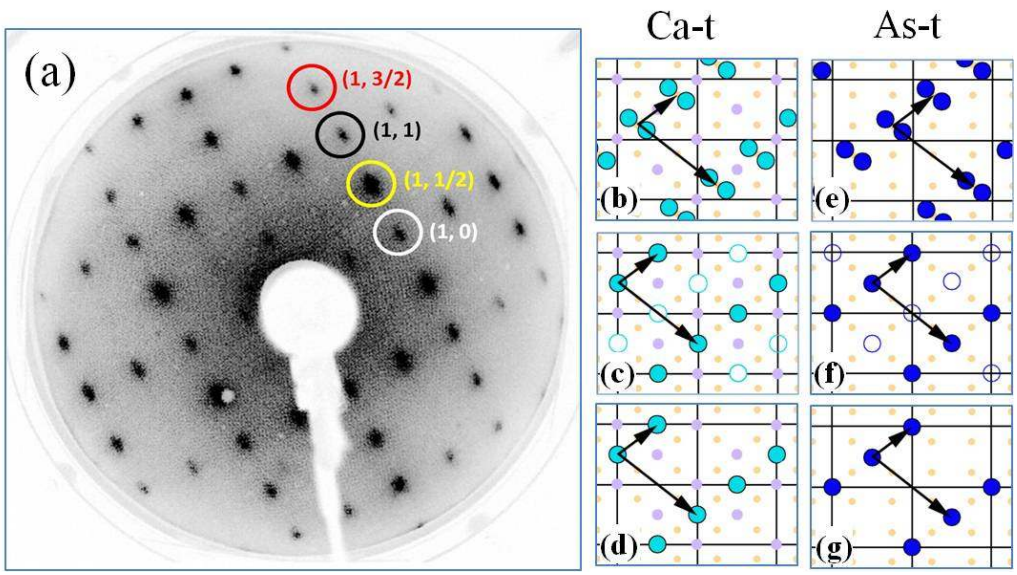

Figure 9.2: (a) LEED pattern on the surface of $CaFe_2As_2$ (120 eV); (b-g): Six possible structural models for the stripe (1×2) phase for Ca- or As- termination.

Fig. 9.1(a) shows the phase diagram of $Ca(Fe_{1-x}Co_x)_2As_2$ [135], and the Ort-AFM structure in the inset. There are two atoms in each Ca and As plane, and four in the Fe plane in a unit cell. Unfortunately, the symmetric STM images cannot resolve the small distortion ($a \neq b$) induced by the bulk orthorhombicity [$(a-b)/(a+b) \sim 0.5\%$] [142] and we therefore used the tetragonal unit cell. The STM image in Fig. 9.1(b) only shows rows of atoms (stripes) with a spacing of ∼8 Å, which is about twice the tetragonal lattice constant (∼4 Å). STM performed at 4.2 K has been previously reported to resolve the atoms in each row [143]. Surface twin domains are observed as perpendicular stripes by

STM (not shown).

Fig. 9.2(a) shows a typical LEED pattern on the surface of $CaFe_2As_2$ obtained at 120 eV. The integer spots [(1,0) and (1,1)], and the fractional spots [(1,1/2) and (1,3/2)] are indicated by colored circles. Fractional spots are present in both directions because of twin domains. We find that the fractional spots are fragile and their existence and sharpness are sensitive to temperature, vacuum, thermal process, and the beam energy, in similitude to doped Ba122 compounds [144]. Thus, extra care has been taken to record the best LEED I-V data in a time period as short as possible, following the fresh cleave at 85 K.

When analyzing the surface structure, we assume that the termination layer cannot be Fe, because of its strong bonding with As. Figs. 9.2(b-g) show six structural models of Ca- and As-termination. All of these six models have the same (1×2) unit cell, as seen by LEED and STM. Nine (1×2) fractional I-V beams with a total energy range 1224 eV are used to determine the optimal structure. The Pendry Rp factor is used to quantify the goodness of the fit between the calculated and measured I-V curves [145]. The Rp values achieved on the optimized structures and Debye temperatures for the six different models of the surface of $CaFe_2As_2$ are: 0.8 for a full-As dimer [Fig. 9.2(e)], 0.6 for a full-As rumple [Fig. 9.2(f)], 0.8 for a half-As [Fig. 9.2(g)], 0.8 for full-Ca dimer [Fig. 9.2(b)], 0.6 for full-Ca rumple [Fig. 9.2(c)], and 0.23 for half-Ca [Fig. 9.2(d)]). The half-monolayer-Ca model is therefore the only acceptable one. Table 9.1 lists the experimentally determined displacements, and our LEED I-V structure analysis on $x = 0.075$ compound for comparison.

The preference for half-monolayer Ca terminated model is not surprising: it is the most intuitive model and also has the lowest DFT energy [146]. What is surprising is the consequence of the surface reconstruction: Ca atoms at the surface are pulled down (inward relaxation) by $\sim$0.5 Å as shown in Fig. 9.3(a). Even more startling is the rippling in the As-Fe_2-As triple layer just below the surface Ca plane: the Fe atoms (Fe1) between the Ca rows move up by $\sim$0.1 Å compared to the position of this plane for the bulk structure or the position of Fe3 atoms. The displacements of other surface Fe atoms (Fe2 & Fe3) are less than 0.05 Å, which is comparable to the experimental error bar (see Table 9.1). The Rp value is very sensitive to the vertical motion of Ca and Fe1 atoms,

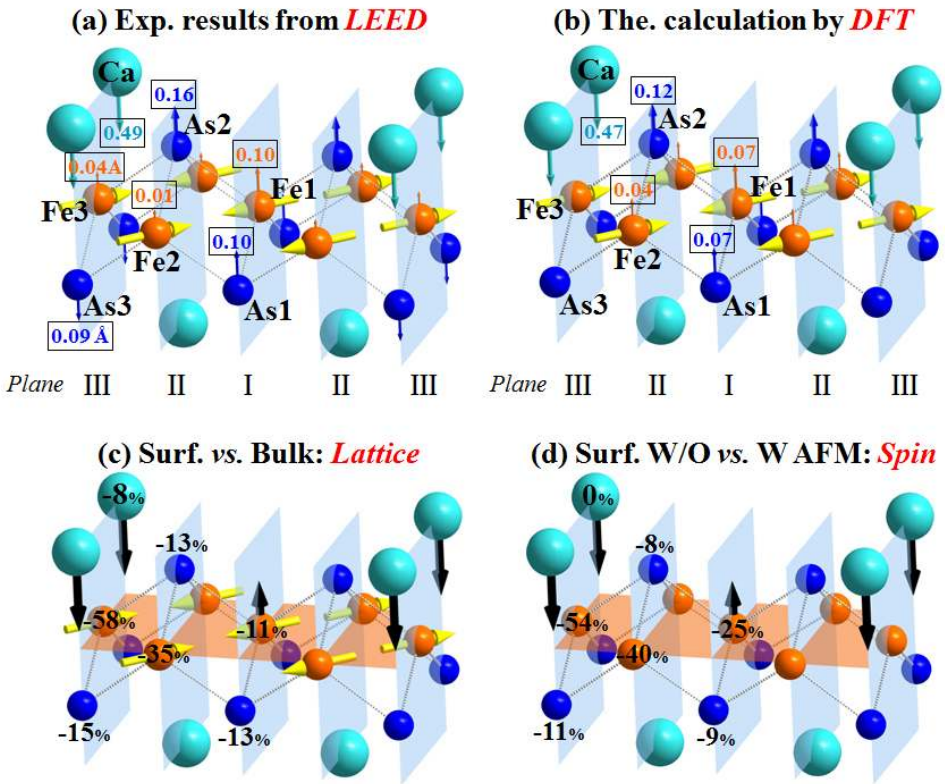

Figure 9.3: (a) Surface structure determined by LEED I-V analysis; (b) DFT calculated structure with AFM ordering identical to bulk; (c) Bader charge difference between surface and bulk atoms both with AFM ordering. The yellow arrows represent spins while the black arrows indicate the distortion with respect to the bulk; (d) Bader charge difference of surface atoms with (W) and without (W/O) AFM ordering.

yielding small error bars. The rippling in the Fe plane seems to be accompanied by similar distortion in the As planes (see Table 9.1). The Fe and As atoms are labeled according to their respective planes, with Fe1 and As1 in plane I, Fe2 and As2 in plane II, and Fe3 and As3 in plane III as shown in Figs. 9.3(a) and 9.3(b).

To examine the origin of this reconstruction, we perform spin-dependent DFT calculations and found that the surface with the bulk AFM ordering [spins ferromagnetically (FM) coupled along b axis and anti-ferromagnetically coupled along a & c axes in Fig. 9.1(a)] has the lowest energy and reproduces the structure as determined by experiment. Here are four important findings. First, if no spin ordering is included, the surface has only a 0.38 Å inward relaxation. Second, when FM ordering is considered, the self-consistent magnetic moment goes to zero, and the structure becomes the collapsed tetragonal phase. Third, among six different AFM orders, we can produce a 0.47

Table 9.1: Details of stripe (1×2) surface structures of Ca122 and 7.5% Co-doped Ca122.

Labels	$Ca(Fe_{1-x}Co_x)_2As_2$(x = 0.0, 0.075) (Å)				
	Bulk Exp.	Bulk DFT	Surface LEED $x = 0$	Surface LEED $x = 0.075$	Surface DFT
Ca	0.0000	0.000	**+0.49 (±0.04)**	**+0.54 (±0.03)**	**+0.474**
As2	1.5583	1.538	-0.16 (±0.26)	-0.04 (±0.23)	-0.118
Fe1	2.9160	2.851	**-0.10 (±0.05)**	**-0.07 (±0.04)**	
Fe2	2.9160	2.851	-0.01(±0.10)	+0.08 (±0.13)	**-0.073**
Fe3	2.9160	2.851	+0.04 (±0.06)	+0.11 (±0.05)	-0.043
As1	4.2737	4.160	-0.11 (±0.10)	-0.04 (±0.06)	
As3	4.2737	4.160	+0.10 (±0.10)	+0.11 (±0.05)	+0.004
					-0.072
Ca	5.8320	5.698	0.00	0.00	-0.008
					+0.000

Å surface relaxation if and only if the surface has the same AFM ordering as the bulk [Fig. 9.3(b)]. Within error bar, this is identical to the experimental inward motion of ∼0.5 Å [Fig. 9.3(a)]. Finally, theory reproduces the buckling of the center Fe1 atom. These results confirm that the topmost Fe layer in the (1×2) orthorhombic $CaFe_2As_2$ surface structure has an AFM ordering similar to the bulk. In other words, the striped (1×2) surface structure with top Ca layer ∼0.5 Å relaxation is the signature of a specific AFM ordering.

Since the spin-dependent DFT calculations reproduce the observed surface structure with bulk AFM ordering, they can be used to further understand the interplay between spin, charge, and lattice associated with the surface relaxation. The formal valences in Ca122 are Ca^{2+}, Fe^{2+}, and As^{3-}. Fig. 9.3(c) and Table 9.2 show the calculated change in the atomic Bader charge [147] on the surface compared to the equivalent atoms in the bulk. Overall, the surface becomes more neutral (i.e., less ionic) than the bulk. For example, the surface Ca atoms, which are pulled down ∼0.5 Å, become 8% less positively charged (+1.43e in the bulk to +1.31e at the surface), and the Fe3 atom becomes ∼58% less positive (+0.31e in the bulk to +0.13e at the surface). On average, the charge on the Fe layer (the third layer) is ∼34% less positive than its bulk counterpart. The charge rearrangement is also present in the second and forth As layers, all becoming 13%-15%

less negative. These changes in the charge distribution are the obvious manifestations of the surface reconstruction. We also calculated the effect of spin ordering on the charge distribution by setting magnetic moment to zero (NM) and keeping the orthorhombic structure. Fig. 9.3(d) and Table 9.2 show that there is significant charge redistribution on the Ort-NM surface compared to the Ort-AFM case. The negatively charged As atoms become less negative and the positively charged Fe atoms become less positive. The removal of spin ordering reduces electronic charge transfer from Fe atoms to As atoms. As Table 9.2 shows, this charge redistribution is more dramatic in the bulk than at the surface. Such charge redistribution driven by the loss of spin ordering is what drives the system into the collapsed tetragonal phase in the bulk.

Table 9.2: Bader charges for orthorhombic Ca122 surface and bulk with or without including the AFM spin ordering. See Ref. [147] for details regarding Bader charges.

DFT		Ca1	As2	Fe1	Fe2	Fe3	As1	As3
Ort-AFM	Bulk	+1.43	-0.99	+0.31	+0.31	+0.31	-1.06	-1.05
	Surface	+1.31	-0.86	+0.28	+0.2	+0.13	-0.92	-0.89
Diff. Surface-Bulk		-0.12	+0.13	-0.03	-0.11	-0.18	+0.14	+0.16
Ort-NM	Bulk	+1.39	-0.79	+0.14	+0.14	+0.14	-0.88	-0.88
	Surface	+1.31	-0.79	+0.21	+0.12	+0.06	-0.84	-0.79
Diff. NM-AFM at bulk		-0.04	+0.2	-0.17	-0.17	-0.17	+0.18	+0.17
Diff. NM-AFM at surf.		0.00	+0.07	-0.07	-0.08	-0.07	+0.08	+0.10

It was previously observed that the surface reconstruction could suppress superconductivity, making STS unable to probe the superconducting gap [148]. However, the surface reconstruction of Ca122 does not result in a similar consequence, and we see the signature of a SC gap below T_c of $Ca(Fe_{0.925}Co_{0.075})_2As_2$. Fig. 9.4(a) shows the averaged STS taken from the clean (1×2) surface [Figs. 9.4(b) and 9.4(c)] of $Ca(Fe_{0.925}Co_{0.075})_2As_2$ at 20 K, 16 K and 7.4 K, respectively. There is no gap feature down to 16 K, indicating that the transition temperature at the surface is lower than that in the bulk. However, double coherence peaks are seen at 7.4 K, due to the SC gap $\Delta \sim 7.5$ meV. The obvious interpretation that superconductivity coexists with anti-ferromagnetic ordering at the (1×2) surface presents two glaring issues. First, our structural determination is performed at 80 K, and could be different at temperatures below T_c. Second, there is a large zero-bias

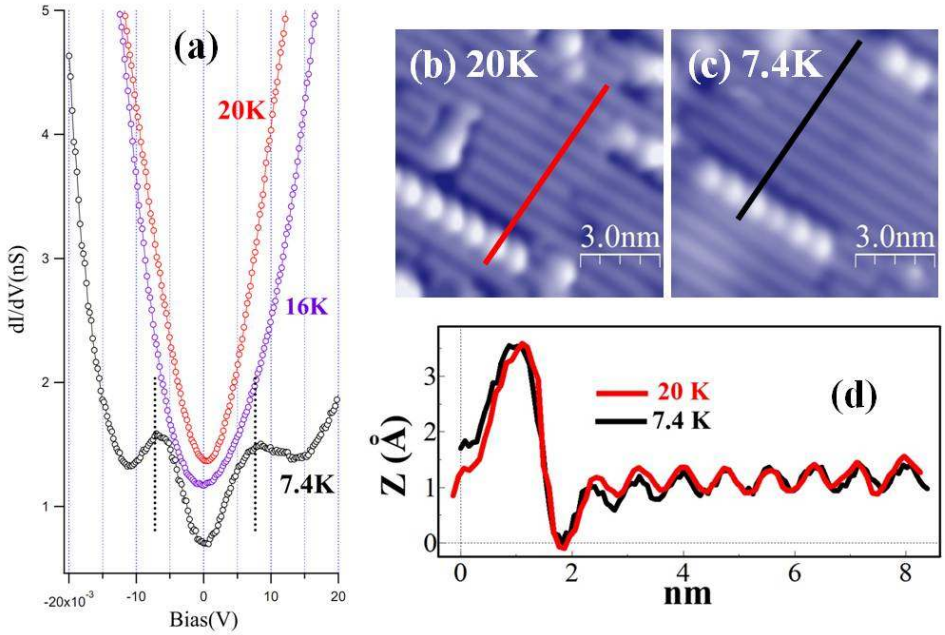

Figure 9.4: (a) Averaged STS taken from the clean stripe (1×2) surface of $Ca(Fe_{0.925}Co_{0.075})_2As_2$ at the indicated temperatures; (b) & (c) STM topographic images taken at 20 K and 7.4 K, respectively (V_{bias} = 1.0 V, I_t = 200 pA). The profiles along indicated lines in (b) and (c) are shown in (d).

conductance, nearly half of that at the coherence peak.

To resolve the first issue, we need to understand what happens in the bulk. According to neutron scattering measurements, there is no structural or magnetic moment change when crossing T_c of Ca122 [149]. At the surface, our STM topographies taken with the same tip and the same tunneling junction show no change of the atomic corrugation and surface adatom (bright protrusion) height above and below T_c [Figs. 9.4(b-d)]. As demonstrated in Fig. 9.3, any change in lattice structure and/or magnetic ordering would result in large charge redistribution. The unchanged atomic corrugation in STM images across T_c is consistent with neutron scattering results, confirming the absence of lattice structure and spin ordering below T_c.

Zero-bias conductance was previously observed on the (1×2) surface of Ca122 with superconductivity induced by partial substitution of Ca using La [150]. If the tunneling spectra shown in Fig. 9.4(a) were from a tunnel junction measurement, the interpretation would be obvious: superconducting region (with gap) coexisting with non-superconducting region (with finite zero-bias conductance). However, the STS measure-

ment is spatially resolved (in plane) on a scale much smaller than the coherence length or the domain size. If the measurement is sampling an inhomogeneous material, it has to be in the direction perpendicular to the surface. For Ca122, STS may have contribution from the reconstructed surface that tends to be a normal metal and the bulk which is superconducting. The latter penetrates to the surface via the proximity effect, thus revealing superconducting gap feature (e.g. coherence peaks in STS). This is consistent with our observation that the gap feature in STS disappears at 16 K [Fig. 9.4(a)], lower than the bulk T_c, very similar to STM/S observation of the proximity effect on heterogeneous superconducting thin films on metallic substrates [151]. This can explain the observed variation of the zero-bias conductance for different reconstructed phases of A122 system.

9.4 Summary

In this chapter, our experimental collaborators have carried out LEED I-V analysis to identify the stripe-ordered phase seen at the surface of $Ca(Fe_{1-x}Co_x)_2As_2$ ($x = 0, 0.075$). The surface consists of half-Ca layer with a (1×2) structure. These surface Ca atoms move inward $\sim$0.5 Å and the surface As-Fe_2-As layer is buckled. DFT calculations show that the (1×2) phase is stabilized by the bulk anti-ferromagnetic ordering through the spin-charge-lattice coupling. Furthermore, STS measurements show the presence of a superconducting gap on the ordered (1×2) surface, while the spectra always have a finite zero-bias conductance. These observations result from a combination of the reconstructed surface, which tends to be both AFM ordered and superconducting due to the proximity to the superconducting bulk. The surface-stabilized coexistence of superconductivity and AFM ordering raises the prospect of growing artificial structured materials with this property.

10. Conclusions and perspectives

10.1 Conclusions

The thesis is concluded here by presenting a summary of the findings made during the course of the graduate research. After listing the computational methods used and developed in this thesis (Chapter 1), we begin to present our results, which are divided into three parts: graphene nanowiggles, transition metal dichalcogenides and Fe-based superconductors.

In Part I, low-dimensional carbon-based nanomaterials, graphene and graphene nanoribbons (GNRs), have attracted much attention due to their extraordinary electrical, optical, thermal and mechanical properties (Chapter 2). The rich properties of graphene have made it one of the most promising candidates to replace silicon technology. However, the gapless feature of pristine graphene limits its applicability in semiconductors industry. A band gap can be opened for GNRs due to quantum confinement effects, offering a solution for graphene-based applications. To have a band gap comparable to conventional semiconductors like silicon, GNRs are required to have a width less than 3 nm with clean edges, which remains a great experimental challenge. Recently, major experimental advance was made with an atomically precise bottom-up approach to chemically assemble small aromatic molecules into high-quality subnanometer ribbons including the novel graphene nanowiggles (GNWs).

Then Chapter 3 is dedicated to a thorough study on electronic and magnetic properties of a variety of GNWs in a combination of first-principles density functional theory (DFT) and many-body Green's function approach within the *GW* approximation. Our study reveals their unusual electro-magnetic properties that are absent in their constitutive GNRs, such as tunable band gaps and versatile magnetic states. The emergence of these properties is the result of the interplay between the properties of the GNR constituents, the symmetry of the atomic structure, and the bipartition of the graphene lattice. The relationship between the band gap and the geometry is dictated by the armchair or zigzag characters of the corresponding parallel and oblique sectors, enabling GNWs to offer a broader set of geometrical parameters to tune the electronic structures compared

to GNRs. All GNWs with at least one zigzag sector have an AFM ground state. More importantly, a number of new metastable spin distributions are found due to GNWs' unique wiggle-like edges. For instance, the existence of versatile magnetic states in the AZ GNW (7_A,4_Z) enables its quasiparticle band gap to be tuned from 0.56 to 1.46 eV, the ideal band gap range for semiconductor devices, thereby demonstrating GNWs' potential for nanoelectronic and spintronic applications. Finally, we have developed a less computational demanding tight-binding+Hubbard (TBU) model that can capture the most relevant physical aspects of electronic and magnetic properties of GNWs. A systematic study was performed using TBU, showing that each achiral GNW type has a specific map for the band gap as a function of the widths of both parallel and oblique sectors.

In Chapter 4, GNWs are also found by DFT calculations to possess significantly enhanced thermoelectric performance compared to their straight GNRs counterparts. Such improvement originates from the combination of (i) reduced phonon thermal conductance due to phonon scattering by wiggle-like edges and the mismatch of phonon modes in the parallel and oblique sectors, and (ii) the electron resonant tunneling effect between these sectors which guarantee good electronic conduction. In general, peak ZT values of AA GNWs are more than triple those of straight AGNRs of the same width. For many GNWs with at least one zigzag sector, the interplay between parallel and oblique sectors opens a band gap, leading to larger thermopower and consequently to higher ZT while peak ZT values of straight ZGNRs are almost zero due to their metallicity. A larger proportion of AA systems possess ZT higher than 0.5 in comparison to the other three types of achiral GNWs, leading to the conclusion that the experimentally available AA GNWs are the most promising candidates for thermoelectric applications. We also used a combination of TBU and density-functional based tight binding method (DFTB+) to conduct a systematic study to show the relationship of peak ZT and structural parameters for each GNW type. The highest ZT at room temperature for pristine GNWs is found to be 0.79. However, for practical thermoelectric applications, a system should have ZT higher than 1. Our DFT calculations show that a certain pattern of structural dislocation in the experimentally available GNW (9_A,6_A) can make ZT exceed 1 at room temperature by further reducing the thermal conductance of the GNW.

Note that the aforementioned electronic, magnetic and thermal properties are found

for free-standing GNWs. In reality, however, these structures are synthesized on a gold substrate. Thus, Chapter 5 is devoted to an investigation of the influence of the gold substrate on electronic properties of the experimentally fabricated GNR (AGNR-7) and GNW (9_A,6_A). DFT calculations found that both GNR and GNW are weakly adsorbed on the Au(111) surface by the van der Waals (vdW) force with separation distances larger than 3.0 Å. There is a small net charge transfer from GNW (GNR) to the substrate, resulting in a *p*-type doping of GNW (GNR). Such charge transfer gives rise to an electric dipole at the interface, leading to substrate polarization and subsequently a band gap reduction of the adsorbed GNW (GNR). A semi-empirical image charge model was developed to give satisfactory estimation of band gap reductions, consistent with experimental values. Since the gold substrate can have significant influence on electronic properties of GNWs, it is essential to find out how the substrate affects their magnetic properties. In Chapter 5, to verify the robustness of spin states of GNWs on the gold substrate, we choose the AZ GNW (7_A,4_Z) supported on the Au(111) surface as a case study. Our spin-polarized DFT calculations indicate that the gold substrate only interacts with (7_A,4_Z) by weak physical forces. Subsequently, the spin orderings of (7_A,4_Z) do not significantly vary in the presence of the gold substrate.

Now, we have studied pure GNWs. Recently, nitrogen atoms have been doped to GNWs and heterojunctions consisting of pure and nitrogen-doped GNWs (p-GNWs and N-GNWs) have been synthesized. In the final chapter of Part I (i.e., Chapter 6), we have considered two types of experimentally realized nitrogen doping in the GNW (9_A,6_A) and denoted them as N2 and N4. The corresponding GNW heterojunctions are then labeled as the p-N2-GNW and p-N4-GNW heterojunctions, respectively. NEGF-DFT computational method has been used to investigate their electronic and transport properties. Nitrogen doping in the GNW (9_A,6_A) is found to shift down the Fermi level without significantly change the electronic band gap, thus resulting in a type-II band alignment at the heterojunction interface. The band alignment subsequently reduces the electronic band gap of the heterojunction while increases its transport gap. More interestingly, as the nitrogen doping concentration increases, both the conduction and valence band offsets (ΔE_c and ΔE_v) at the interface increase almost linearly. Hence, the highly-controllable (at the atomic level) nitrogen doping technique not only enables the fabrication of atomic-

precise and defect-free p-N-GNW heterojunctions with type-II band alignments, but also offers a unique approach to engineer the interface band offsets of heterojunctions. The recently synthesized p-N4-GNW heterojunction is estimated to have a maximum power conversion efficiency of 11.3% as an excitonic solar cell, and hence is very promising for future solar cell applications.

In Part II, we turn our attention to graphene-like materials: transition metal dichalcogenides MX_2 (M = Mo, W; X = S). Similar to graphite and h-BN, they are also layered structures stacked by weak vdW forces. Single-layer MoS_2 and WS_2 have been synthesized and found to show enhanced carrier charge mobilities and strong photoluminescence with direct band gaps, and thus they have been considered as replacements or complements to graphene for future applications. Raman spectroscopy is a very powerful nondestructive characterization tool used extensively to study them. Despite the extensive experimental Raman study on MoS_2 and WS_2, it remains unclear how Raman intensities and especially intensity ratio of Raman modes E^1_{2g} and A_{1g} depend on the materials thickness, due to the large spectrum of seemingly contradictory findings (Chapter 7).

To clarify such issues, in Chapter 8, we perform a comprehensive first-principles study of Raman scattering of both MoS_2 and WS_2. Our calculations successfully reproduce the experimentally observed continuous downshift of E^1_{2g} mode and upshift of A_{1g} mode with increasing thickness. The increasing dielectric screening (interlayer coupling) is found to be responsible for downshift of E^1_{2g} (upshift of A_{1g}) with increasing thickness. Our calculations also reveal the intrinsic thickness dependence of Raman intensities and intensity ratio. More importantly, we quantitatively analyze the laser polarization effect on the intensity ratio and reveal the high sensitivity of the intensity ratio to laser polarization. The intensity ratio can be essentially tuned from 0 to infinity by adjusting laser polarization, which could be the key to explaining the large discrepancy between measured intensity ratios by different experimental groups where different laser polarization set-ups might be used.

In Chapter 8, we also study *ab initio* Raman spectra of MoS_2/WS_2 heterostructures up to four layers in every possible combinations and stacking orders. Each heterostructure configuration is found to possess a unique Raman spectrum in both frequency and intensity that can be explained by changes in dielectric screening and interlayer interactions.

The results establish a set of guidelines that can be used for the practical experimental identification of heterostructure configurations.

In the final part of the thesis, Part III, we highlight the experimental collaboration project with Prof. Plummer's group from Louisiana State University: surface reconstruction of layered Fe-based superconductors $CaFe_2As_2$. In Chapter 9, our experimental collaborators have carried out low energy electron diffraction (LEED) I-V analysis to identify the stripe-ordered phase seen at the surface of $Ca(Fe_{1-x}Co_x)_2As_2$ ($x = 0, 0.075$). The surface consists of half-Ca layer with a (1×2) structure. These surface Ca atoms move inward $\sim$0.5 Å and the surface As-Fe_2-As layer is buckled. Spin-dependent DFT calculations show that the (1×2) phase is stabilized by the bulk anti-ferromagnetic ordering through the spin-charge-lattice coupling. Furthermore, scanning tunneling spectroscopy (STS) measurements show the presence of a superconducting gap on the ordered (1×2) surface, while the spectra always have a finite zero-bias conductance. These observations result from a combination of the reconstructed surface, which tends to be both AFM ordered and superconducting due to the proximity to the superconducting bulk. The surface-stabilized coexistence of superconductivity and AFM ordering raises the prospect of growing artificial structured materials with this property.

10.2 Perspectives

While we have a good collection of promising results in this thesis, there are still a lot of interesting problems to be explored in the future. A non-exhaustive list of ongoing projects are presented below.

As mentioned in Chapter 6 of Part I, two types of nitrogen doping have been experimentally realized in the GNW (9_A,6_A): N2 and N4. We have investigated the electronic and transport properties of p-N2-GNW and p-N4-GNW heterojunctions, which show the type-II band alignments for excitonic solar cell applications. To further explore doping effects in GNWs, we currently use both DFT and more accurate many-body *GW* approach to systematically study both boron and nitrogen doping with various concentrations in four armchair-armchair GNWs. The GNWs under investigation include (9_A,6_A), (8_A,6_A), (8_A,5_A) and (6_A,5_A). The doping concentrations considered include N1-N5 and B1-B5. For all four GNWs, the increasing B/N doping concentrations affect little the magnitude

of band gaps but almost linearly shift up/down them, leading to type-II staggered band alignments in GNWs heterojunctions with tunable band gaps and band offsets. More importantly, the proposed (8_A,5_A) p-B1-GNW heterojunction is predicted to have maximum power conversion efficiencies 22.0% as an excitonic solar cell. These interesting results are expected to stimulate further efforts to realize GNWs with a variety of sizes and doping concentrations for applications in photovoltaics and electronics.

In Chapter 8 of Part II, a theoretical model of non-resonant first-order Raman scattering is developed and adopted to study Raman spectra of MoS_2, WS_2 and their heterostructures. The possession of such Raman tool enables us to explore in a barely touched ground. In the near future, we plan to further study defect and stain effects on Raman scattering of MoS_2 and WS_2. Or we can study other transition metal dichalcogenides such as $MoSe_2$, $MoTe_2$, WSe_2, etc. Recently, two-dimensional Si and Ge with graphene-like hexagonal lattices, so called silicene and germanene, have been extensively studied. Their hydrogenated and fluorinated products are also very interesting. Raman spectroscopy can be used to monitor their hydrogenation and fluorination, and hence we are currently working on theoretical Raman scattering of hydrogenated and fluorinated graphene, silicene and germanene in attempt to guide the experimental characterization of them.

In Chapter 9 of Part III, spin-dependent surface reconstruction of layered Fe-based superconductors $CaFe_2As_2$ has been probed. Now, we are studying another superconductor $BaFe_2As_2$, which also shows similar spin-dependent surface reconstruction. The (1×2) surface phase of $BaFe_2As_2$ is also stabilized by the bulk anti-ferromagnetic ordering through the spin-charge-lattice coupling. Moreover, we have calculated work functions for a variety of surfaces of $CaFe_2As_2$ such as the orthorhombic/tetragonal surfaces with 1 ML, 1/2 ML and 0 ML Ca to help experimental identification of these surfaces. We will start the computation of work functions for various surfaces of $BaFe_2As_2$ soon.

REFERENCE

[1] E. C. Girão, Ph.D. thesis, Federal University of Ceará, 2011.

[2] A. Bostwick, J. McChesney, T. Ohta, E. Rotenberg, T. Seyller, and K. Horn, Prog. Surf. Sci. **84**, 380 (2009).

[3] K. Novoselov, A. Geim, S. Morozov, D. Jiang, Y. Zhang, S. Dubonos, I. Grigorieva, and A. Firsov, Science **306**, 666 (2004).

[4] A. Geim and K. Novoselov, Nat. Mater. **6**, 183 (2007).

[5] K. Wakabayashi, Y. Takane, and M. Sigrist, Phys. Rev. Lett. **99**, 36601 (2007).

[6] Y. Zhang, Y. Tan, H. Stormer, and P. Kim, Nature **438**, 201 (2005).

[7] X. Xu, N. Gabor, J. Alden, A. van der Zande, and P. McEuen, Nano Lett. **10**, 562 (2009).

[8] R. Nair, P. Blake, A. Grigorenko, K. Novoselov, T. Booth, T. Stauber, N. Peres, and A. Geim, Science **320**, 1308 (2008).

[9] J. Seol, I. Jo, A. Moore, L. Lindsay, Z. Aitken, M. Pettes, X. Li, Z. Yao, R. Huang, D. Broido, N. Mingo, R. Ruoff, and L. Shi, Science **328**, 213 (2010).

[10] A. A. Balandin, S. Ghosh, W. Bao, I. Calizo, D. Teweldebrhan, F. Miao, and C. N. Lau, Nano Lett. **8**, 902 (2008).

[11] C. Lee, X. Wei, J. Kysar, and J. Hone, Science **321**, 385 (2008).

[12] C. Palma and P. Samorì, Nature Chem. **3**, 431 (2011).

[13] D. Dragoman and M. Dragoman, Appl. Phys. Lett. **91**, 203116 (2007).

[14] F. Xia, V. Perebeinos, Y. Lin, Y. Wu, and P. Avouris, Nature Nanotech. **6**, 179 (2011).

[15] F. Schwierz, Nature Nanotech. **5**, 487 (2010).

[16] D. Elias, R. Nair, T. Mohiuddin, S. Morozov, P. Blake, M. Halsall, A. Ferrari, D. Boukhvalov, M. Katsnelson, A. Geim, and K. Novoselov, Science **323**, 610 (2009).

[17] X. Li, X. Wang, L. Zhang, S. Lee, and H. Dai, Science **319**, 1229 (2008).

[18] Y. Son, M. Cohen, and S. Louie, Phys. Rev. Lett. **97**, 216803 (2006).

[19] O. Yazyev, Rep. Prog. Phys. **73**, 056501 (2010).

[20] Y. Son, M. Cohen, and S. Louie, Nature **444**, 347 (2006).

[21] J. Cai, P. Ruffieux, R. Jaafar, M. Bieri, T. Braun, S. Blankenburg, M. Muoth, A. Seitsonen, M. Saleh, X. Feng, K. Mullen, and R. Fasel, Nature **466**, 470 (2010).

[22] C. Bronner, S. Stremlau, M. Gille, F. Brauße, A. Haase, S. Hecht, and P. Tegeder, Angew. Chem. Int. Ed. **52**, 4422 (2013).

[23] X. Jia, J. Campos-Delgado, M. Terrones, V. Meunier, and M. Dresselhaus, Nanoscale **3**, 86 (2011).

[24] J. Cai, C. A. Pignedoli, L. Talirz, D. Passerone, P. Ruffieux, J. Liu, H. Sode, L. Liang, V. Meunier, R. Berger, X. Feng, K. Mullen, and R. Fasel (unpublished).

[25] E. C. Girão, L. Liang, E. Cruz-Silva, A. Filho, and V. Meunier, Phys. Rev. Lett. **107**, 135501 (2011).

[26] E. C. Girão, E. Cruz-Silva, L. Liang, A. Souza Filho, and V. Meunier, Phys. Rev. B **85**, 235431 (2012).

[27] L. Liang, E. C. Girão, and V. Meunier, Phys. Rev. B **88**, 035420 (2013).

[28] P. Hohenberg and W. Kohn, Phys. Rev. B **136**, B864 (1964).

[29] W. Kohn and L. J. Sham, Phys. Rev. **140**, 1133 (1965).

[30] J. P. Perdew and Y. Wang, Phys. Rev. B **45**, 13244 (1992).

[31] J. Perdew, K. Burke, and M. Ernzerhof, Phys. Rev. Lett. **77**, 3865 (1996).

[32] V. Fock, Zeitschrift für Physik **61**, 126 (1930).

[33] A. D. Becke, J. Chem. Phys. **98**, 5648 (1993).

[34] C. Lee, W. Yang, and R. G. Parr, Phys. Rev. B **37**, 785 (1988).

[35] J. Heyd, G. E. Scuseria, and M. Ernzerhof, J. Chem. Phys. **118**, 8207 (2003).

[36] G. Kresse and J. Furthmüller, Comput. Mat. Sci. **6**, 15 (1996).

[37] G. Kresse and J. Furthmüller, Phys. Rev. B **54**, 11169 (1996).

[38] H. J. Monkhorst and J. D. Pack, Phys. Rev. B **13**, 5188 (1976).

[39] E. C. Girão, L. Liang, J. Owens, E. Cruz-Silva, B. G. Sumpter, and V. Meunier, *Graphene Chemistry* (John Wiley & Sons, Ltd, 2013) Chap. 14, pp. 319–346.

[40] D. Gunlycke and C. White, Phys. Rev. B **77**, 115116 (2008).

[41] C. Friedrich and A. Schindlmayr, NIC Series **31**, 335 (2006).

[42] K. Thygesen and A. Rubio, Phys. Rev. Lett. **102**, 046802 (2009).

[43] M. Shishkin and G. Kresse, Phys. Rev. B **75**, 235102 (2007).

[44] L. Yang, C. Park, Y. Son, M. Cohen, and S. Louie, Phys. Rev. Lett. **99**, 186801 (2007).

[45] S. Wang and J. Wang, J. Phys. Chem. C **116**, 10193 (2012).

[46] L. Liang, E. Cruz-Silva, E. C. Girão, and V. Meunier, Phys. Rev. B **86**, 115438 (2012).

[47] L. Liang and V. Meunier, Appl. Phys. Lett. **102**, 143101 (2013).

[48] L. Bell, Science **321**, 1457 (2008).

[49] C. Vining, Nat. Mater. **8**, 83 (2009).

[50] M. Dresselhaus, G. Chen, M. Tang, R. Yang, H. Lee, D. Wang, Z. Ren, J. Fleurial, and P. Gogna, Adv. Mater. **19**, 1043 (2007).

[51] T. Gunst, T. Markussen, A. Jauho, and M. Brandbyge, Phys. Rev. B **84**, 155449 (2011).

[52] K. Saha, T. Markussen, K. Thygesen, and B. Nikolić, Phys. Rev. B **84**, 041412 (2011).

[53] F. Mazzamuto, V. Nguyen, Y. Apertet, C. Caër, C. Chassat, J. Saint-Martin, and P. Dollfus, Phys. Rev. B **83**, 235426 (2011).

[54] W. Huang, J. Wang, and G. Liang, Phys. Rev. B **84**, 045410 (2011).

[55] Y. Chen, T. Jayasekera, A. Calzolari, K. Kim, and M. Buongiorno Nardelli, J. Phys.: Condens. Matter **22**, 372202 (2010).

[56] N. Mingo and D. Broido, Phys. Rev. Lett. **95**, 96105 (2005).

[57] L. Rego and G. Kirczenow, Phys. Rev. Lett. **81**, 232 (1998).

[58] K. Esfarjani, M. Zebarjadi, and Y. Kawazoe, Phys. Rev. B **73**, 085406 (2006).

[59] A. Togo, F. Oba, and I. Tanaka, Phys. Rev. B **78**, 134106 (2008).

[60] D. Porezag, T. Frauenheim, T. Köhler, G. Seifert, and R. Kaschner, Phys. Rev. B **51**, 12947 (1995).

[61] H. Sevinçli and G. Cuniberti, Phys. Rev. B **81**, 113401 (2010).

[62] G. Guttman, E. Ben-Jacob, and D. Bergman, Phys. Rev. B **51**, 17758 (1995).

[63] L. Liang and V. Meunier, Phys. Rev. B **86**, 195404 (2012).

[64] N. Kharche and S. Nayak, Nano Lett. **11**, 52745278 (2011).

[65] J. Sławińska, P. Dabrowski, and I. Zasada, Phys. Rev. B **83**, 245429 (2011).

[66] S. Linden, D. Zhong, A. Timmer, N. Aghdassi, J. H. Franke, H. Zhang, X. Feng, K. Müllen, H. Fuchs, L. Chi, and H. Zacharias, Phys. Rev. Lett. **108**, 216801 (2012).

[67] G. Giovannetti, P. Khomyakov, G. Brocks, V. Karpan, J. Van den Brink, and P. Kelly, Phys. Rev. Lett. **101**, 26803 (2008).

[68] D. Andrade, R. Miwa, and G. Srivastava, Phys. Rev. B **84**, 165322 (2011).

[69] S. Grimme, J. Comput. Chem. **27**, 1787 (2006).

[70] J. Tersoff and D. Hamann, Phys. Rev. B **31**, 805 (1985).

[71] E. C. Girão, E. Cruz-Silva, and V. Meunier, ACS Nano **6**, 64836491 (2012).

[72] J. Neaton, M. Hybertsen, and S. Louie, Phys. Rev. Lett. **97**, 216405 (2006).

[73] Y. Li, D. Lu, and G. Galli, J. Chem. Theory Comput. **5**, 881 (2009).

[74] I. White, R. Godby, M. Rieger, and R. Needs, Phys. Rev. Lett. **80**, 4265 (1998).

[75] Y. Lu and J. Guo, Nano Res. **3**, 189 (2010).

[76] C. Tao, L. Jiao, O. V. Yazyev, Y.-C. Chen, J. Feng, X. Zhang, R. B. Capaz, J. M. Tour, A. Zettl, S. G. Louie, H. Dai, and M. F. Crommie, Nature Phys. **7**, 616 (2011).

[77] J. M. Soler, E. Artacho, J. D. Gale, A. García, J. Junquera, P. Ordejón, and D. Sánchez-Portal, J. Phys.Condens. Matter **14**, 2745 (2002).

[78] V. Meunier, M. B. Nardelli, J. Bernholc, T. Zacharia, and J.-C. Charlier, Appl. Phys. Lett. **81**, 5234 (2002).

[79] R. Landauer, Philos. Mag. **21**, 863 (1970).

[80] S. Datta, *Quantum Transport: Atom to Transistor* (University Press, Cambridge, 2005).

[81] F. Ferry and S. Goodnick, *Transport in nanostructures* (University Press, Cambridge, 1997).

[82] M. B. Nardelli, Phys. Rev. B **60**, 7828 (1999).

[83] M. B. Nardelli and J. Bernholc, Phys. Rev. B **60**, R16338 (1999).

[84] M. L. Sancho, J. L. Sancho, and J. Rubio, J. Phys. F: Metal Phys. **14**, 1205 (1984).

[85] M. L. Sancho, J. L. Sancho, J. L. Sancho, and J. Rubio, J. Phys. F: Metal Phys. **15**, 851 (1985).

[86] M. C. Scharber, D. Mühlbacher, M. Koppe, P. Denk, C. Waldauf, A. J. Heeger, and C. J. Brabec, Adv. Mater. **18**, 789 (2006).

[87] J. D. Servaites, M. A. Ratner, and T. J. Marks, Appl. Phys. Lett. **95**, 163302 (2009).

[88] L.-J. Zhou, Y.-F. Zhang, and L.-M. Wu, Nano Lett. **13**, 5431 (2013).

[89] M. Bernardi, M. Palummo, and J. C. Grossman, ACS Nano **6**, 10082 (2012).

[90] M. D. Perez, C. Borek, S. R. Forrest, and M. E. Thompson, J. Am. Chem. Soc. **131**, 9281 (2009).

[91] The solar spectrum is taken from the NREL website: http://rredc.nrel.gov/solar/spectra/am1.5.

[92] L. Dou, J. You, J. Yang, C.-C. Chen, Y. He, S. Murase, T. Moriarty, K. Emery, G. Li, and Y. Yang, Nat. Photonics **6**, 180 (2012).

[93] H. Choi, J.-P. Lee, S.-J. Ko, J.-W. Jung, H. Park, S. Yoo, O. Park, J.-R. Jeong, S. Park, and J. Y. Kim, Nano Lett. **13**, 2204 (2013).

[94] A. Molina-Sánchez and L. Wirtz, Phys. Rev. B **84**, 155413 (2011).

[95] B. Radisavljevic, A. Radenovic, J. Brivio, V. Giacometti, and A. Kis, Nature Nanotech **6**, 147 (2011).

[96] H. Zeng, G.-B. Liu, J. Dai, Y. Yan, B. Zhu, R. He, L. Xie, S. Xu, X. Chen, W. Yao, and X. Cui, Sci. Rep. **3**, 1608 (2013).

[97] S. Z. Butler, S. M. Hollen, L. Cao, Y. Cui, J. A. Gupta, H. R. Gutirrez, T. F. Heinz, S. S. Hong, J. Huang, A. F. Ismach, E. Johnston-Halperin, M. Kuno, V. V. Plashnitsa, R. D. Robinson, R. S. Ruoff, S. Salahuddin, J. Shan, L. Shi, M. G. Spencer, M. Terrones, W. Windl, and J. E. Goldberger, ACS Nano **7**, 2898 (2013).

[98] H. Li, Q. Zhang, C. C. R. Yap, B. K. Tay, T. H. T. Edwin, A. Olivier, and D. Baillargeat, Adv. Funct. Mater. **22**, 1385 (2012).

[99] W. Ho, J. C. Yu, J. Lin, J. Yu, and P. Li, Langmuir **20**, 5865 (2004).

[100] K. F. Mak, C. Lee, J. Hone, J. Shan, and T. F. Heinz, Phys. Rev. Lett. **105**, 136805 (2010).

[101] K. Novoselov, D. Jiang, F. Schedin, T. Booth, V. Khotkevich, S. Morozov, and A. Geim, Proc. Natl. Acad. Sci. **102**, 10451 (2005).

[102] A. Splendiani, L. Sun, Y. Zhang, T. Li, J. Kim, C.-Y. Chim, G. Galli, and F. Wang, Nano Lett. **10**, 1271 (2010).

[103] H. R. Gutierrez, N. Perea-Lopez, A. L. Elías, A. Berkdemir, B. Wang, R. Lv, F. López-Urías, V. H. Crespi, H. Terrones, and M. Terrones, Nano Lett. **13**, 3447 (2012).

[104] W. S. Yun, S. Han, S. C. Hong, I. G. Kim, and J. Lee, Phys. Rev. B **85**, 033305 (2012).

[105] C. Lee, H. Yan, L. E. Brus, T. F. Heinz, J. Hone, and S. Ryu, ACS Nano **4**, 2695 (2010).

[106] Y. Yu, C. Li, Y. Liu, L. Su, Y. Zhang, and L. Cao, Sci. Rep. **3**, 1866 (2013).

[107] Y.-H. Lee, L. Yu, H. Wang, W. Fang, X. Ling, Y. Shi, C.-T. Lin, J.-K. Huang, M.-T. Chang, C.-S. Chang, M. Dresselhaus, T. Palacios, L.-J. Li, and J. Kong, Nano Lett. **13**, 1852 (2013).

[108] N. A. Lanzillo, A. Glen Birdwell, M. Amani, F. J. Crowne, P. B. Shah, S. Najmaei, Z. Liu, P. M. Ajayan, J. Lou, M. Dubey, S. K. Nayak, and T. P. O'Regan, Appl. Phys. Lett. **103**, 093102 (2013).

[109] A. Berkdemir, H. R. Gutiérrez, A. R. Botello-Méndez, N. Perea-López, A. L. Elías, C.-I. Chia, B. Wang, V. H. Crespi, F. López-Urías, J.-C. Charlier, H. Terrones, and M. Terrones, Sci. Rep. **3**, 1755 (2013).

[110] W. Zhao, Z. Ghorannevis, K. K. Amara, J. R. Pang, M. Toh, X. Zhang, C. Kloc, P. H. Tan, and G. Eda, Nanoscale **5**, 9677 (2013).

[111] A. C. Ferrari and D. M. Basko, Nature Nanotech **8**, 235 (2013).

[112] L. Liang and V. Meunier, Nanoscale **6**, 5394 (2014).

[113] S.-L. Li, H. Miyazaki, H. Song, H. Kuramochi, S. Nakaharai, and K. Tsukagoshi, ACS Nano **6**, 7381 (2012).

[114] X. Luo, Y. Zhao, J. Zhang, Q. Xiong, and S. Y. Quek, Phys. Rev. B **88**, 075320 (2013).

[115] X. Luo, Y. Zhao, J. Zhang, M. Toh, C. Kloc, Q. Xiong, and S. Y. Quek, Phys. Rev. B **88**, 195313 (2013).

[116] G. Kresse and D. Joubert, Phys. Rev. B **59**, 1758 (1999).

[117] G. Kresse, J. Furthmüller, and J. Hafner, Europhys. Lett. **32**, 729 (1995).

[118] G. Kern, G. Kresse, and J. Hafner, Phys. Rev. B **59**, 8551 (1999).

[119] G. Giovannetti, P. Khomyakov, G. Brocks, P. Kelly, and J. van den Brink, Phys. Rev. B **76**, 073103 (2007).

[120] J. Kang, J. Li, S.-S. Li, J.-B. Xia, and L.-W. Wang, Nano Lett. **13**, 5485 (2013).

[121] P. Umari, A. Pasquarello, and A. Dal Corso, Phys. Rev. B **63**, 094305 (2001).

[122] M. Ceriotti, F. Pietrucci, and M. Bernasconi, Phys. Rev. B **73**, 104304 (2006).

[123] K. Parlinski, computer code PHONON, Krakow, Poland, 2010.

[124] K. Parlinski, Z. Li, and Y. Kawazoe, Phys. Rev. Lett. **78**, 4063 (1997).

[125] H. Terrones, F. López-Urías, and M. Terrones, Sci. Rep. **3**, 1549 (2013).

[126] C. Ataca, M. Topsakal, E. Akturk, and S. Ciraci, J. Phys. Chem. C **115**, 16354 (2011).

[127] C. Rice, R. Young, R. Zan, U. Bangert, D. Wolverson, T. Georgiou, R. Jalil, and K. Novoselov, Phys. Rev. B **87**, 081307 (2013).

[128] G. Li, L. Liang, Q. Li, M. Pan, V. Nascimento, X. He, A. B. Karki, V. Meunier, R. Jin, J. Zhang, and E. Plummer, Phys. Rev. Lett. **112**, 077205 (2014).

[129] S. Nandi, M. G. Kim, A. Kreyssig, R. M. Fernandes, D. K. Pratt, A. Thaler, N. Ni, S. L. Bud'ko, P. C. Canfield, J. Schmalian, R. J. McQueeney, and A. I. Goldman, Phys. Rev. Lett. **104**, 057006 (2010).

[130] J. Teng, C. Chen, Y. Xiong, J. Zhang, R. Jin, and E. Plummer, Proc. Natl. Acad. Sci. **110**, 898 (2013).

[131] J. E. Hoffman, Rep. Prog. Phys. **74**, 124513 (2011).

[132] Y. Kamihara, T. Watanabe, M. Hirano, and H. Hosono, J. Am. Chem. Soc. **130**, 3296 (2008).

[133] D. C. Johnston, Adv. Phys. **59**, 803 (2010).

[134] G. Li, X. He, J. Zhang, R. Jin, A. Sefat, M. A. McGuire, D. Mandrus, B. C. Sales, and E. Plummer, Phys. Rev. B **86**, 060512 (2012).

[135] L. Harnagea, S. Singh, G. Friemel, N. Leps, D. Bombor, M. Abdel-Hafiez, A. U. B. Wolter, C. Hess, R. Klingeler, G. Behr, S. Wurmehl, and B. Büchner, Phys. Rev. B **83**, 094523 (2011).

[136] C. Dhital, Z. Yamani, W. Tian, J. Zeretsky, A. Sefat, Z. Wang, R. Birgeneau, and S. D. Wilson, Phys. Rev. Lett. **108**, 087001 (2012).

[137] Y. Kamihara, T. Nomura, M. Hirano, J. E. Kim, K. Kato, M. Takata, Y. Kobayashi, S. Kitao, S. Higashitaniguchi, Y. Yoda, M. Seto, and H. Hosono, New J. Phys. **12**, 033005 (2010).

[138] J. Zhao, Q. Huang, C. de La Cruz, S. Li, J. Lynn, Y. Chen, M. Green, G. Chen, G. Li, Z. Li, J. Luo, N. Wang, and P. Dai, Nat. Mater. **7**, 953 (2008).

[139] P. Cai, X. Zhou, W. Ruan, A. Wang, X. Chen, D.-H. Lee, and Y. Wang, Nat. Commun. **4**, 1596 (2013).

[140] F. Ronning, T. Klimczuk, E. D. Bauer, H. Volz, and J. D. Thompson, J. Phys. Condens. Matter **20**, 322201 (2008).

[141] S. Pan, E. Hudson, and J. Davis, Rev. Sci. Instrum. **70**, 1459 (1999).

[142] A. Goldman, D. Argyriou, B. Ouladdiaf, T. Chatterji, A. Kreyssig, S. Nandi, N. Ni, S. Budko, P. Canfield, and R. McQueeney, Phys. Rev. B **78**, 100506 (2008).

[143] T.-M. Chuang, M. Allan, J. Lee, Y. Xie, N. Ni, S. Budko, G. Boebinger, P. Canfield, and J. Davis, Science **327**, 181 (2010).

[144] E. van Heumen, J. Vuorinen, K. Koepernik, F. Massee, Y. Huang, M. Shi, J. Klei, J. Goedkoop, M. Lindroos, J. van den Brink, and M. S. Golden, Phys. Rev. Lett. **106**, 027002 (2011).

[145] J. Pendry, J. Phys. C: Solid State Phys. **13**, 937 (1980).

[146] M. Gao, F. Ma, Z.-Y. Lu, and T. Xiang, Phys. Rev. B **81**, 193409 (2010).

[147] G. Henkelman, A. Arnaldsson, and H. Jónsson, Comput. Mat. Sci. **36**, 354 (2006).

[148] R. Matzdorf, Z. Fang, J. Zhang, T. Kimura, Y. Tokura, K. Terakura, and E. Plummer, Science **289**, 746 (2000).

[149] K. Prokeš, S. Mataš, L. Harnagea, S. Singh, S. Wurmehl, D. Argyriou, and B. Büchner, Phys. Rev. B **83**, 104414 (2011).

[150] H. Yao-Bo, R. Pierre, W. Ji-Hui, W. Xiao-Ping, S. Xun, X. Nan, W. Zheng, L. Ang, Y. Jia-Xin, and Q. Tian, Chin. Phys. Lett. **30**, 017402 (2013).

[151] J. Kim, V. Chua, G. A. Fiete, H. Nam, A. H. MacDonald, and C.-K. Shih, Nature Phys. **8**, 464 (2012).

APPENDIX A
Publications Related to the Thesis

- E. C. Girão, **L. Liang**, E. Cruz-Silva, A. Filho, and V. Meunier, "Emergence of atypical properties in assembled graphene nanoribbons," Phys. Rev. Lett. **107**, 135501 (2011).

- E. C. Girão, E. Cruz-Silva, **L. Liang**, A. Souza Filho, and V. Meunier, "Structural and electronic properties of graphitic nanowiggles," Phys. Rev. B **85**, 235431 (2012).

- **L. Liang**, E. Cruz-Silva, E. C. Girão, and V. Meunier, "Enhanced thermoelectric figure of merit in assembled graphene nanoribbons," Phys. Rev. B **86**, 115438 (2012).

- **L. Liang** and V. Meunier, "Electronic structure of assembled graphene nanoribbons: Substrate and many-body effects," Phys. Rev. B **86**, 195404 (2012).

- **L. Liang**, E. C. Girão, and V. Meunier, "Quasiparticle band gaps of graphene nanowiggles and their magnetism on Au (111)," Phys. Rev. B **88**, 035420 (2013).

- **L. Liang** and V. Meunier, "Electronic and thermoelectric properties of assembled graphene nanoribbons with elastic strain and structural dislocation," Appl. Phys. Lett. **102**, 143101 (2013).

- E. C. Girão, **L. Liang**, J. Owens, E. Cruz-Silva, B. G. Sumpter, and V. Meunier, *Graphene Chemistry: Theoretical Perspectives* (John Wiley & Sons, Ltd, 2013) Chap. 14, pp. 319-346.

- G. Li, **L. Liang**, Q. Li, M. Pan, V. Nascimento, X. He, A. Karki, V. Meunier, R. Jin, J. Zhang, and E. Plummer, "Role of antiferromagnetic ordering in the (1×2) surface reconstruction of $Ca(Fe_{1-x}Co_x)_2As_2$," Phys. Rev. Lett. **112**, 077205 (2014).

- J. Cai, C. A. Pignedoli, L. Talirz, D. Passerone, P. Ruffieux, J. Liu, H. Sode, **L. Liang**, V. Meunier, R. Berger, X. Feng, K. Mullen, and R. Fasel, "Graphene nanoribbon heterojunctions with p-n-characteristics," Submitted.

- **L. Liang** and V. Meunier, "First-principles Raman spectra of MoS_2, WS_2 and their heterostructures," Nanoscale **6**, 5394 (2014).

INDEX

AA-GNW, 18
anti-ferromagnetic (AFM), 18, 87, 92
aromatic molecules, 7
AZ-GNW, 20

$BaFe_2As_2$, 102
band gap reductions, 46
band structures, 18, 41, 64, 72
bottom-up fabrication, 7
buckling, 40, 47
bulking, 91

$CaFe_2As_2$, 89
charge transfer, 42
computation of ZT, 29

density functional theory (DFT), 13, 30, 39, 50, 70, 89
DFT band gaps, 18, 72
DFT-D2 of Grimme, 39
DFTB+, 30
dielectric constants, 72
dielectric screening, 74, 82
dynamic matrix, 71
dynamical screening, 22

electron mobility, 64
electron transmission function, 28
electronic resonant tunneling, 33
electronic transport, 53
exchange-correlation functional, 16
excitonic solar cells, 57

Fe-based superconductors, 87
ferromagnetic (FM), 18
figure of merit ZT, 27
finite difference, 72
frequency difference, 74

generalized gradient approximation (GGA), 15
GNRs, 5, 40
GNW heterojunctions, 9, 49
GNWs, 9, 11
graphene, 4

image charge model, 44
intensity ratio, 66, 76, 78
interlayer coupling, 74
inward relaxation, 91

Kohn-Sham, 13, 22

laser polarization, 76
local density approximation (LDA), 15, 39
low energy electron diffraction, 89

magnetic robustness on substrate, 47
magnetic states, 18
many-body GW, 23, 44
MoS_2, 62, 73
MoS_2/WS_2 heterostructures, 68, 80

nitrogen doping, 9, 50

non-equilibrium Green's function formalism, 50, 51

orthorhombic, 87

paramagnetic (PM), 18, 87, 92
Perdew-Burke-Ernzerhof (PBE), 16, 50
phonon dispersions, 30
phonon frequencies, 72
PHONON software, 71
phonon thermal conductance, 28
phonon transmission function, 28
photoluminescence, 64
photovoltaic, 63
power conversion efficiency, 57
projection bands, 41

QP band gaps, 24
quasiparticle, 23, 24, 44

Raman intensities, 66, 76
Raman mode A_{1g}, 66
Raman mode E^1_{2g}, 66
Raman spectra, 73, 75, 80
Raman spectroscopy, 66
Raman susceptibility, 71
Raman tensor, 78
Raman theory, 71
roadmap to optimal ZT, 33

scanning tunneling microscopy (STM), 39, 89
scanning tunneling spectroscopy (STS), 89
SIESTA, 50
slab geometry, 39
spin polarization, 6
structural dislocation, 35
substrate, 39
substrate polarization, 43
superconducting gap, 94
superconductivity, 87
surface reconstruction, 91
symmetry space group, 69

tetragonal, 87
theoretical solar cells model, 57
thermal, 28
thermoelectric, 27
thickness dependence, 66
tight-binding+Hubbard model, 16
transition metal dichalcogenides, 62
type-II staggered band alignment, 56

van der Waals (vdW), 39, 62
VASP, 16

work function, 42, 102
WS_2, 62, 75

ZA-GNW, 21
ZZ-GNW, 22